T2R2 東京科学大学 リサーチリポジトリ
Science Tokyo Research Repository

論文 / 著書情報
Article / Book Information

題目(和文)	
Title(English)	Lattice Boltzmann Method for Two-phase Flows with High Density Ratio and Reynolds Number
著者(和文)	SITOMPULYOS P
Author(English)	Yos Sitompul
出典(和文)	学位:博士（工学）, 学位授与機関:東京工業大学, 報告番号:甲第11912号, 授与年月日:2021年3月26日, 学位の種別:課程博士, 審査員:青木 尊之,平井 秀一郎,末包 哲也,肖 鋒,長﨑 孝夫
Citation(English)	Degree:Doctor (Engineering), Conferring organization: Tokyo Institute of Technology, Report number:甲第11912号, Conferred date:2021/3/26, Degree Type:Course doctor, Examiner:,,,,
学位種別(和文)	博士論文
Type(English)	Doctoral Thesis

Powered by T2R2 (Science Tokyo Research Repository)

Lattice Boltzmann Method for Two-phase Flows with High Density Ratio and Reynolds Number

by

Yos Panagaman Sitompul

Submitted to the Department of Mechanical Engineering
in partial fulfillment of the requirements for the degree of

Doctor of Engineering

at the

TOKYO INSTITUTE OF TECHNOLOGY

March 2021

© Tokyo Institute of Technology 2021. All rights reserved.

Author .....
Department of Mechanical Engineering
December 17, 2020

Takayuki AOKI
Professor
Thesis Supervisor

Lattice Boltzmann Method for Two-phase Flows with High Density Ratio and Reynolds Number

by

Yos Panagaman Sitompul

Submitted to the Department of Mechanical Engineering
on December 17, 2020, in partial fulfillment of the
requirements for the degree of
Doctor of Engineering

Abstract

The Lattice Boltzmann Method (LBM) has become a popular alternative for fluid flow simulations. However, the conventional LBM is unstable when simulating two-phase flows with a high-density ratio and Reynolds number. Two types of such problems studied in this thesis are violent two-phase flows and turbulent bubbly flows. A novel cumulant LBM is developed to simulate those problems stably. The proposed method employs a combination of a velocity-based formulation of the two-phase LBM with a cumulant collision model for hydrodynamics and a conservative phase-field lattice Boltzmann method for the interface capturing. The proposed method has been validated for both violent two-phase flows and turbulent bubbly flows. Additionally, we also studied foam formation simulations with thin liquid films. Our proposed method can simulate all the above complex problems stably, which opens possibilities for future applications.

Thesis Supervisor: Takayuki AOKI
Title: Professor

Contents

1 Introduction **19**

1.1 Background 19

1.2 Scope 20

1.3 Literature Review 22

1.4 Objective 24

1.5 Originality 25

1.6 Significance 26

1.7 Outline 27

2 Basic Theory **29**

2.1 Incompressible Navier-Stokes Equations 29

2.2 Lattice Boltzmann Method 30

2.2.1 Single Relaxation Time Model 30

2.2.2 Multi Relaxation Time Model 34

2.2.3 Cumulant Model 35

2.3 Two-phase Flow Formulations 36

2.4 Interface Capturing Methods 38

2.4.1 Volume of Fluid Method 38

2.4.2 Level Set Method 39

2.4.3 Phase-field Method 39

3 Cumulant LBM for Violent Two-phase Flows **41**

3.1 Introduction 41

3.2 Governing equations . . . 43
3.3 Numerical methods . . . 44
3.3.1 Filtered cumulant LBM . . . 45
3.3.2 Conservative phase-field lattice Boltzmann method . . . 54
3.3.3 Boundary conditions . . . 55
3.3.4 Algorithm of computation . . . 55
3.4 Results and discussions . . . 56
3.4.1 2D Rayleigh-Taylor instability . . . 57
3.4.2 2D droplet falling . . . 60
3.4.3 2D rising bubble . . . 62
3.4.4 3D oblique coalescence of two bubbles . . . 65
3.4.5 3D droplet splashing on a thin film . . . 68
3.4.6 3D dam-breaking on a dry floor . . . 72
3.4.7 3D dam-breaking on a wet floor . . . 76
3.4.8 3D liquid jet breakup . . . 79
3.5 Conclusions . . . 84

4 Cumulant LBM for Turbulent Bubbly Pipe Flow Simulations 85
4.1 Introduction . . . 85
4.2 Governing equations . . . 87
4.3 Numerical methods . . . 89
4.3.1 Cumulant LBM with Multi-phase Field Model . . . 89
4.3.2 Boundary conditions . . . 93
4.3.3 Algorithm of computation . . . 93
4.4 Flow Characteristics . . . 94
4.4.1 Computational domain . . . 94
4.4.2 Flow characteristics . . . 96
4.4.3 Test cases . . . 97
4.4.4 Post-processing . . . 99
4.5 Results and Discussions . . . 100

4.5.1 3D bubble rising . . . 100
4.5.2 Turbulent single-phase flows at low Reynolds number . . . 102
4.5.3 Turbulent single-phase flows at high Reynolds number . . . 105
4.5.4 Turbulent Bubbly Channel Flow . . . 106
4.5.5 Turbulent Bubbly Pipe Flow . . . 113
4.6 Conclusions . . . 117

5 Cumulant LBM for Foam Simulations 119
5.1 Introduction . . . 119
5.2 Numerical Methods . . . 120
5.3 Results and Discussions . . . 122
5.4 Conclusions . . . 124

6 Conclusions 127
6.1 Summary . . . 127
6.1.1 Violent flow simulations . . . 129
6.1.2 Turbulent bubbly pipe flow simulations . . . 130
6.1.3 Foam formation simulations . . . 131
6.2 Recommendations . . . 132

Appendices 133

A Cumulant-collision Model 135

List of Figures

1-1 Application of CFD to study the airflow around a car. 19

1-2 Flow patterns in gas-liquid two-phase flow. Adapted from Chen et al. (2006). 21

2-1 D3Q27 lattice model. 33

3-1 Schematic of initial condition of the 2D Rayleigh-Taylor instability problem. 58

3-2 Evolution of the interface shape in 2D Rayleigh – Taylor instability problem with $\Delta x = 1/512$. Herrmann (black), unfiltered cumulant LBM (red), filtered cumulant LBM (blue). Adapted from (Herrmann, 2008). 59

3-3 Interface shapes at final time for various mesh sizes in 2D Rayleigh – Taylor instability problem. Unfiltered cumulant LBM (left) filtered cumulant LBM (right). Herrmann's result is shown as background (black). Adapted from (Herrmann, 2008). 60

3-4 Evolution of droplet shapes in 2D falling droplet problem at $t^* = 2$, $t^* = 3$, $t^* = 4$, $t^* = 5$, $t^* = 6$, $t^* = 7$, and $t^* = 9$. Reference (blue) and filtered cumulant LBM (red). Adapted from (Fakhari et al., 2017b) . 61

3-5 Schematic of initial condition of the 2D rising bubble problem. 62

3-6 Bubble shapes at final time (left) and rise velocity (right) for Case 1 of the 2D rising bubble problem. Filtered cumulant LBM with $Ma_{max} = 0.007$ (red), filtered cumulant LBM with $Ma_{max} = 0.014$ (blue). References: TP2D (Hysing et al., 2009) (solid black) and Abels (Aland and Voigt, 2012) (dashed black). 64
3-7 Bubble shapes at final time (left) and rise velocity (right) for Case 2 of the 2D rising bubble problem. Filtered cumulant LBM with $Ma_{max} = 0.012$ (red), filtered cumulant LBM with $Ma_{max} = 0.024$ (blue). References: TP2D (Hysing et al., 2009) (solid black) and Abels (Aland and Voigt, 2012) (dashed black). 64
3-8 Schematic of initial condition of the 3D oblique coalescence of two bubbles. 65
3-9 Evolution of bubble shapes in 3D oblique coalescence of two bubbles problem. van Sint Annaland et al. (2005) (left), unfiltered cumulant LBM (middle), and filtered cumulant LBM (right). 67
3-10 Evolution of rising velocities in 3D oblique coalescence of two bubbles problem. Unfiltered cumulant LBM (blue) and filtered cumulant LBM (red). Included are the experimental photos taken from Brereton and Korotney (Brereton and Korotney, 1991). 68
3-11 Schematic of initial condition of the 3D droplet splashing on a thin film. 69
3-12 Interface evolution in 3D droplet splashing on a thin film at a resolution $\Delta x = D/200$. Unfiltered cumulant LBM (left) and filtered cumulant LBM (right). 70
3-13 Evolution of the crown radius in 3D droplet splashing on a thin film problem. Reference (Rieber and Frohn, 1999) (black line), unfiltered cumulant LBM (blue circle), and filtered cumulant LBM (red triangle). 71
3-14 Determination of crown radius $r = (r_i + r_o)/2$ in 3D droplet splashing on a thin film problem. 72
3-15 Schematic of initial condition of the 3D dam-breaking on a dry floor problem. 73

3-16 Evolution of water profile for 3D dam-breaking problem on a dry floor. Experimental by Hu and Sueyoshi (Hu and Sueyoshi, 2010) (left), filtered cumulant LBM – free-slip (middle), filtered cumulant LBM – no-slip (right). 75

3-17 Evolution of dimensionless surge front position for 3D dam-breaking problem on a dry floor. Slip (red) and no-slip (blue) at resolution of $400 \times 300 \times 100$. References: experiment by Hu and Sueyoshi (Hu and Sueyoshi, 2010) (black circle), experiment by Martin and Moyce (Martin et al., 1952) (black square), and simulation by Janssen and Krafczyk (2010) (black triangle). 75

3-18 Schematic of initial condition of the 3D dam-breaking problem on a wet floor. 77

3-19 Evolution of water profiles in 3D dam-breaking on a wet floor. Reference ($576 \times 96 \times 288$) (top), filtered cumulant LBM ($576 \times 96 \times 288$) (middle), and filtered cumulant LBM ($1152 \times 192 \times 576$) (bottom). . 78

3-20 Evolution of water profiles in 3D dam-breaking on a wet floor at $t = 1.0$ s using filtered cumulant LBM. Resolution: $576 \times 96 \times 288$ (left) and $1152 \times 192 \times 576$ (right). 78

3-21 Schematic of initial condition of the liquid jet atomization problem. . 79

3-22 The overall flow structure at $T^* = 7.19$ in liquid jet breakup for Case 1. Reference ($\Delta x = D/286$) (a), unfiltered cumulant LBM ($\Delta x = D/100$) (b), filtered cumulant LBM ($\Delta x = D/50, Pe_{cutoff} = 2$) (c), filtered cumulant LBM ($\Delta x = D/100, Pe_{cutoff} = 2$) (d), filtered cumulant LBM ($\Delta x = D/100, Pe_{cutoff} = 20$) (e), and filtered cumulant LBM ($\Delta x = D/100, Pe_{cutoff} = 50$) (f). 81

3-23 Interface shapes and axial velocities (upper half) at $y = 2.5D, T^* = 7.19$ in liquid jet breakup for Case 1. Reference ($\Delta x = D/286$) (a), unfiltered cumulant LBM ($\Delta x = D/100$) (b), filtered cumulant LBM ($\Delta x = D/50, Pe_{cutoff} = 2$) (c), filtered cumulant LBM ($\Delta x = D/100, Pe_{cutoff} = 2$) (d), filtered cumulant LBM ($\Delta x = D/100, Pe_{cutoff} = 20$) (e), and filtered cumulant LBM ($\Delta x = D/100, Pe_{cutoff} = 50$) (f). 82

3-24 Interface shape of liquid jet breakup (Case 1, high resolution) at $T^* = 7.19$. 82

3-25 Interface shapes at $T^* = 7.19$ in liquid jet atomization obatined using filtered cumulant LBM with $\Delta x = D/100$ and $Pe_{cutoff} = 20$. Case 1 (a) and Case 2 (b). 83

4-1 The schematic of the original active parameter tracking (APT) method. 91

4-2 The schematic of the improved active parameter tracking (APT) method. 92

4-3 Schematic of the computational domain used in the present turbulent channel and pipe flow simulations. 95

4-4 Comparison of bubble shapes in 3D bubble-rising problem. For each case, the bubble shape is split in half: one half obtained by van Sint Annaland et al. (2005) (left) and the other half obtained by the proposed method (right). 101

4-5 Turbulent single-phase flow structures at low Reynolds number. Red and blue colours represent positive and negative values, respectively. . 103

4-6 Comparison of the turbulent statistics distribution of the turbulent single-phase flow at low Reynolds number obtained from the present simulation and the references, normalized by the friction velocity. . . 104

4-7 Turbulent single-phase flow structures at high Reynolds number. Red and blue colours represent positive and negative values, respectively. . 106

4-8 Comparison of the turbulent statistics of the turbulent single-phase flow at high Reynolds number obtained from the present simulation and the references, normalized by the friction velocity. 107

4-9 Instantenous bubble distributions and Q-criterion values in the turbulent bubbly channel flows. 109
4-10 Comparison of the first-order turbulent statistics in the turbulent bubbly channel flow obtained from the present simulation and the references: $\alpha = 1.5\%$ (left) and $\alpha = 19.4\%$ (right). 110
4-11 Comparison of the second-order turbulent statistics in the turbulent bubbly channel flow obtained from the present simulation and the references: $\alpha = 1.5\%$ (left) and $\alpha = 19.4\%$ (right). 111
4-12 Instantenuos bubble distribution (left) and Q-criterion value (right) in the turbulent bubbly pipe flow obtained from the present simulation. 114
4-13 The comparison of the velocity field inside and around a single bubble obtained from the present simulation. Turbulent bubbly channel flow with $\alpha = 1.5\%$ (A), $\alpha = 19.4\%$ (B) and turbulent bubbly pipe flow with $\alpha = 9.5\%$ (C). 114
4-14 Comparison of the first-order turbulent statistics in the turbulent bubbly pipe flow. The average void fraction distribution (left) and the average streamwise velocity, normalized by the friction velocity (right). 115
4-15 Comparison of the second-order turbulent statistics in the turbulent bubbly pipe flow, normalized by the friction velocity. 116

5-1 The topology of the bubble cluster by MPF method. 121
5-2 Bubble shapes at final time (left) and rise velocity (right) for Case 2 of the 2D rising bubble problem. Cumulant LBM with 10 pressure iterations (red), cumulant LBM without pressure iteration (blue). References: TP2D (Hysing et al., 2009) (solid black) and Abels (Aland and Voigt, 2012) (dashed black). 123
5-3 Snapshots of a 2D foam development. 123
5-4 Snapshots of a 3D foam development. 124

List of Tables

2.1 Discrete velocities and weights of D3Q27 lattice model. 33

3.1 Physical parameters (non-dimensional unit) and dimensionless numbers in 2D rising bubble problem. 63

3.2 Physical parameters in 3D liquid jet breakup problem. 80

4.1 Comparison of the details of the turbulent bubbly flow simulations between the present study and the references. 98

4.2 Comparison of the terminal Reynolds numbers in 3D bubble-rising problem. 101

Acronyms

AC Allen–Cahn.

AMR Adaptive Mesh Refinement.

BGK Bhatnagar-Gross-Krook.

CBE Continuum Boltzmann Equation.

CFD Computational Fluid Dynamics.

CH Cahn-Hiliard.

CPF Conservative Phase Field.

CPFLBM Conservative Phase Field Lattice Boltzmann Method.

DBE Discrete Boltzmann Equation.

DNS Direct Numerical Simulation.

FDM Finite Difference Methods.

FT Front-Tracking.

HJ-WENO Hamilton-Jacobi Weighted Essentially Non-Oscillatory.

INSE Incompressible Navier-Stokes Equations.

LBM Lattice Boltzmann Method.

LGA Lattice Gas Automata.

LKS Lattice Kinetic Scheme.

LS Level-Set.

MAC Marker and Cell.

NSE Navier-Stokes Equations.

PDF Particle Distribution Function.

PF Phase-Field.

PIC Particle-In-Cell.

PLIC Piecewise Linear Interface Calculation.

SMAC Simplified Marker and Cell.

SPH Smoothed Particle Hydrodynamics.

SRT Single-Relaxation Time.

THINC Tangent of Hyperbola for Interface Capturing.

TVD Total Variation Diminishing.

VOF Volume of Fluid.

Chapter 1

Introduction

1.1 Background

Computational Fluid Dynamics (CFD) is a useful tool for studying problems involving fluid flow, especially when analytical or experimental methods are not feasible. By using computers, various fluid flow problems can be simulated, such as the aerodynamics of a vehicle (see Fig. 1-1 as an example), cooling process, combustion analysis, chemical process engineering, and weather prediction. From these simulations, one can gain insights into the problems, create theories about certain phenomena, develop a more efficient process, or improve a system's safety.

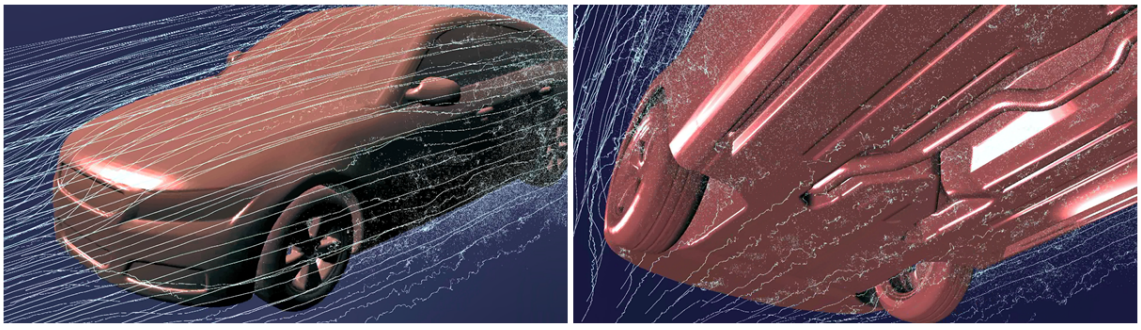

Figure 1-1: Application of CFD to study the airflow around a car.

The development of CFD is closely related to the development of computers. In its early development, calculations had to be performed manually, and simplified equations such as the linearized potential equations were solved instead of Navier-Stokes

Equations (NSE) (Richardson, 2007; Kawaguti, 1953). With the increase of computing power, the computations based on NSE were studied, both for the compressible flows (Harlow et al., 1955; Lax and Wendroff, 1960) and incompressible flows (Harlow and Welch, 1965; Chorin, 1967a; Patankar, 1980). Since 1990s, CFD has become an indispensable part of the aerodynamic and hydrodynamic design process for planes, trains, automobiles, rockets, ships, and submarines.

With the continuous development of supercomputers, CFD continues to develop to perform more accurate simulations or simulate more complex problems. One complex problem that has gained more attention recently is a multi-phase flow problem. An interactive flow that involves several phases, namely solid, liquid, and gas, is called a multi-phase flow. This type of flow can occur naturally, such as cloud formation, river flow, groundwater flow, blood flow, or artificially as in various industries, such as fluidized bed, crude oil flow in pipelines, combustion reactors, and fiber suspension flow. Using a supercomputer, all of the above complex problems become more and more feasible to simulate realistically.

1.2 Scope

In this dissertation, we focus our study on a subset of multi-phase flows called liquid-gas two-phase flows that are immiscible and incompressible. Historically, this type of flow was commonly studied in large-scale power systems. For example, a nuclear reactor uses water to remove heat from its reactor core, and steam can occur in this cooling process (see Fig. 1-2 as an example). The phenomena that occur in this two-phase flow are very different from the single-phase flow. In-depth knowledge of this two-phase flow phenomena is essential for the better design, operation, maintenance, and safety of the nuclear reactor. Other applications involving this two-phase flow include marine engineering, inkjet, spray, combustion engines, and fire fighting.

Although the CFD field is mature, the liquid-gas two-phase flow simulation is still lagging and need to be further developed. This lag comes from the difficulty in simulating the two phases that move, deform, and interact dynamically. The

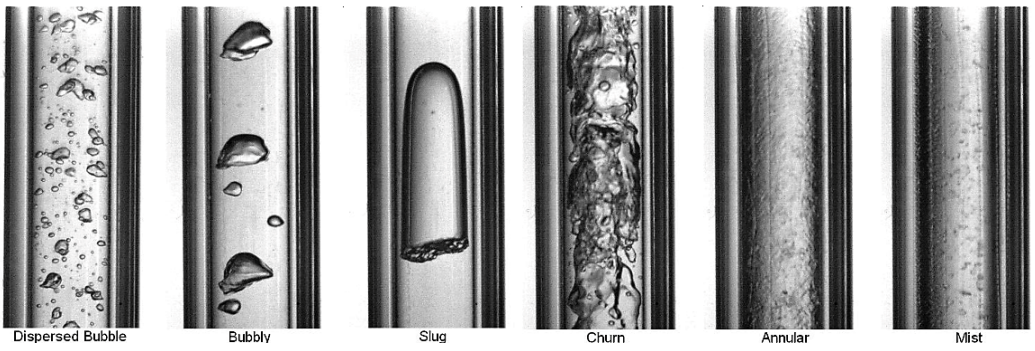

Figure 1-2: Flow patterns in gas-liquid two-phase flow. Adapted from Chen et al. (2006).

interface separating the liquid from the gas is very thin, with a large density and viscosity contrast. The interface also exerts local surface tension forces on fluids, and its topology varies greatly. The simulation becomes even more difficult when other phenomena such as turbulence, material transport, and heat transport are considered. One must also ensure that the simulation conserves mass, momentum, and energy. Therefore, it requires advanced calculation methods to simulate these various conditions accurately. Moreover, the methods should be efficient for parallel computation.

Many methods have been developed to simulate the immiscible, incompressible, two-phase flows. However, most of these methods focus only on small-scale simulations with simple flow conditions. In this research, we are interested in developing a method for large-scale simulations with complex flow conditions, i.e., industrial applications. In conventional method, the Incompressible Navier-Stokes Equations (INSE) solver is employed to simulate the two-phase hydrodynamics, while an interface tracking/capturing method such as Front-Tracking (FT), Volume of Fluid (VOF), and Level-Set (LS) is employed to simulate the liquid-gas interface (Tryggvason et al., 2001; Hirt and Nichols, 1981; Osher and Sethian, 1988). Its computational performance relied heavily on the computational performance of the pressure Poisson solver it uses, which is greatly reduced in large-scale simulations with complex flow conditions (ONODERA and AOKI, 2014). Moreover, the conventional interface tracking/capturing methods have issues handling topological change, simulating

surface-tension accurately, and conserving mass. Although there are more sophisticated algorithms to overcome these limitations, their parallel efficiency are lower than the original methods.

In this dissertation, we applied an alternative method called Lattice Boltzmann Method (LBM) (Qian et al., 1992). Instead of solving INSE, it solves a simplified Boltzmann equation using lattice discretization and low Mach number approximation. The resulting kinetic equation is simple and can simulate incompressible viscous flows without solving the pressure Poisson equation. Moreover, it can handle complex boundaries and efficient for parallel computation. To simulate the liquid-gas interface, we employed a conservative phase-field model. Its algorithm is simple, and it can handle topological change, simulate surface-tension accurately, and conserve mass. For the interface capturing, an alternative method called a conservative phase-field model (Chiu and Lin, 2011). The model can handle topological change, simulate the interfaces accurately, conserve mass, and efficient for parallel computation. The combined algorithm has good parallel efficiency, and therefore is promising for large-scale two-phase flow simulations.

1.3 Literature Review

LBM is an alternative to classical INSE solvers, which solves the Boltzmann equation governing the kinetic of microscopic variables namely the probability distribution functions using certain assumptions and discretizations. The macroscopic flow variables, such as pressure and velocity, are obtained as low-order moments of these distribution functions. It is now known that the LBM converges towards INSE solution, with second-order accuracy in space and time (He and Luo, 1997). The LBM is efficient to be implemented in parallel computers than those of traditional CFD solvers.

LBM was initially used for single-phase flow simulations and has been successful, especially in simulating porous media flow (Guo and Zhao, 2002). LBM's use for two-phase flow is not straightforward due to LBM's characteristics that allow only

negligible density changes. Many studies have been done to solve this issue, which can be classified into four representative models:

1. Color-Gradient model: The model was proposed by Gunstensen and Rothman (1993), where distinct fluids are represented by color functions that evolve via their own discretized Boltzmann equation and interact with each other via local color gradients. The recoloring step was improved by Latva-Kokko and Rothman (2005) to reduce the spurious current across the interface. This model has disadvantages in that its recoloring step is time-consuming, and it is limited to low-density ratio two-phase flows.

2. Pseudo-potential model: The model was proposed by Shan and Chen (1993), where the distribution functions are modified by a pseudo-potential forcing term that models interfacial interactions between different phases. Although it cannot satisfy the local momentum conservation law, the SC model attracted much popularity due to its accuracy and ease of implementation. This model, however, is also limited to low-density ratio two-phase flows.

3. Free energy model: Swift et al. (1996) used free-energy functional to model the interfacial interactions between different phases. Two sets of particle distribution functions are employed to solve the approximate INSE equations and Cahn-Hiliard (CH) equation for interface capturing. Swift's model, however, suffers from the non-Galilean invariance. Inamuro et al. (2004) developed an improved model by solving an order parameter equation and the pressure Poisson equation. This model is capable of a high-density ratio as high as 1000. However, the calculation of the pressure Poisson equation is hefty.

4. Kinetic theory based discrete Boltzmann equation: The pioneer works of this kind of model were conducted by He et al. (1998), who transformed the conventional lattice Boltzmann equation from a mass and momentum formulation to a pressure and momentum formulation. This transformation helps reducing instabilities due to high fluid density gradients at the interface. Like Swift

et al. (1996), the second set of particle distribution functions is used to track the interface. Lee and Lin (2003) showed that this model's pressure evolution equation is an ideal gas pressure evolution. Lee and Lin (2005) developed a high-density ratio two-phase model phase model through a stable intermolecular force. However, its computational efficiency is reduced due to the use of mixed discretization for the intermolecular force. Fakhari et al. (2016) proposed a mass-conserving conserving two-phase model with a dynamic grid refinement technique to improve computational efficiency. A new formulation was also recently developed by Fakhari et al. (2017b) to improve computational efficiency by using a velocity-based formulation of the kinetic theory-based discrete Boltzmann equation.

1.4 Objective

Despite the many successes of the previous two-phase LBM, violent two-phase flows and turbulent bubbly flows with a high-density ratio and high Reynolds number have not been succesfully simulated using two-phase LBMs. In this dissertation, we extend the LBM for two flows from the kinetic theory-based discrete Boltzmann equation. We have developed a novel cumulant LBM with a conservative phase-field model for interface capturing to simulate two-phase flows with a high-density ratio and high Reynolds number. The development of the method is described in detail in Chapter 3.

In this dissertation, three topics are studied:

1. **Violent two-phase flow** problems such as dam-breaking and liquid jet breakup where the density ratio and Reynolds number are high, and there are rapid and complex topological changes,

2. **Turbulent bubbly pipe flow** of a water-air system, a common experimental setting, with high-density ratio and Reynolds number,

3. **Foam formation** with thin films and a large number of bubbles.

These topics have not been studied much because of their difficulty. By simulating these three topics, we expect that the proposed method can be used for a wide range of future applications, especially for industrial applications.

1.5 Originality

1. **Violent two-phase flow problems**: The violent two-phase flows with high-density ratio ratios such as dam breaking problems are often simulated using a free-surface model, where the gas phase dynamics are neglected (Janssen and Krafczyk, 2010). Only the liquid phase is simulated, and the free-surface boundary is applied at the liquid-gas interface. Although this model is simple, it is unrealistic in simulating droplets and bubbles generated by the violent flows. A two-phase flow model should be used for more realistic simulation, where the gas phase is simulated; however, there was no previously successful simulation using two-phase LBM, especially for high Reynolds number. This dissertation develops a novel cumulant LBM, which employs a velocity-based LBM formulation with a cumulant type collision model and a velocity-field filter to simulate the two-phase hydrodynamics (Sitompul and Aoki, 2019). Using the proposed method, the violent two-phase flows with a high-density ratio, and Reynolds number have been successfully simulated for the first time using LBM.

2. **Turbulent bubbly pipe flow**: The turbulent bubbly flow has been studied using DNS; however, the past studies are limited to channel flow with low-density ratio ($\gamma \approx 10$) and low Reynolds number ($\mathrm{Re}_\tau \approx 180$) (Lu and Tryggvason, 2006; Bois, 2017; Cifani et al., 2018). Although these simulations can capture the fundamentals of bubble interactions with turbulence flow, they are inaccurate in simulating experimental condition where the density ratio and Reynolds number are high. Therefore in this dissertation, we simulated a turbulent bubbly pipe flow with a high-density ratio ($\gamma \approx 832$) and high Reynolds number ($\mathrm{Re}_\tau \approx 550$) and validated the simulation with the experimental value for the

first time (Sitompul et al., 2021). Moreover, we can expect good parallel efficiency by using cumulant LBM and conservative phase-field models.

3. **Foam simulation**: To simulate stable thin liquid film in foam formation is a difficult task. Past research tried to simulate the thin film using Adaptive Mesh Refinement (AMR), considering the Marangoni effect, and calculating viscoelastic fluid. However, the computation cost is high, especially if one wants to resolve real liquid film thickness and simulate many bubbles. As an alternative method, we employ our cumulant LBM with a multi-phase filed model to simulate foam formation with a high-density ratio and stable thin liquid films.

1.6 Significance

This research produces a method that can be used to simulate a more complex two-phase flow. With better simulation capabilities, in the future, this method can be used to simulate two-phase flow problems in industries more realistically. Some application examples of problems that can be studied in the future:

1. **Violent two-phase flow problems**: A large simulation can be used in the disaster prevention study by considering the interaction between free-surfaces and much debris to determine debris trapping and impact on building structures. Moreover, violent flow study is an essential mechanism in spreading droplets, currently being attention in present coronavirus pandemic on how the disease is transmitted via droplets spreading.

2. **Turbulent bubbly pipe flow**: for the characterization of turbulent flow in the presence of bubbles, especially for conditions of very high Reynolds number (industrial conditions). Can be used to improve the design of cooling processes and damage prevention.

3. **Foam formation**: to understand the stability of liquid films and foams. Furthermore, the new area of heat transfer and material transportation through liquid film can be explored.

1.7 Outline

This dissertation contains six chapters:

1. **Chapter 1: Introduction**: We give the background and scope of our study, followed with a literature review. We then formulate our objective, specify our originality, and describe the significance of our study.

2. **Chapter 2: Basic theory**: We describe the prerequisite knowledge for developing the proposed method, which includes the Incompressible Navier-Stokes Equations (INSE), the improved collision models of Lattice Boltzmann Method (LBM) , the two-phase LBM formulations, and the standard interface capturing schemes.

3. **Chapter 3: Cumulant LBM for violent two-phase flows**: We apply our proposed method, namely the cumulant LBM for violent two-phase flow simulations. The method is described in detail and followed by several validation tests.

4. **Chapter 4: Cumulant LBM for turbulent bubbly pipe flow simulations**: We applied our proposed method to simulate a turbulent bubbly pipe flow. We add the multi-phase field model to be able to simulate dispersed bubbles. Several tests have been performed, and the results are validated with reference computational and experimental results.

5. **Chapter 5: Cumulant LBM for foam simulations**: We applied our proposed method to simulate thin liquid film in foam formation. We improve the pressure calculation and the efficiency of multi-phase field calculation. The proposed method opens new possibilities for future studies and applications of flow involving thin liquid film.

6. **Chapter 6: Conclusions and Recommendations**: We summarize our study, give some quantitative results, and describe some possible future studies.

Chapter 2

Basic Theory

This chapter describes the prerequisite knowledge for the development of the proposed method. Section 2.1 describes the Incompressible Navier-Stokes Equations (INSE) that govern the fluid motion. Section 2.2 describes the Lattice Boltzmann Method (LBM) with a focus on improving the collision model. Section 2.3 describes the two-phase LBM formulation: the momentum-based and velocity-based formulations. Section 2.4 describes three standard interface capturing methods: namely, the Volume of Fluid (VOF), Level-Set (LS), and Phase-Field (PF) methods.

2.1 Incompressible Navier-Stokes Equations

The following INSE describe the dynamics of an incompressible viscous fluid:

$$\nabla \cdot \mathbf{u} = 0, \tag{2.1}$$

$$\frac{\partial \mathbf{u}}{\partial t} + \mathbf{u} \cdot \nabla \mathbf{u} = -\frac{1}{\rho}\nabla p + \frac{1}{\rho}\nabla \cdot \left[\mu \left(\nabla \mathbf{u} + \nabla^T \mathbf{u}\right)\right] + \frac{1}{\rho}\mathbf{F} \tag{2.2}$$

where ρ is the fluid density, $\mathbf{u}$ is the fluid velocity, p is the pressure acting on the fluid, μ is the dynamic viscosity of the fluid, $\mathbf{F}$ is external forces acting on the fluid, and t is time. Eq. (2.2) describes the motion of fluid due to the advection of momentum (the second term at the left-hand side), the pressure gradient (the first term at the right-hand side), the diffusion of momentum (the second term at the right-hand side), and

external forces (the third term at the right-hand side), under the incompressibility condition of Eq. (2.1). The solution of these coupled equations still cannot be obtained analytically up to now, except for a little simplified problem. Therefore numerical methods are continuously being developed to obtain the solution.

2.2 Lattice Boltzmann Method

Lattice Boltzmann Method (LBM) is an alternative numerical method for simulating fluid flows. It can be derived either as an extension of Lattice Gas Automata (LGA) (Frisch et al., 1986), or as an approximation to the Continuum Boltzmann Equation (CBE). Hereafter, the derivation of LBM from the CBE (Chen et al., 1998) is described.

2.2.1 Single Relaxation Time Model

Instead of solving the INSE of Eqs. (2.1) and (2.2) directly, LBM solves the following CBE:

$$\frac{\partial f}{\partial t} + \boldsymbol{\xi} \cdot \nabla f = \Omega, \tag{2.3}$$

where $f \equiv f(\boldsymbol{\xi}, \mathbf{x}, t)$ is the Particle Distribution Function (PDF) that is the probability of finding a particle with velocity $\boldsymbol{\xi}$ at position $\mathbf{x}$ and time t, and Ω is a collision term. With particular approximations and discretizations, the INSE can be obtained from the CBE.

The collision term Ω in Eq. (2.3) can be approximated as a linear operator on the PDF, known as the BGK collision model (Bhatnagar et al., 1954), as follows:

$$\Omega = -\frac{1}{\tau}\left(f - f^{eq}\right), \tag{2.4}$$

where τ is the relaxation time and f^{eq} is the local equilibrium distribution given by

the following Maxwell-Boltzmann equilibrium distribution:

$$f^{eq} = \frac{\rho}{(2\pi RT)^{D/2}} \exp\left[-\frac{(\boldsymbol{\xi} - \mathbf{u})^2}{2RT}\right], \tag{2.5}$$

where ρ is the fluid density, $\mathbf{u}$ is the fluid velocity, D is the spatial dimension, R is the gas constant, and T is the absolute temperature. Eq. (2.3) can then be rewritten as

$$\frac{\partial f}{\partial t} + \boldsymbol{\xi} \cdot \nabla f = -\frac{1}{\tau}\left(f - f^{eq}\right). \tag{2.6}$$

The collision operator conserves mass, momentum, and energy that

$$\rho = \int f d\xi = \int f^{eq} d\xi, \tag{2.7}$$

$$\rho \mathbf{u} = \int \xi f d\xi = \int \xi f^{eq} d\xi, \tag{2.8}$$

$$\rho\varepsilon = \frac{1}{2}\int (\boldsymbol{\xi} - \mathbf{u})^2 f d\xi = \frac{1}{2}\int (\boldsymbol{\xi} - \mathbf{u})^2 f^{eq} d\xi. \tag{2.9}$$

The particle velocity $\boldsymbol{\xi}$ can be discretized into a finite set of velocity $\boldsymbol{\xi}_\alpha$ to obtain the following Discrete Boltzmann Equation (DBE):

$$\frac{\partial f_\alpha}{\partial t} + \boldsymbol{\xi}_\alpha \cdot \nabla f_\alpha = -\frac{1}{\tau}\left(f_\alpha - f_\alpha^{eq}\right), \tag{2.10}$$

where $f \equiv f_\alpha(\mathbf{x}, t)$ is the discrete PDF that is the probability of finding a particle with discrete velocity $\boldsymbol{\xi}_\alpha$ at position $\mathbf{x}$ and time t.

Eq. (2.10) can then be made non-dimensional by introducing the reference length L_r, the reference speed U_r, the reference density ρ_r, and the time between particle collision t_c as follows:

$$\frac{\partial \hat{f}_\alpha}{\partial \hat{t}} + \mathbf{e}_\alpha \cdot \hat{\nabla} \hat{f}_\alpha = -\frac{1}{\hat{\tau}\epsilon}\left(\hat{f}_\alpha - \hat{f}_\alpha^{eq}\right). \tag{2.11}$$

where $\hat{f}_\alpha = f_\alpha/\rho_r$, $\hat{\mathbf{x}} = L_r\mathbf{x}$, $\hat{t} = U_r t/L_r$, $\mathbf{e}_\alpha = \boldsymbol{\xi}_\alpha/U_r$, $\hat{\nabla} = L_r\nabla$, $\hat{\tau} = \tau/t_c$. The parameter $\epsilon = U_r t_c/L_r$ can be interpret as a Knudsen number which is the ratio of mean free path to reference length scale.

Eq. (2.11) can be written in semi-Lagrangian form by integrating along the characteristic line $\mathbf{x} + \mathbf{e}_{\boldsymbol{\alpha}}\delta t$ over $[t, t+\delta t]$ and selecting the lattice spacing to time step ratio equal to lattice velocity ($\mathbf{e}_\alpha = \delta\hat{\mathbf{x}}/\delta\hat{t}$) as follows:

$$\hat{f}_\alpha(\hat{\mathbf{x}} + \mathbf{e}_\alpha\delta\hat{t}, \hat{t} + \delta\hat{t}) - \hat{f}_\alpha(\hat{\mathbf{x}}, \hat{t}) = -\frac{\delta\hat{t}}{\hat{\tau}\epsilon}\left(\hat{f}_\alpha(\hat{\mathbf{x}}, \hat{t}) - \hat{f}_\alpha^{eq}(\hat{\mathbf{x}}, \hat{t})\right), \tag{2.12}$$

Setting $\delta\hat{t} = t_c$, and dropping all hats leads to the following equation:

$$f_\alpha(\mathbf{x} + \mathbf{e}_\alpha\delta t, t + \delta t) - f_\alpha(\mathbf{x}, t) = -\frac{1}{\tau}\left(f_\alpha(\mathbf{x}, t) - f_\alpha^{eq}(\mathbf{x}, t)\right). \tag{2.13}$$

Eq. (2.13) is unique for its simplicity, since it employs local parameters only. Equation Eq. (2.13) can be split up into a local collision and streaming step as follows:

$$f_\alpha^*(\mathbf{x}, t) = f_\alpha(\mathbf{x}, t) - \frac{1}{\tau}\left(f_\alpha(\mathbf{x}, t) - f_\alpha^{eq}(\mathbf{x}, t)\right), \tag{2.14}$$

$$f_\alpha(\mathbf{x} + \mathbf{e}_\alpha\delta t, t + \delta t) = f_\alpha^*(\mathbf{x}, t), \tag{2.15}$$

where f_α^* is the post-collision distribution function. In the collision step, particle distribution functions are driven to their equilibrium locally, as shown in Eq. (2.14), whereas in the streaming step, the post-collision distribution functions are shifted to their corresponding neighbors, as shown in Eq. (2.15). Eq. (2.13) is also know as the Single-Relaxation Time (SRT) – Lattice Boltzmann Method (LBM) because its linear collision operator employs a single relaxation time only.

Through Taylor expansion and neglecting the $O(\mathbf{u}^3)$ terms with the assumption that fluid velocity is small compared with the sound speed (low Mach number assumption), the discrete equilibrium distribution f_α^{eq} can be approximated as (Koelman, 1991):

$$\begin{aligned} f_\alpha^{eq} &= \rho\frac{1}{(2\pi RT)^{D/2}}\exp\left(\frac{\mathbf{e}_\alpha^2}{2RT}\right)\exp\left[1 + \frac{\mathbf{e}_\alpha\cdot\mathbf{u}}{RT} + \frac{(\mathbf{e}_\alpha\cdot\mathbf{u})^2}{2R^2T^2} - \frac{\mathbf{u}^2}{2RT} + O(\mathbf{u}^3)\right] \\ &\approx \rho w_\alpha\left[1 + \frac{\mathbf{e}_\alpha\cdot\mathbf{u}}{c_s^2} + \frac{(\mathbf{e}_\alpha\cdot\mathbf{u})^2}{2c_s^4} - \frac{\mathbf{u}^2}{2c_s^2}\right], \end{aligned} \tag{2.16}$$

where w_α are the weighting factors that depend on the chosen lattice model and $c_s = \sqrt{RT}$ is the isothermal sound speed.

There are several lattice models have been developed and among them, the group DdQq (d-dimensional q-velocity) models proposed by Qian et al. (1992) are the most respective one. In this dissertation, we employs D3Q27 lattice model as shown in Fig. 2-1. Table 2.1 shows the sound speed, discrete velocity, and weights of D2Q9 and D3Q27 models. The discrete velocities $\mathbf{e}_\alpha$ and weights w_α as shown in Table 2.1, where $c = \delta x/\delta t$ is the lattice speed, δx is the lattice spacing, and δt is the lattice time step. The square of the sound speed c_s^2 of this lattice is $c^2/3$.

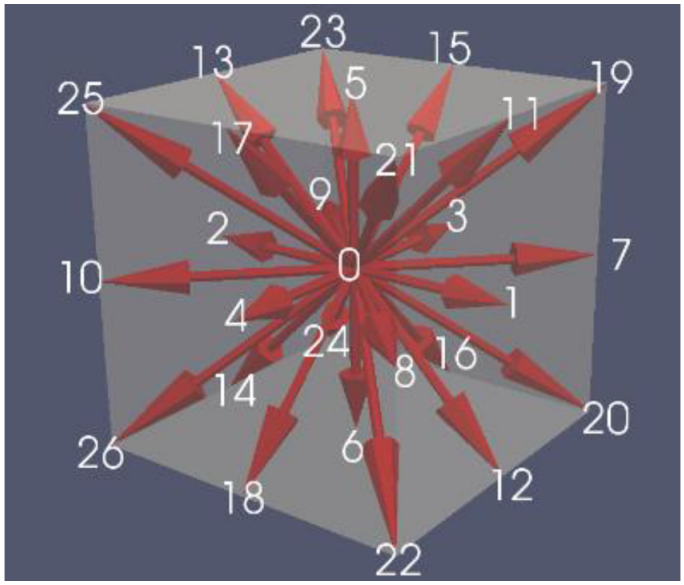

Figure 2-1: D3Q27 lattice model.

Table 2.1: Discrete velocities and weights of D3Q27 lattice model.

α	$\mathbf{e}_\alpha/c$	w_α
0	(0, 0, 0)	8/27
1, ..., 6	(±1, 0, 0), (0, ±1, 0), (0, 0, ±1)	2/27
7, ..., 18	(±1, ±1, 0), (±1, 0, ±1), (0, ±1, ±1)	1/54
19, ..., 26	(±1, ±1, ±1)	1/216

The macroscopic variables can be obtain from the PDF as follows:

$$\rho = \sum_\alpha f_\alpha, \tag{2.17}$$

$$\rho \mathbf{u} = \sum_{\alpha} \mathbf{u}_{\alpha} f_{\alpha}, \tag{2.18}$$

Through the Chapmann-Enskog analysis, it can be proved that LBM satisfy the INSE of Eqs. (2.1) and (2.2) up to errors of $O(\delta x^2)$ and $O(\mathrm{Ma}^2)$, with the pressure p and the kinetic viscosity ν as follows:

$$p = \rho c_s^2, \tag{2.19}$$

$$\tau = \frac{\nu}{c_s^2 \Delta t} + \frac{1}{2} \tag{2.20}$$

LBM is a weakly compressible model with the density fluctuation ($\delta\rho = \rho - \rho_0$) is of the order $O(\mathrm{Ma}^2)$ in the limit of $\mathrm{Ma} \to 0$, where ρ_0 is the supposedly constant density).

2.2.2 Multi Relaxation Time Model

In SRT-LBM, all off-equilibrium particle distribution functions relax simultaneously; however, physically, each should be able to relax at different times. Chapman-Enskog analysis shows that the macroscopic flow quantities obtained from the particle distribution functions, thus in the SRT model, all these quantities relax simultaneously. This model's apparent defects have been known, such as the fixed ratio of the kinematic and bulk viscosities. Although it is simple, the SRT model is numerically unstable for simulating high Reynolds number flows.

To overcome the defects of SRT-LBM method, the generalized lattice Boltzmann method was developed, which is also now known as multiple-relaxation time – lattice Boltzmann method (MRT-LBM) (d'Humieres, 2002; Suga et al., 2015). The kinetic equation of this method is shown in the following equation:

$$f_{\alpha}(\mathbf{x} + \mathbf{e}_{\alpha}\delta t, t + \delta t) - f_{\alpha}(\mathbf{x}, t) = -\sum_{\beta} \Lambda_{\alpha\beta} \left(f_{\beta}(\mathbf{x}, t) - f_{\beta}^{eq}(\mathbf{x}, t) \right) \tag{2.21}$$

In this method, a collision matrix Λ acts as a linear operator on a vector consisting of an off-equilibrium particle distribution function that replaces the single relaxation

time parameter. Therefore, each off-equilibrium particle distribution function can relax at a different time. If this operator is diagonalizable, its eigenvalues possess an excellent interpretation as relaxation parameters act on the particle populations' modes. Some modes are physically meaningful, and intervening with them modifies the physics of the model. However, some of them are not, and they can be optimized to enhance the model's numerical stability.

2.2.3 Cumulant Model

In this study, a cumulant LBM is employed (Geier et al., 2015b). In MRT-LBM, there are statistical dependencies among the moments which limits the number of adjustable parameters. The statistical dependencies are solved by in cumulant collision model.

The discrete distribution function is denoted as f_{ijk} where $i, j, k \in \{-1, 0, 1\}$. It can be rewritten as a continuous function of macroscopic velocity $\boldsymbol{\xi} = (\xi, \upsilon, \zeta)$ using the Dirac delta function:

$$f(\xi, \upsilon, \zeta) = \sum_{i,j,k} f_{i,j,k} \delta(\xi - ic)\delta(\upsilon - jc)\delta(\zeta - kc). \tag{2.22}$$

Two-sided Laplace transform is performed to increase regularity and the resulted distribution function in frequency space $\boldsymbol{\Xi} = (\Xi, \Upsilon, Z)$ is

$$\begin{aligned} F(\boldsymbol{\Xi}) = \mathcal{L}[f(\boldsymbol{\Xi})] &= \int_{-\infty}^{\infty} f(\boldsymbol{\Xi}) e^{\boldsymbol{\Xi}\cdot\boldsymbol{\xi}} d\boldsymbol{\xi} \\ &= \sum_{i,j,k} f_{i,j,k} \mathcal{L}[\delta(\xi - ic)]\mathcal{L}[\delta(\upsilon - jc)]\mathcal{L}[\delta(\zeta - kc)] \\ &= \sum_{i,j,k} f_{i,j,k} e^{\Xi ic} e^{\Upsilon jc} e^{Zkc}. \end{aligned} \tag{2.23}$$

Eq. (2.23) is called a moment generating function. The moments of discrete distribution function f_{ijk} can be obtained from the coefficients of the Taylor expansion of the moment generating function:

$$m_{\alpha\beta\gamma} = \frac{\partial^\alpha \partial^\beta \partial^\gamma}{\partial \Xi^\alpha \partial \Upsilon^\beta \partial Z^\gamma} F(\Xi, \Upsilon, Z)\Big|_{\Xi=\Upsilon=Z=0} = \sum_{i,j,k} (ic)^\alpha (jc)^\beta (kc)^\gamma f_{i,j,k}, \tag{2.24}$$

When the set of discrete velocities is shifted with the local velocities (u, v, w), the central moment generating function can be similarly defined as

$$\begin{aligned}\hat{F}(\boldsymbol{\Xi}) &= \mathcal{L}\left[f_{i,j,k}\delta(\xi-(ic-u))\delta(\upsilon-(jc-v))\delta(\zeta-(kc-w))\right] \\ &= \sum_{i,j,k} f_{i,j,k}\mathcal{L}[\delta(\xi-(ic-u))]\mathcal{L}[\delta(\upsilon-(jc-v))]\mathcal{L}[\delta(\zeta-(kc-w))] \\ &= \sum_{i,j,k} f_{i,j,k}e^{\Xi(ic-u)}e^{\Upsilon(jc-u)}e^{Z(kc-u)}.\end{aligned} \tag{2.25}$$

The central moments are obtained as

$$k_{\alpha\beta\gamma} = \frac{\partial^\alpha\partial^\beta\partial^\gamma}{\partial\Xi^\alpha\partial\Upsilon^\beta\partial Z^\gamma}\hat{F}(\Xi,\Upsilon,Z)\Big|_{\Xi=\Upsilon=Z=0} = \sum_{i,j,k}(ic-u)^\alpha(jc-v)^\beta(kc-w)^\gamma f_{i,j,k}. \tag{2.26}$$

In order to find a group of statistically independent and Galilean invariant quantities, the coefficients of the Taylor expansion of the logarithm of the moment generating function are considered which yields the cumulants

$$C_{\alpha\beta\gamma} = \frac{\partial^\alpha\partial^\beta\partial^\gamma}{\partial\Xi^\alpha\partial\Upsilon^\beta\partial Z^\gamma} ln[F(\Xi,\Upsilon,Z)]\Big|_{\Xi=\Upsilon=Z=0} \tag{2.27}$$

Each cumulant has an individual relaxation frequency $\omega_{\alpha\beta\gamma}$ when relaxed to its equilibrium $C^{eq}_{\alpha\beta\gamma}$ in the collision process:

$$C^*_{\alpha\beta\gamma} = \omega_{\alpha\beta\gamma}C^{eq}_{\alpha\beta\gamma} + (1-\omega_{\alpha\beta\gamma})C_{\alpha\beta\gamma}, \tag{2.28}$$

where the superscript $*$ denotes the post-collision state.

2.3 Two-phase Flow Formulations

The kinetic theory-based discrete Boltzmann equation for two-phase flow can be divided into two: momentum-based formulation and velocity-based formulation. In the momentum-based formulation, the fluid pressure and fluid density are distinguish in

its equilibrium distribution function as follows:

$$f_\alpha^{eq} = w_\alpha \left[\frac{p}{c_s^2} + \rho \left(\frac{(\mathbf{e}_\alpha \cdot \mathbf{u})}{c_s^2} + \frac{(\mathbf{e}_\alpha \cdot \mathbf{u})^2}{2c_s^4} - \frac{|\mathbf{u}|}{c_s^2} \right) \right], \tag{2.29}$$

where p is the fluid pressure and ρ is the fluid density. To obtain correct two-phase hydrodynamics, the forcing term should be defined as:

$$\mathbf{F} = -\nabla(p - \rho c_s^2) + \mathbf{F}_s + \mathbf{F}_b, \tag{2.30}$$

where $\mathbf{F}$ is the external force, $\mathbf{F}_s$ is the surface tension force, and $\mathbf{F}_b$ is the body force. The first term in RHS of Eq. (2.30) means that the incorrect pressure term from the LBM kinetics is canceled out, and the correct pressure is added using the external forcing. This formulation successfully simulates two-phase flow with a high-density ratio (Lee and Lin, 2005); however, it is known that it has a large divergence error due to the cancelation error in the pressure calculation (Kim and Pitsch, 2015).

To have smaller divergence error, the velocity-based formulation is constructed, where the equilibrium function is based on the velocity and not the momentum:

$$f_\alpha^{eq} = w_\alpha \left[1 + \frac{(\mathbf{e}_\alpha \cdot \mathbf{u})}{c_s^2} + \frac{(\mathbf{e}_\alpha \cdot \mathbf{u})^2}{2c_s^4} - \frac{|\mathbf{u}|}{c_s^2} \right]. \tag{2.31}$$

In this formulation, fluid density is removed from the equilibrium distribution function, and therefore the LBM kinetics leads to a pressure-less momentum equation, and any pressure solver that can simulate incompressible flow can be used in the velocity-based formulation can be used directly without needing cancelation operation. To obtain correct two-phase hydrodynamics, the forcing term should be defined as:

$$\mathbf{F} = -\nabla p + \nu \nabla \cdot [\rho(\nabla \mathbf{u} + (\nabla \mathbf{u})^T)] + \mathbf{F}_s + \mathbf{F}_b. \tag{2.32}$$

The second term at the RHS of Eq. (2.32) is the additional viscosity term due to the density change.

2.4 Interface Capturing Methods

2.4.1 Volume of Fluid Method

The interface motion follows the fluid motion and can be described by using the advection equation of a characteristic function. In VOF, the interface is implicitly tracked by the advection of the volume fraction C, which is defined as a ratio of the liquid phase volume to the computational cell volume, where $C = 0$ denotes a gas cell, $C = 1$ denotes a liquid cell, and $0 < C < 1$ denotes an interface cell. The advection equation of the volume fraction is as follows:

$$\frac{\partial C}{\partial t} = \mathbf{u} \cdot \nabla C, \tag{2.33}$$

where $\mathbf{u}$ is the flow velocity.

The VOF is computationally friendly. Using the VOF method, one can evade using complicated mesh deformation algorithms used in FT methods. There are two approaches to solve this model, known as geometric VOF and algebraic VOF. In geometric VOF, the interface is reconstructed in each computational cell from the volume fraction field. The reconstructed interface is then advected by computing the fluxed volume across each computational cell using geometric methods. The most widely used method is the Piecewise Linear Interface Calculation (PLIC) scheme (Youngs, 1982), where the interface is approximated in each interfacial cell as a line in two dimensions or a plane in three dimensions. Algebraic VOF methods are originally developed by Hirt and Nichols (1981). In these methods, the volume fraction C is obtained with a numerical approximation such as volume-averaged, polynomial, and hyperbolic-tangent representation (Xiao et al., 2005). Although VOF can capture sharp interfaces, the method faces difficulty in simulating surface tension accurately. Therefore, another method, called the LS method, gains popularity for surface tension simulation.

2.4.2 Level Set Method

LS methods were first developed and used in computer graphics and image processing (Osher and Sethian, 1988). They were extended to the case of two-phase flows by Sussman et al. (1998). A traditional level set function is a signed-distance function $\phi(\mathbf{x}, t)$that represents the shortest distance to the interface. These methods solve the advection equation.

$$\frac{\partial \phi}{\partial t} + \mathbf{u} \cdot \mathbf{n} |\nabla \phi| = 0, \tag{2.34}$$

Eq. (2.35) commonly discretized with a Hamilton-Jacobi Weighted Essentially Non-Oscillatory (HJ-WENO) type scheme in space and a Total Variation Diminishing (TVD) scheme in time. However, ϕ loses its signed-distance property after the advection step, and hence needs to be reinitialized. Reinitialization of ϕ can be performed by solving the Eikonal equation:

$$||\nabla \phi|| = 1, \tag{2.35}$$

Level set methods offer many advantages over other methods, such as sharp interface representation and accurate computation of normals and curvature. However, they have the disadvantage that it does not conserve mass.

2.4.3 Phase-field Method

Several methods have been developed to overcome the limitation of VOF and LS. The well-known approach is to combine the LS and VOF, known as CLSVOF, where the level set is used to calculate the normal vector in the VOF calculation. The combined algorithm, however, become more complex and have reduced efficiency for parallel computation. In this dissertation, we employed an alternative method called a phase-field method that can simulate the liquid-gas interface and surface tension accurately, conserves mass, and efficient for parallel computation.

Traditionally, phase-field methods were either based on the Cahn-Hiliard (CH) or the Allen–Cahn (AC) equations. The AC equation is essentially a convection-diffusion

equation with a source term as follows:

$$\frac{\partial \phi}{\partial t} + \nabla \cdot (\mathbf{u}\phi) = \epsilon^2 \nabla^2 \phi - W'(\phi). \tag{2.36}$$

, where $\phi = -1$ and $\phi = 1$ represent the pure phases and $W(\phi) = (1 - \phi^2)^2/4$ is the mathematically approximated double-well potential. Eq. (2.36) is easy to implement and widely used in material science applications where a phase change occurs. This equation is nonconservative which limits its application for immiscible two-phase flows.

The CH equation is a more popular option within the two-phase flow community as it conserves total mass. This equation is given by:

$$\frac{\partial \phi}{\partial t} + \nabla \cdot (\mathbf{u}\phi) = -\nabla^2 [\epsilon^2 \nabla^2 \phi - W'(\phi)]. \tag{2.37}$$

Although the CH equation is conservative, handling a fourth-order spatial derivative is cumbersome. Moreover, equilibrium solutions can yield phase values other than 1 and -1 at pure phases, which is unacceptable for high-density ratio flows.

Owing to the aforementioned intrinsic deficiencies, neither the traditional phase-field equations nor the above equations are particularly suitable for the simulation of immiscible two-phase flows, which motivated researchers to try to combine the advantages of the two equations while avoiding their issues. Sun and Beckermann (2007) subtracted out the curvature-driven flow in AC to obtain a second-order PDE suitable for two-phase simulations. Later, Chiu and Lin (2011) reformulate the phase field in a conservative form giving

$$\frac{\partial \phi}{\partial t} + \nabla \cdot (\mathbf{u}\phi) = \gamma \nabla \cdot \left[\epsilon \nabla \phi - \phi(1 - \phi) \left(\frac{\nabla \phi}{|\nabla \phi|} \right) \right]. \tag{2.38}$$

In this dissertation, we employed the Conservative Phase Field (CPF) method mentioned above.

Chapter 3

Cumulant LBM for Violent Two-phase Flows

3.1 Introduction

LBM has become a popular alternative for solving the Incompressible Navier-Stokes Equations (INSE) numerically. Its popularity is due to its simple kinetic equation, derived from a particular discretization of the Boltzmann equation, which can be used to solve the INSE without solving the pressure Poisson equation (Sterling and Chen, 1996). The model is constituted of simple collision and streaming processes of particle distribution functions that can be efficiently parallelized. The implementation of its boundary conditions is also efficient, a significant reason for its popularity, especially in simulating flow in porous media. Through the Chapman-Enskog procedure, the INSE can be derived from its kinetic equation (He and Luo, 1997).

Because of its promising features, LBM is continually being extended for a wider range of applications. One such application is the simulation of two-phase flow problems, which appear in many scientific and engineering problems such as bubble and droplet dynamics (Clift et al., 1978). LBM traditionally has difficulty in simulating these problems because of the pressure-density coupling through an equation of state, allowing only a tiny density variation (He and Luo, 1997). Some early models were developed to tackle this difficulty, such as Rothman and Keller's color-gradient

(Rothman and Keller, 1988), the Shan and Chen's pseudo-potential (Shan and Chen, 1993), the Swift's free-energy (Swift et al., 1996), and the He's mean-field models (He et al., 1998). These models simulated two-phase flow problems, but their success is limited to problems with a low-density ratio, typically about 10. Therefore, many new models were developed to reduce the severity of this limitation. Some are the direct improvement of the early models such as Ba's color-gradient (Ba et al., 2016), Wu's pseudo-potential (Wu et al., 2018), and Huang and Wang's free-energy (Huang and Wang, 2018). Others are new techniques such as Lee and Lin's pressure-evolution (Lee and Lin, 2003), Inamuro's lattice kinetic (Inamuro et al., 2004), Zu and He's velocity-based formulation (Zu and He, 2013), and Wang's flux-solver (Wang et al., 2015) models, with further improvement in Fakhari's phase-field (Fakhari et al., 2016), Inamuro's improved lattice kinetic (Inamuro et al., 2016), Kim and Pitsch's (Kim and Pitsch, 2015) and Fakhari's velocity-based formulation models (Fakhari et al., 2017b). All these models were able to simulate problems with a high-density ratio, typically about 1000. Their success was mainly obtained by implementing a separate interface capturing method, better calculation of the pressure field, and a better collision model.

Despite the many successes, violent two-phase flow problems such as dam-breaking are rarely studied using two-phase LBMs. The problem is fundamental in civil and marine engineering to study the dynamics of a free surface impacting civil or marine structures. This problem is difficult to solve because its density ratio and Reynolds number are high (about 1000 and more than 10^5, respectively), and there are rapid and complex topological changes. Chen et al. (1998) has studied the dam-breaking problem using a two-phase LBM; however, in low-density ratio and Reynolds number settings (about 10 and 0.01, respectively). A similar problem, namely the wave-breaking problem, has been studied by Banari et al. (2014a) with moderate Reynolds number (about 10^4). A proposed solution, the free-surface LBM (Janssen and Krafczyk, 2010) assumes the lighter phase has negligible effects on the flow dynamics. While good for an early stage, this assumption does not hold for a later stage when bubbles and droplets appear.

Another violent two-phase flow problem is the liquid jet breakup, which is important in gas turbines, jets, and rockets development. In the LBM framework, this problem has been studied by Saito et al. (2017) and Amirshaghaghi et al. (2018), limitedly in low to moderate density ratio settings (about 100). In reality, the fuel to air density ratio can be high (about 1000).

Therefore, we propose a filtered cumulant LBM for two-phase flows and show that it is suited to solve the problem. The filtered cumulant LBM is based on a velocity-formulation model (Kim and Pitsch, 2015; Banari et al., 2014a) and is extended by employing the cumulant collision model (Geier et al., 2015b) and a second-order filter applied on the velocity field. The conservative phase-field lattice Boltzmann method (Geier et al., 2015a) is employed for the interface capturing, which guarantees mass conservation.

In Section 3.2, the governing equations for two-phase flows are described, followed by the description of the proposed two-phase LBM in Section 3.3. In Section 3.4, the proposed method is first validated using five non-violent two-phase flow problems and then employed to simulate three violent two-phase flow problems. In Section 3.5, the concluding remarks are given.

3.2 Governing equations

An immiscible, incompressible, viscous, two-fluid system is considered. Its unsteady motion is governed by the following INSE:

$$\nabla \cdot u = 0, \tag{3.1}$$

$$\frac{\partial \mathbf{u}}{\partial t} + \mathbf{u} \cdot \nabla \mathbf{u} = -\frac{1}{\rho}\nabla p + \frac{1}{\rho}\nabla \cdot \left[\mu \left(\nabla \mathbf{u} + \nabla^T \mathbf{u}\right)\right] + \frac{1}{\rho}\mathbf{F_b} + \frac{1}{\rho}\mathbf{F_s}, \tag{3.2}$$

where ρ is fluid density, $\mathbf{u}$ is fluid velocity, p is fluid pressure, μ is fluid dynamic viscosity, $\mathbf{F}_b$ is body force, $\mathbf{F}_s$ is surface tension force, and t is time. A one fluid approach is employed, where the two phases are modeled as a single fluid having

density and viscosity defined as:

$$\rho = \rho_l + \phi\left(\rho_h - \rho_l\right), \tag{3.3}$$

$$\mu = \mu_l + \phi\left(\mu_h - \mu_l\right), \tag{3.4}$$

where ϕ is a marker function distinguishing the two fluids, and the subscripts l and h indicate the light and heavy fluids, respectively. A phase-field variable is used as a smooth marker function, where $\phi = 0$ and $\phi = 1$ represent the light the heavy fluids, respectively. The motion of ϕ is governed by the conservative phase-field equation (CPFE) (Geier et al., 2015a):

$$\frac{\partial \phi}{\partial t} + \nabla \cdot \phi \mathbf{u} = \nabla \cdot \left[M \left(\nabla \phi - \frac{1 - 4\left(\phi - \frac{1}{2}\right)^2}{W} \mathbf{n} \right) \right], \tag{3.5}$$

where M, W, and $\mathbf{n}$ are the mobility parameter, the interface width, and the normal vector, respectively. Further explanations on how to solve the governing equation numerically are described in the following section.

3.3 Numerical methods

Eqs. (3.1), (3.2) and (3.5) are solved by using LBM. In LBM, instead of solving the intended equations directly, the following lattice Boltzmann equation is solved:

$$f_\alpha(\mathbf{x} + \mathbf{e}_\alpha \delta t, t + \delta t) = f_\alpha(\mathbf{x}, t) + \Omega_\alpha(\mathbf{x}, t) + F_\alpha(\mathbf{x}, t), \tag{3.6}$$

where f_α is a discrete particle distribution function (PDF) that represents the probability of finding a particle with discrete velocity $\mathbf{e}_\alpha$, Ω_α is the discrete collision operator that describes changes in f_α by means of a collision process, F_α is a forcing term, $\mathbf{x}$ is the position of the particle, and t is time.

In the following two subsections, the two LBMs employed in this paper, namely the filtered cumulant LBM and the Conservative Phase Field Lattice Boltzmann Method

(CPFLBM), are described. Both employ a D3Q27 lattice model which consists of 27 discrete velocities $\mathbf{e}_\alpha$ and weights w_α as shown in Table 2.1. The D3Q27 lattice is known to have good stability, especially for high Reynolds number flows, due to a smaller error in Galilean invariance (Suga et al., 2015), which is also the reason why the cumulant collision model was developed on this lattice (Geier et al., 2015b).

LBM was originally used to solve an incompressible single-phase flow, and in that solution, it allowed only a negligible density change (He and Luo, 1997). Special formulations are needed to support a large density change, and they can be categorized as momentum-based (Lee and Lin, 2003; Fakhari et al., 2016) or velocity-based formulations (Inamuro et al., 2016; Fakhari et al., 2017b). The difference between the two is that the first-order moment recovered from the PDFs is independent of density in the case of velocity-based formulations. Hereafter, the velocity-based formulation is used because it is more stable than the momentum-based formulation due to less incompressibility error and its semi-implicit velocity update (Kim and Pitsch, 2015).

3.3.1 Filtered cumulant LBM

A novel velocity-based formulation of two-phase LBM with a cumulant collision model and a velocity-field filter, namely a filtered cumulant LBM, is employed to solve the INSE of Eqs. (3.1) and (3.2). A cumulant collision model is employed as it has good stability for high Reynolds number problems due to statistical independence among cumulants. It has been demonstrated to stably simulate turbulent flow around a sphere with Reynolds number up to 10^5 (Geier et al., 2015b).

The cumulant LBM solves the following lattice Boltzmann equation:

$$f_{ijk(x+ic\delta t)(y+jc\delta t)(z+kc\delta t)(t+\delta t)} = f_{ijkxyzt} + \Omega_{ijkxyzt} + F_{ijkxyzt}, \tag{3.7}$$

which is Eq. (3.6) written in different notation to be consistent with Geier et al. (2015b), where $i = e_x/c$, $j = e_y/c$, $k = e_z/c$, $i, j, k \in \{1, 0, \bar{1}\}$ (Miller indices with $\bar{1} \equiv -1$ is used), $\mathbf{x} = (x, y, z)$, and $\mathbf{e} = (e_x, e_y, e_z)$. Herein, detailed descriptions such as the derivation of the cumulant model is not given and the interested readers may

refer to Geier et al. (2015b). In the following, the implementation of the proposed method is described in details.

The PDFs are first initialized from the initial macroscopic fluid velocities by using the following Maxwellian equilibrium PDFs:

$$f^{eq}_{ijkxyzt} = -X_i Y_j Z_k, \tag{3.8}$$

where eq denotes equilibrium and

$$X_0 = c_s^2 - 1 + u_x^2\Big|_{xyzt}, \tag{3.9}$$

$$X_1 = -(X_0 + 1 + u_x\Big|_{xyzt})/2, \tag{3.10}$$

$$X_{\bar{1}} = X_1 + u_x\Big|_{xyzt}, \tag{3.11}$$

where u_x is the x-component of macroscopic fluid velocity, and Y_j and Z_k are obtained analogously. At $t = 0$, $u_x\Big|_{xyzt} = u_x\Big|_{xyz0}$. These equilibrium PDFs include all terms in Mach number (Ma) that are supported by the velocity set, different from the usual polynomial type which includes terms only up to $O(Ma^2)$ (Geier et al., 2006).

It is important to note that the original Maxwellian equilibrium PDFs are:

$$f^{eq}_{ijk} = -\rho X_i Y_j Z_k, \tag{3.12}$$

where ρ is the density. The proposed method's idea is to keep the original equilibrium PDFs but set the density to unity, in the same way as Banari et al. (2014a). The zeroth-order moment is a constant, and the first-order moment is based on velocity rather than momentum. As it keeps the original equilibrium PDFs, the proposed method is distinguished from other velocity-based formulations that modify the original equilibrium PDFs (Zu and He, 2013; Inamuro et al., 2016; Kim and Pitsch, 2015; Fakhari et al., 2017b; Banari et al., 2014a). By keeping the original equilibrium PDFs, the implementation of the cumulant collision model becomes straightforward.

Next, the lattice Boltzmann kinetics are computed which consist of the collision

and streaming. Eq. (3.7) is split into collision and streaming steps as follows:

$$f^*_{ijkxyzt} = f_{ijkxyzt} + \Omega_{ijkxyzt} + F_{ijkxyzt}, \tag{3.13}$$

$$f_{ijk(x+ic\delta t)(y+jc\delta t)(z+kc\delta t)(t+\delta t)} = f^*_{ijkxyzt}, \tag{3.14}$$

where f^* is the post-collision PDF. This procedure is efficient as the collision step in Eq. (3.13) is evaluated locally and the streaming step in Eq. (3.14) is a simple shifting operation. In the single-relaxation model, Eq. (3.13) can be expanded as

$$f^*_{ijkxyzt} = (1-s)f_{ijkxyzt} + sf^{eq}_{ijkxyzt} + \left(1 - \frac{s}{2}\right) f^F_{ijkxyzt}, \tag{3.15}$$

where f^F is the forcing PDF and s is relaxation rate. The form of the forcing term is that of Guo et al. (2002), which matches the correct Navier-Stokes equations. In the cumulant collision model, Eq. (3.15) is further expanded to give the following equation in cumulant space:

$$C^*_{\alpha\beta\gamma xyzt} = (1 - s_{\alpha\beta\gamma})C_{\alpha\beta\gamma xyzt} + s_{\alpha\beta\gamma}C^{eq}_{\alpha\beta\gamma xyzt} + \left(1 - \frac{s_{\alpha\beta\gamma}}{2}\right) C^F_{\alpha\beta\gamma xyzt}, \tag{3.16}$$

where C is the cumulant, C^{eq} is the equilibrium cumulant, C^F is the forcing cumulant, and $\alpha, \beta, \gamma \in \{0, 1, 2\}$. Hereafter, following the study of Geier et al. (2015b), it is supposed that the forces act only on the first-order cumulants. In their study (Geier et al., 2015b), the forcing is applied by changing the sign of the first-order cumulants. This sign-changing operation is equal to setting the relaxation rates for the first-order cumulants to two. This setting may not be the most stable numerically, but it has the advantage that the external forces are only calculated once, namely, on the recovery of the macroscopic fluid velocity. It is possible to choose a relaxation rate less than two to improve numerical stability; however, the external forces need to be calculated twice, namely, once at the collision step and once on the recovery of the macroscopic fluid velocity. The forward transformation from PDFs to cumulants, the collision in cumulant space, and the backward transformation from cumulants to PDFs are

described in detail in Appendix A. After this collision step, the streaming step, given by Eq. (3.14), is executed. It is known through Chapman-Enskog analysis that this velocity-based formulation leads to the following pressure-less momentum equation:

$$\frac{\partial \mathbf{u}}{\partial t} + \mathbf{u} \cdot \nabla \mathbf{u} = \nabla \cdot \left[\nu \left(\nabla \mathbf{u} + \nabla^T \mathbf{u} \right) \right] + \frac{1}{\rho} \mathbf{F}, \tag{3.17}$$

where $\mathbf{F}$ is the external force exerted on the fluid (Banari et al., 2014b). Moreover, pressure is completely decoupled from the LBM kinetics. The momentum equation must therefore be corrected, and the pressure equation must be constructed.

The momentum is conserved as LBM's collision and streaming processes conserve the momentum. Eq. (3.17) is different from the target Eq. (3.2) which can be rewritten by expanding the viscous term as:

$$\frac{\partial \mathbf{u}}{\partial t} + \mathbf{u} \cdot \nabla \mathbf{u} = -\frac{1}{\rho} \nabla p + \frac{1}{\rho} \nabla \cdot \left[\nu \rho \left(\nabla \mathbf{u} + \nabla^T \mathbf{u} \right) \right] + \frac{1}{\rho} \mathbf{F_b} + \frac{1}{\rho} \mathbf{F_s}, \tag{3.18}$$

$$\begin{aligned} \frac{\partial \mathbf{u}}{\partial t} + \mathbf{u} \cdot \nabla \mathbf{u} = & -\frac{1}{\rho} \nabla p + \nabla \cdot \left[\nu \left(\nabla \mathbf{u} + \nabla^T \mathbf{u} \right) \right] \\ & + \frac{\nu}{\rho} \left(\nabla \mathbf{u} + \nabla^T \mathbf{u} \right) \cdot \nabla \rho + \frac{1}{\rho} \mathbf{F_b} + \frac{1}{\rho} \mathbf{F_s}, \end{aligned} \tag{3.19}$$

To obtain the intended momentum equation, the missing terms are added as body forces which makes the formulation partially conservative. Away from the interface, the density is constant and the additional viscous and surface tension terms disappear, thus the formulation becomes conservative. At the interface, the formulation is not conservative because of the additional terms. However, when the viscosity is very low, the contribution of the additional viscous term can be neglected.

To add the pressure term to the momentum equations, the following force is added:

$$\mathbf{F}_p = -\nabla p, \tag{3.20}$$

where $\mathbf{F}_p$ is the pressure force. The viscosity term is also corrected by adding the following force:

$$\mathbf{F}_\nu = \nu \left(\nabla \mathbf{u} + \nabla^T \mathbf{u} \right) \cdot \nabla \rho, \tag{3.21}$$

where $\mathbf{F}_\nu$ is the additional viscous force. The body force due to gravity is calculated as:

$$\mathbf{F_b} = \rho \mathbf{g}, \tag{3.22}$$

where $\mathbf{g}$ is the gravity acceleration. The surface tension force is modeled by the density-scaled continuous surface force model (Brackbill et al., 1992):

$$\mathbf{F_s} = \sigma \kappa \frac{\nabla \rho}{[\rho]} \frac{\rho}{\langle \rho \rangle}, \tag{3.23}$$

where σ is the surface tension, κ is the curvature defined as:

$$\kappa = -\nabla \cdot \mathbf{n}, \tag{3.24}$$

and

$$[\rho] = \rho_h - \rho_l, \tag{3.25}$$

$$\langle \rho \rangle = \frac{1}{2} \left(\rho_h + \rho_l \right). \tag{3.26}$$

The normal vector $\mathbf{n}$ is calculated as:

$$\mathbf{n} = \frac{\nabla \phi}{|\nabla \phi| + \epsilon}, \tag{3.27}$$

where ϵ is a small number which is added to prevent a division by zero. In this study, $\epsilon = 10^{-40}$ was employed for double-precision calculations. The density-scaled model has better stability than the original model as it shifts the force distribution to higher density regions and therefore reduces the acceleration of the lighter phase which may cause the instability (Brackbill et al., 1992). Finally, the forces are summed:

$$\mathbf{F} = \mathbf{F}_p + \mathbf{F}_\nu + \mathbf{F}_b + \mathbf{F}_s. \tag{3.28}$$

The gradient of an arbitrary variable ψ used in (3.20), and (3.21), and Eqs. (3.23)

is approximated as (Kim and Pitsch, 2015):

$$\nabla\psi(\mathbf{x}) = \frac{1}{c_s^2\delta t}\sum_\alpha w_\alpha \mathbf{e}_\alpha \left[\psi(\mathbf{x}+\mathbf{e}_\alpha\delta t) - \psi(\mathbf{x},t)\right]. \tag{3.29}$$

It is also worth to know that in (Geier et al., 2015b), the cumulant collision operator can be made well-conditioned to reduce the round-off error. However, it is not employed here as it requires more operations.

After the post-collision PDFs have been obtained, they are advected using Eq. (3.14). The pressure at time step $n+1$ is then calculated from the PDFs as follows:

$$p^{n+1} = p^n - \rho^{n+1}c_s^2\nabla\cdot\mathbf{u}. \tag{3.30}$$

In this formulation, the velocity divergence is recovered as follows:

$$\sum_\alpha f_\alpha(\mathbf{x},t+\delta t) = \sum_\alpha f_\alpha^*(\mathbf{x}-\mathbf{e}_\alpha\delta t,t). \tag{3.31}$$

$$\sum_\alpha f_\alpha(\mathbf{x},t+\delta t) - \sum_\alpha f_\alpha^*(\mathbf{x},t) = \sum_\alpha \left[f_\alpha^*(\mathbf{x}-\mathbf{e}_\alpha\delta t,t) - f_\alpha^*(\mathbf{x},t)\right], \tag{3.32}$$

Note that the equilibrium of zeroth order moment is enforced in the collision step, therefore:

$$\sum_\alpha f_\alpha(\mathbf{x},t+\delta t) - \sum_\alpha f_\alpha^{eq}(\mathbf{x},t) = \sum_\alpha \left[f_\alpha^*(\mathbf{x}-\mathbf{e}_\alpha\delta t,t) - f_\alpha^*(\mathbf{x},t)\right], \tag{3.33}$$

$$\sum_\alpha f_\alpha(\mathbf{x},t+\delta t) - 1 = -\nabla\cdot\mathbf{u} + O(Ma^2). \tag{3.34}$$

In this formulation, as the velocity divergence is calculated directly from the PDFs, the predictor-corrected steps in (Kim and Pitsch, 2015) are not required.

To enhance the stability, a second order filter is applied to the pressure field (Kim and Pitsch, 2015):

$$\bar{p}(x) = \sum_\alpha w_\alpha p(\mathbf{x}+\mathbf{e}_\alpha\delta t). \tag{3.35}$$

The pressure force is then updated by using

$$\bar{\mathbf{F}}_p^{n+1} = -\nabla \bar{p}, \tag{3.36}$$

and the macroscopic fluid velocity is updated semi-implicitly as follows:

$$\mathbf{u}^{n+1} = \sum_\alpha \mathbf{e}_\alpha f_\alpha + \frac{\mathbf{F}^{n+1}}{2\rho}\delta t = \sum_\alpha \mathbf{e}_\alpha f_\alpha + \frac{1}{2\rho}\left(\bar{\mathbf{F}}_p^{n+1} + \mathbf{F}_\nu^n + \mathbf{F}_b^n + \mathbf{F}_s^n\right)\delta t. \tag{3.37}$$

This formulation has recovered the INSE of Eq. (3.2) with the following pressure equation:

$$\frac{1}{\rho c_s^2}\frac{\partial p}{\partial t} + \nabla \cdot \mathbf{u} = O(Ma^2), \tag{3.38}$$

To satisfy the incompressible flow condition (Eq. (3.1)), the Mach number should be kept low:

$$Ma = \frac{|u|}{c_s} \ll 1, \tag{3.39}$$

i.e.:

$$\frac{|u|\delta t}{\delta x} \ll \frac{1}{\sqrt{3}}, \tag{3.40}$$

Hereafter, this formulation is referred as the unfiltered cumulant LBM as the velocity field is unfiltered.

To further enhance its stability for violent two-phase flow, the following second order filter is applied to the velocity field:

$$\begin{aligned}\mathbf{F_a} = \frac{\rho}{2}\frac{\delta t}{\delta x^2}(&|u_{xi+1/2,j,k}|D_{i+1/2,j,k} - |u_{xi-1/2,j,k}|D_{i-1/2,j,k} \\ &+ |u_{y_{i,j+1/2,k}}|D_{i,j+1/2,k} - |u_{y_{i,j-1/2,k}}|D_{i,j-1/2,k} \\ &+ |u_{zi,j,k+1/2}|D_{i,j,k+1/2} - |u_{zi,j,k-1/2}|D_{i,j,k-1/2}),\end{aligned} \tag{3.41}$$

with

$$D_{i+1/2,j,k} = \begin{cases}\mathbf{u}_{i,j,k} - \mathbf{u}_{i-1,j,k}, & \text{if } Pe \geq 2 \\ 0, & \text{otherwise}\end{cases} \tag{3.42}$$

$$Pe_{i+1/2,j,k} = \left| \frac{u_x \delta x}{\nu} \right|_{i+1/2,j,k}, \tag{3.43}$$

where i, j, k are the node index in x-, y-, z-direction, respectively. u_x, u_y, u_z are the x-, y-, z-velocity components, respectively. The values at the half gridpoints are obtained using linear interpolation. In this formulation, artificial viscosity is added depending on the Peclet number Pe through additional force term $\mathbf{F_a}$ (added to Eq. (3.28)), analogously to the hybrid differencing scheme for advection equation (Spalding, 1972). This formulation is referred as the filtered cumulant LBM. As the artificial viscosity is added as separate filter, it can be turned-off easily and thus the solver can be adapted to handle both violent and non-violent flows.

Herein, we would like to highlight the main differences between the proposed methods and several two-phase LBMs. First, most of the well-known two-phase LBMs are based on momentum-based formulation (Lee and Lin, 2003; Fakhari et al., 2016), whereas our proposed method is based on velocity-based formulation. As studied by Kim and Pitsch (2015), the momentum-based will suffer from higher divergence error.

Perhaps the first to propose a velocity-based formulation is Inamuro et al. (2004) using Lattice Kinetic Scheme (LKS) which is LBM with relaxation rate equal to one. The relaxation rate contribution to the momentum equations' viscous term is canceled by modifying the equilibrium function, and the correct viscous term is added through external force. In their method, the Poisson solver was employed to obtain the pressure field against LBM's original benefit. Their method was improved by Banari et al. (2014a). They replaced the LKS with the original LBM to improve the viscous term representation. However, in their other paper (Banari et al., 2014b), they essentially returned to LKS to simulate wave breaking problems. It seems that by using LKS, artificial viscosity is introduced and stabilizes the computation. Poisson solver was also employed by Banari et al. (2014a). Later, Inamuro et al. (2016) switched to LKS with pressure evolution equation.

Zu and He (2013) developed a velocity-based formulation for LBM. Similarly, a velocity-based formulation was developed by Kim and Pitsch (2015). Both methods

distinguish the distribution function at rest and the others. For Zu and He's method, a pressure correction term must be added through external forces to get the correct pressure term in the momentum equation, whereas for Kim and Pitch's method, the pressure term is calculated directly. The pressure field calculation in Zu and He's method is not described physically, whereas, in Kim and Pitch's method, the pressure evolution equation is recovered. In both methods, the velocity and pressure are coupled; therefore, a predictor-corrector scheme is required to update the pressure and velocity fields.

Fakhari improved Zu and He's method (Fakhari et al., 2017b). Fakhari's formulation is promising as it does not require a predictor-corrector scheme and improves the locality of the two-phase LBM by calculating the stress tensor for the additional viscous term from the distribution functions. In the same manner as Zu and He's method, a pressure correction term must be added, whereas in our proposed method, the pressure term is calculated directly. The pressure field calculation in Fakhari's method is not described physically, whereas the pressure evolution equation is recovered from our proposed method.

In our method, the pressure and momentum equations are decoupled. One can update the pressure using any working methods, for example, using Poisson solver. However, in our proposed method, we chose to recover the velocity divergence from LBM kinetics and then formulate the pressure evolution equation. In this way, our method also does not require a predictor-corrector scheme.

Lastly, our proposed method employs a cumulant collision model. Fakhari extended his method from 2D to 3D, which employs a weighted multi relaxation time (MRT) collision model to simulate the two-phase flows stably (Fakhari et al., 2017a). The weighted MRT changes the inner product among moments by giving weights to the product to reduce the coupling between moments. The coupling between moments is avoided in the cumulant collision model because of the statistical independence between cumulants.

3.3.2 Conservative phase-field lattice Boltzmann method

To capture the interface dynamics, the following CPFLBM (Geier et al., 2015a) is employed to solve Eq. (3.5):

$$h_\alpha(\mathbf{x}+\mathbf{e}_\alpha\delta t, t+\delta t) - h_\alpha(\mathbf{x},t) = -\frac{1}{\tau_\phi}\left(h_\alpha(\mathbf{x},t) - h_\alpha^{eq}(\mathbf{x},t)\right), \tag{3.44}$$

which is Eq. (3.6) written in different notation, where h_α and τ_ϕ are the distribution function and the relaxation time for CPFLBM, respectively. The collision operator is expressed by single relaxation time model.

The interface spans between several mesh points ($W \approx 3$ mesh points). At equilibrium, the phase-field variable assumes a hyperbolic tangent profile:

$$\phi = \frac{1}{2}\left[1 + \tanh\left(\frac{2s}{W}\right)\right], \tag{3.45}$$

where s is the signed distance function of the interface located at $s = 0$. This profile is also used as initial profile.

The equilibrium PDFs for CPFLBM is defined slightly differently from its original paper (Geier et al., 2015a) as the second order term is neglected:

$$h_\alpha^{eq} = w_\alpha\left(\phi\left[1 + \frac{\mathbf{e}_\alpha\cdot\mathbf{u}}{c_s^2}\right] + \frac{M}{W}\left[1 - 4\left(\phi - \frac{1}{2}\right)^2\right]\frac{\mathbf{e}_\alpha\cdot\mathbf{n}}{c_s^2}\right). \tag{3.46}$$

The normal vector is calculated using Eqs. (3.27) and (3.29). The equilibrium PDFs are also used as the initial PDFs.

Eq. (3.44) is solved in two steps, analogously to Eqs. (3.13) and (3.14):

$$h_\alpha^*(x,t) = h_\alpha(x,t) - \frac{1}{\tau_\phi}\left(h_\alpha(x,t) - h_\alpha^{eq}(x,t)\right), \tag{3.47}$$

$$h_\alpha(\mathbf{x}+\mathbf{e}_\alpha\delta t, t+\delta t) = h_\alpha^*(x,t). \tag{3.48}$$

The relaxation time for CPFLBM is defined as:

$$\tau_\phi = M c_s^2 \frac{\delta t}{\delta_x^2} + \frac{1}{2}. \tag{3.49}$$

Finally, the phase-field variable is computed as:

$$\phi = \sum_\alpha h_\alpha. \tag{3.50}$$

3.3.3 Boundary conditions

The no-slip boundary condition is realized by setting zero velocities and zero normal gradients of phase-field variable and pressure at the boundary. For PDFs, the half-way bounce-back scheme is applied.

The free-slip boundary condition is realized by setting zero normal velocity and zero normal gradients of phase-field variable and pressure at the boundary. For PDFs, the specular reflection scheme is applied (Succi, 2002).

The inflow boundary condition is realized by setting fixed velocities and phase-field variables and zero normal gradients of pressure at the boundary. For PDFs, Guo's scheme is employed (Zhao-Li et al., 2002).

The open boundary condition is realized by setting zero normal gradients of velocities, phase-field variables, pressure, and PDFs at the boundary. A reflective boundary is applied for the normal vector in all conditions.

3.3.4 Algorithm of computation

The algorithm of computation is summarized as follows:

Step 1: Initialize the macroscopic variables: phase-field variable $\phi(\mathbf{x}, 0)$ (Eq. (3.45)), normal vector $\mathbf{n}(\mathbf{x}, 0)$ (Eq. (3.27)), density $\rho(\mathbf{x}, 0)$ (Eq. (3.3)), viscosity $\mu(\mathbf{x}, 0)$ (Eq. (3.4)), pressure $p(\mathbf{x}, 0)$, and macroscopic velocity $\mathbf{u}(\mathbf{x}, 0)$.

Step 2: Initialize the PDFs: $h(\mathbf{x}, 0)$ for the CPFLBM (Eq. (3.46)) and $f(\mathbf{x}, 0)$ for the cumulant LBM (Eq. (3.12)).

Step 3: Compute the post-collision distribution functions (collision step): $h^*(\mathbf{x}, t)$ (Eq. (3.47)) and $f^*(\mathbf{x}, t)$ (Eqs. (A.1) – (A.46)). The velocity field filter is added to the external forces.

Step 4: Update the distribution functions (boundary conditions and streaming steps): $h(\mathbf{x}, t + \delta t)$ (Eq. (3.48)) and $f(\mathbf{x}, t + \delta t)$ (Eq. (3.14)).

Step 5: Update the phase-field variable $\phi(\mathbf{x}, t + \delta t)$ (Eq. (3.50)).

Step 6: Update density $\rho(\mathbf{x}, t + \delta t)$ (Eq. (3.3)), viscosity $\mu(\mathbf{x}, t + \delta t)$ (Eq. (3.4)).

Step 7: Update the pressure $p(\mathbf{x}, t + \delta t)$ (Eq. (3.30)).

Step 8: Filter the pressure field (Eq. (3.35)).

Step 9: Update the velocity $\mathbf{u}(\mathbf{x}, t + \delta t)$ (Eq. (3.37)). The velocity field filter is added to the external forces.

Step 10: Advanced time step and return to **Step** 3.

3.4 Results and discussions

In this section, the proposed method is first validated using five non-violent two-phase flow problems: a 2D Rayleigh-Taylor instability, a 2D falling droplet, a 2D rising bubble, a 3D oblique coalescence of two bubbles, and a 3D droplet splashing on a thin film. The proposed method is then employed to simulate three violent two-phase flow problems: a 3D dam-breaking on a dry floor, a 3D dam-breaking on a wet floor, and a 3D liquid jet breakup. Along with the proposed method, the results from the unfiltered cumulant LBM are provided for comparisons.

Computational domains are divided into cubic lattices with lattice spacing and time interval $\delta x = \delta t = 1$. Physical values are transformed into lattice values in the following way:

$$\nu' = \nu \cdot \frac{\Delta t}{\Delta x^2}, \tag{3.51}$$

$$\sigma' = \sigma \cdot \frac{\Delta t^2}{\rho_l \Delta x^3}, \tag{3.52}$$

$$g' = g \cdot \frac{\Delta t^2}{\Delta x}, \tag{3.53}$$

where ν, σ, g, Δx, Δt are the kinematic viscosity, the surface tension, the gravity acceleration, grid spacing, and time interval, respectively.

Interface width $W = 3$, mobility $M = 1/12$ in lattice units, and maximum Mach number (overall gridpoints) ($Ma_{max} < 0.3$) are used for all problems. Although the interface width and mobility values are a bit diffusive, they offer good stability for this preliminary study. As a note, physical units are used throughout the following subsections.

3.4.1 2D Rayleigh-Taylor instability

The proposed method's validity at a low-density ratio and without surface tension effect is examined by simulating a 2D Rayleigh-Taylor instability problem. As a reference, the work by Hermann (Herrmann, 2008) is considered where the problem is solved using the refined level set grid method for the interface capturing and the fractional-step method for collocated variables on unstructured grids for the INSE solver.

The initial conditions of the problem are shown in Fig. 3-1. A heavy fluid (marked by Ω_h in the figure) with density $\rho_h = 1.225$ and dynamic viscosity $\mu_h = 0.00313$ is placed above a light fluid Ω_l with density $\rho_l = 0.1694$ and dynamic viscosity $\mu_l = 0.00313$. The gravity acceleration is set to $g = 9.81$. The fluid interface is located at $y = L_y/2$ and is perturbed by the following function:

$$y = 0.05 \cos(2\pi x). \tag{3.54}$$

Note that the physical values are hypothetical as given in the reference.

The Reynolds number and Atwood number (a relative density difference between

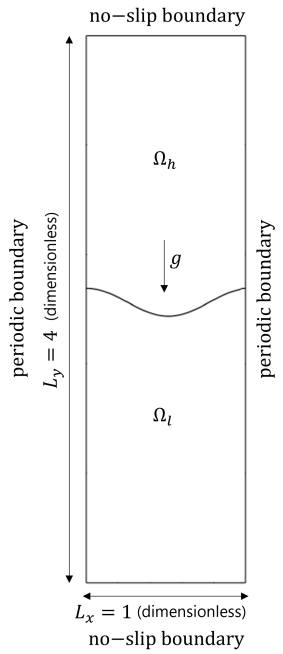

Figure 3-1: Schematic of initial condition of the 2D Rayleigh-Taylor instability problem.

two fluids) of this problem are calculated as follows:

$$Re = \frac{\rho_h \sqrt{g}}{\mu_h} \approx 1200, \tag{3.55}$$

$$At = \frac{\rho_h - \rho_l}{\rho_h + \rho_l} = 0.76, \tag{3.56}$$

The problem was solved using both unfiltered and filtered cumulant LBM with $\omega_1 = 1$ up to the time $T = 0.9$ with four different mesh resolutions $\Delta x = 1/128$, $\Delta x = 1/256$, $\Delta x = 1/512$, $\Delta x = 1/1024$ and corresponding time intervals $\Delta t = 1/20000$, $\Delta t = 1/40000$, $\Delta t = 1/80000$, $\Delta t = 1/160000$. The body force is calculated as $F_b = -\rho g$. Periodic boundaries are applied to the left and right boundaries. D3Q27 lattice model is employed and therefore in this problem, the mesh depth is set to a single gridpoint with free-slip boundaries. The reference uses mesh resolutions $\Delta x = 1/512$.

Fig. 3-2 shows the evolution of the interface shape obtained with a mesh resolution $\Delta x = 1/512$ from both reference and the proposed method. At this resolution, the

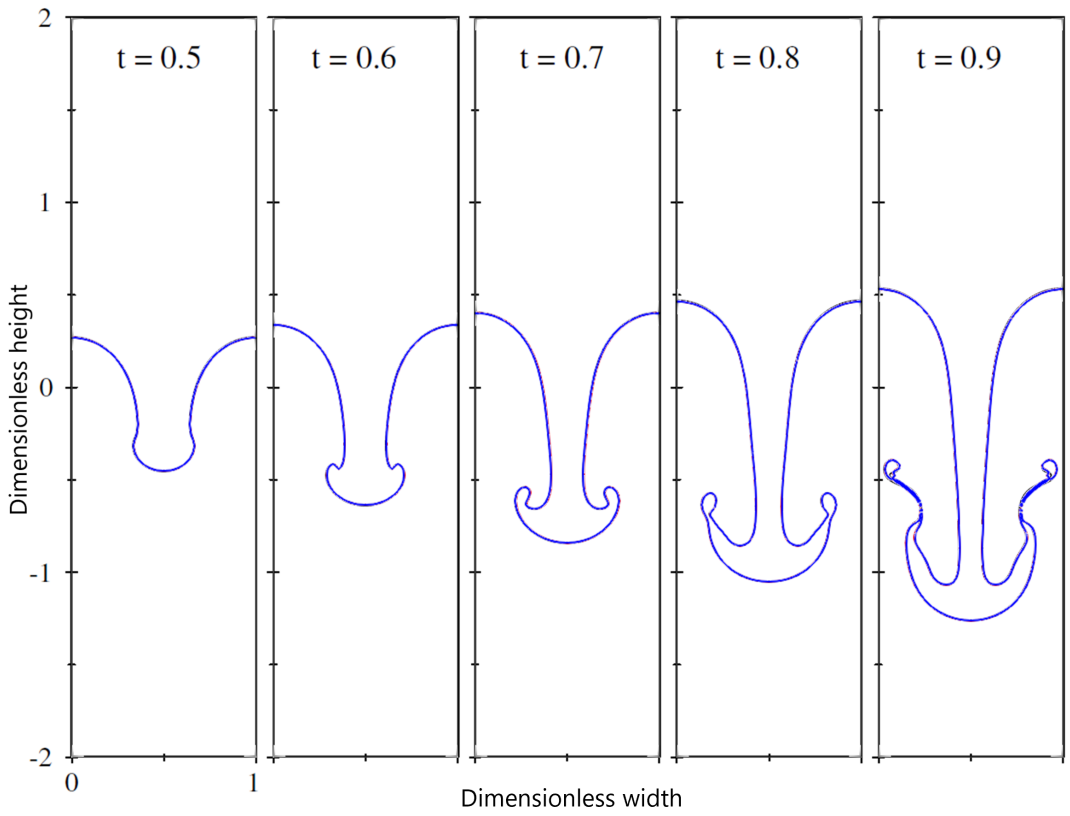

Figure 3-2: Evolution of the interface shape in 2D Rayleigh – Taylor instability problem with $\Delta x = 1/512$. Herrmann (black), unfiltered cumulant LBM (red), filtered cumulant LBM (blue). Adapted from (Herrmann, 2008).

interface shapes obtained by both unfiltered and filtered cumulant LBM agree very well with the reference at all times.

Fig. 3-3 shows the interface shapes at the final time for various mesh resolutions. Different interface shapes were obtained by the unfiltered and filtered cumulant LBM, where the latter one is more diffusive, as seen by the penetration depth and the tail shape. The difference is pronounced at low resolution. A grid convergence, however, is observed in both cases. Although subgrid-scale turbulence model (Amirshaghaghi et al., 2018) or higher-order filters (Ricot et al., 2009; Hejranfar and Ezzatneshan, 2015) can reach better accuracy in this problem, they are not always stable for violent two-phase flow problems in the authors' experience and therefore require further studies.

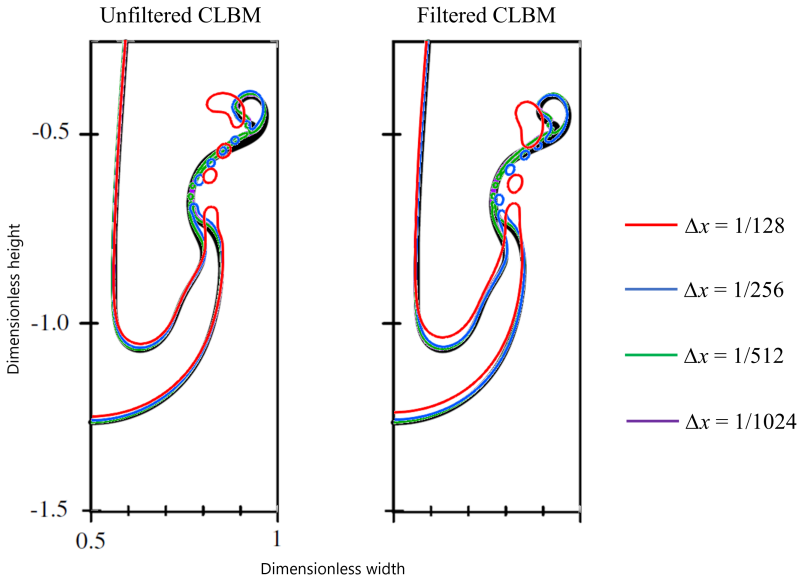

Figure 3-3: Interface shapes at final time for various mesh sizes in 2D Rayleigh – Taylor instability problem. Unfiltered cumulant LBM (left) filtered cumulant LBM (right). Herrmann's result is shown as background (black). Adapted from (Herrmann, 2008).

3.4.2 2D droplet falling

The proposed method is based on the velocity-based formulation, and to compare its accuracy with the momentum-based formulation, the 2D droplet falling problem is considered, as most of the momentum comes from the moving droplet in this problem. As a reference, the work by Fakhari *et al.*. (Fakhari et al., 2017b) is considered which solved the problem using a momentum-based two-phase LBM.

Initially, a circular droplet (heavy fluid) with diameter D, density ρ_h, and dynamic viscosity μ_h is placed at $[2.5D, 12.5D]$ and surrounded by a light fluid with density ρ_l and dynamic viscosity μ_l in a rectangular domain of size $[5D \times 15D]$. The bottom and top boundaries are no-slip, while the left and right boundaries are periodic.

The density ratio, Reynolds number, Eotvos number (the ratio of gravitational to surface tension forces), and dimensionless time of this problem are calculated as follows:

$$r_\rho = \frac{\rho_h}{\rho_l} = 10, \tag{3.57}$$

$$Re = \frac{\sqrt{g_y \rho_h (\rho_h - \rho_l) D^3}}{\mu_h} = 10, \tag{3.58}$$

$$Eo = \frac{\rho_h g_y D^2}{\sigma} = 100, \tag{3.59}$$

$$t^* = t\sqrt{\frac{g_y}{D}}. \tag{3.60}$$

where g_y is the magnitude of the gravitational acceleration in the y-direction and σ is the surface tension.

The simulation was carried using unfiltered and filtered cumulant LBM with $\omega_1 = 1$ up to $T^* = 9$ with the mesh size $N_x \times N_y = 512 \times 1536$ and the number of time steps $N_t = 33750$. The body force is calculated as $F_b = -(\rho - \rho_l) g_y$. In this problem also, the mesh depth is set to a single gridpoint with free-slip boundaries for our proposed method.

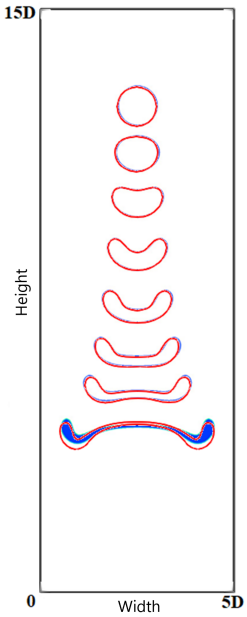

Figure 3-4: Evolution of droplet shapes in 2D falling droplet problem at $t^* = 2$, $t^* = 3$, $t^* = 4$, $t^* = 5$, $t^* = 6$, $t^* = 7$, and $t^* = 9$. Reference (blue) and filtered cumulant LBM (red). Adapted from (Fakhari et al., 2017b)

In this problem only, we modify the interface width to $W = 4.096$, mobility to $M = 0.056$ in lattice units, and the calculation of surface tension force, following the reference so that any differences may be restricted to the error in momentum

conservation.

The evolution of the falling droplet is shown in Fig. 3-4. The interface shapes in blue and red are obtained by the reference and the proposed method, respectively. Due to the low Reynolds number, the results from the unfiltered and filtered cumulant LBM are the same. The proposed method can capture the bag breakup and agrees quite well with the reference most of the time. The difference is pronounced at the final time when a thin film develops. Perhaps the difference can be attributed to the error in momentum conservation.

3.4.3 2D rising bubble

The proposed method's capacity in simulating two-phase flows with high-density ratio and surface tension is analyzed by simulating a 2D rising bubble problem. The present technique is benchmarked against two Finite Element Method (FEM) solvers: TP2D (FEM with a level set for interface tracking) (Hysing et al., 2009) and Abels' model (FEM with Cahn-Hilliard for interface tracking) (Aland and Voigt, 2012). The prior one is based on the sharp-interface model, whereas the latter is based on the diffuse-interface model.

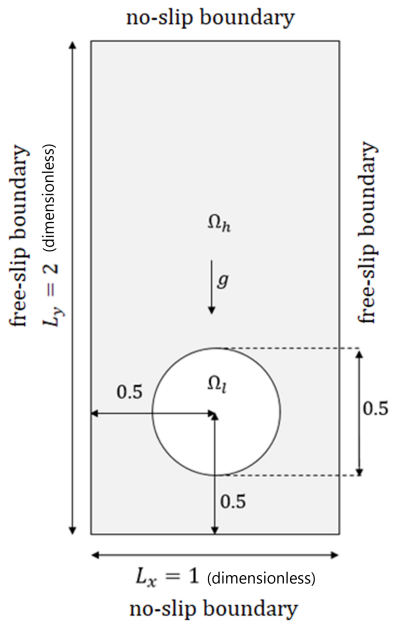

Figure 3-5: Schematic of initial condition of the 2D rising bubble problem.

Fig. 3-5 shows the problem setup, where a bubble of lighter fluid (in Ω_l) is surrounded by a heavier fluid (in Ω_h). As the simulation progresses, the bubble rises, and its shape evolves according to the given physical parameters. Two cases were simulated with the physical parameters, and dimensionless numbers are shown in Table 3.1. Note that the physical values are only hypothetical as given by the reference (Hysing et al., 2009).

The Reynolds number and Eotvos number of this problem are calculated as follows:

$$Re = \frac{\rho_h D\sqrt{gD}}{\mu_h}, \tag{3.61}$$

$$Eo = \frac{\rho_h g D^2}{\sigma}, \tag{3.62}$$

where D is the bubble's diameter. Case 2 is considered more difficult than Case 1, where more complex bubble shape with thin filaments is expected due to the higher density ratio and Eotvos numbers.

Table 3.1: Physical parameters (non-dimensional unit) and dimensionless numbers in 2D rising bubble problem.

Case	ρ_h	ρ_l	μ_h	μ_l	g	σ	Re	Eo	ρ_h/ρ_l	μ_h/μ_l
1	1000	100	10	1	0.98	24.5	35	10	10	10
2	1000	1	10	0.1	0.98	1.96	35	125	1000	100

The problem was solved using unfiltered and filtered cumulant LBM with $\omega_1 = 2$ up to the time $T = 3.0$ with mesh resolution $\Delta x = 1/320$ and time interval $\Delta t = 1/20000$. The body force is calculated as $F_b = -\rho g$. The reference TP2D and Abels' models use mesh resolutions $\Delta x = 1/320$ and $\Delta x = 1/128$, respectively. Analogously to Subsection 3.4.1, the mesh depth is set to a single gridpoint with free-slip boundaries. In this setting, both unfiltered and filtered cumulant LBM produces the same result as the Reynolds number is low.

Fig. 3-6 shows the benchmark results for Case 1. The bubble shapes at the final time from the proposed method agree very well with the references. Its rise velocity, however, oscillates about a mean value. This oscillation occurs due to compressibility effects where pressure waves travel with the speed proportional to the sound speed.

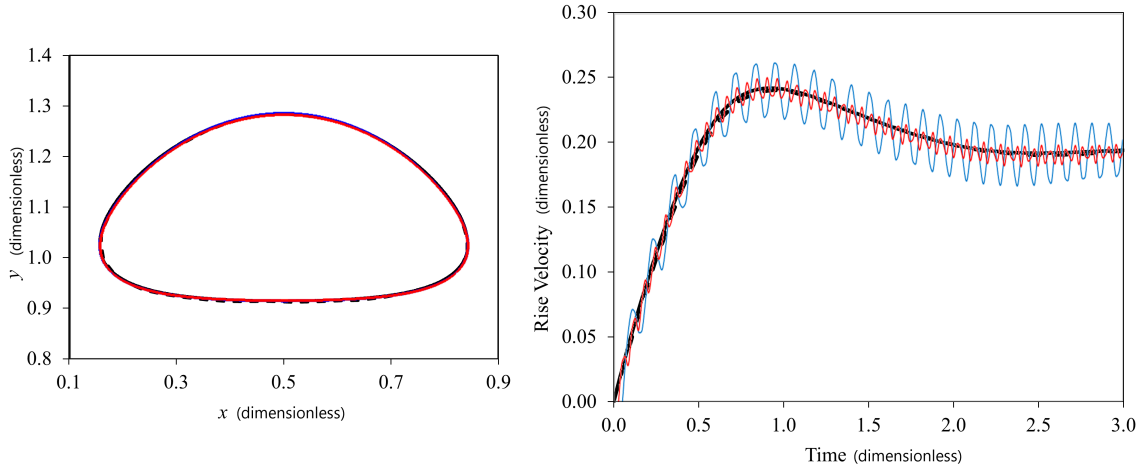

Figure 3-6: Bubble shapes at final time (left) and rise velocity (right) for Case 1 of the 2D rising bubble problem. Filtered cumulant LBM with $Ma_{max} = 0.007$ (red), filtered cumulant LBM with $Ma_{max} = 0.014$ (blue). References: TP2D (Hysing et al., 2009) (solid black) and Abels (Aland and Voigt, 2012) (dashed black).

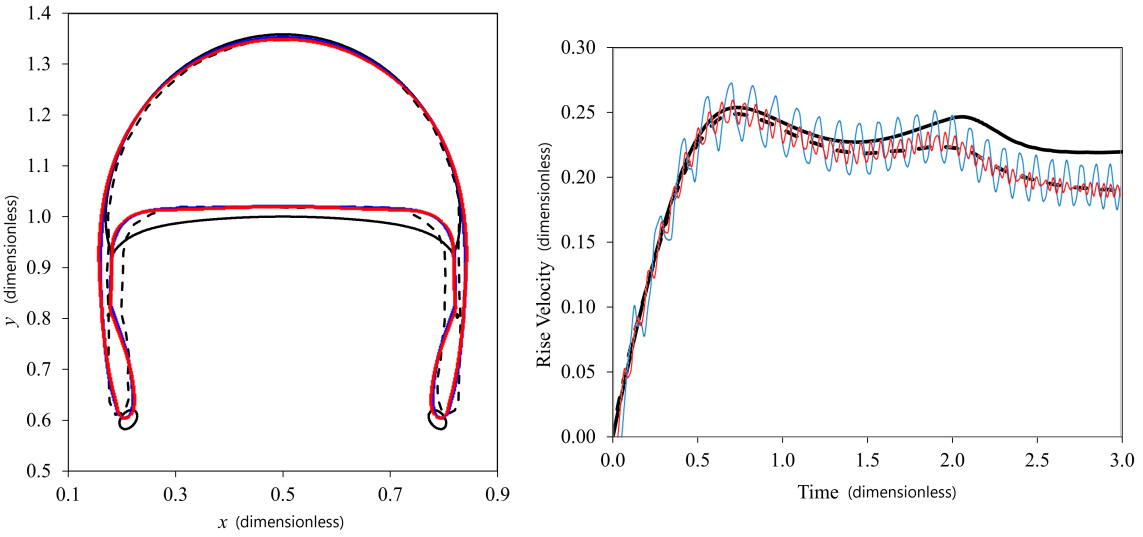

Figure 3-7: Bubble shapes at final time (left) and rise velocity (right) for Case 2 of the 2D rising bubble problem. Filtered cumulant LBM with $Ma_{max} = 0.012$ (red), filtered cumulant LBM with $Ma_{max} = 0.024$ (blue). References: TP2D (Hysing et al., 2009) (solid black) and Abels (Aland and Voigt, 2012) (dashed black).

The oscillation can be reduced by reducing the Mach number. The mean value of the rise velocity, however, is in good agreement with the references.

Fig. 3-7 shows the benchmark results for Case 2. The bubble shapes at the final time from the proposed method differ from the references, mainly on the bubble's

bottom and skirt shape. A better agreement, however, is obtained with the reference diffuse-interface model (Abels' model). The proposed method belongs to a diffuse-interface model where the interface spans several gridpoints. The difference may also be due to the difference in the calculation of surface tension force: the present algorithm uses the curvature from the phase-field function, whereas TP2D uses a level set function and Abels' model uses a chemical potential model. The decrease of Mach number has a slight effect on the bubble shapes; however, it reduces the rise velocity's oscillation.

3.4.4 3D oblique coalescence of two bubbles

The 3D oblique coalescence of two bubbles problem is considered. This setting has been studied both experimentally by Brereton and Korotney (Brereton and Korotney, 1991) and numerically by van Sint Annaland et al. (2005) using a finite difference method (FDM) with a volume of fluid (VOF) for interface tracking.

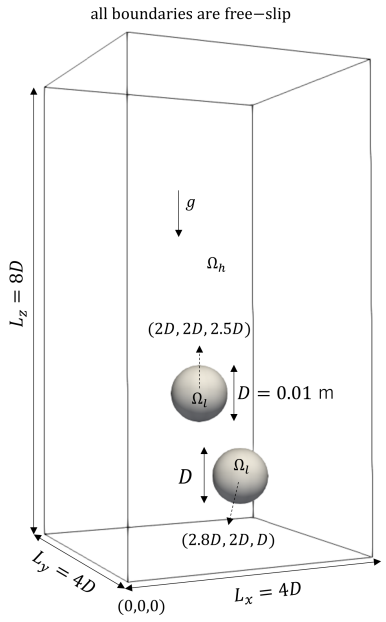

Figure 3-8: Schematic of initial condition of the 3D oblique coalescence of two bubbles.

The schematic of the problem is shown in Fig. 3-8. Two spherical bubbles, identical in size with diameter $d = 0.01$ m, are arranged in oblique configuration as shown in

the figure. The density and viscosity of the heavier fluid are $\rho_h = 100$ kg/m^3 and $\mu_h = 4.63 \times 10^{-3}$ kg/(m $\cdot$ s), whereas the density and viscosity of the lighter fluid are $\rho_l = 1$ kg/m^3 and $\mu_h = 4.63 \times 10^{-5}$ kg/(m $\cdot$ s). The Morton and Eotvos numbers for this case are defined as:

$$Mo = \frac{g\mu_h^4 \Delta\rho}{\rho_h^2 \sigma^3} = 2 \times 10^{-4}, \tag{3.63}$$

$$Eo = \frac{\Delta\rho g d^2}{\sigma} = 16, \tag{3.64}$$

where g is the gravity, σ is the surface tension, and $\Delta\rho = \rho_h - \rho_l$.

The problem is solved using both unfiltered and filtered cumulant LBM with $\omega_1 = 2$ on a mesh of $N_x \times N_y \times N_z = 80 \times 80 \times 160$ gridpoints, where N_x, N_y, N_z are the number of mesh in x-, y-, z-direction, respectively, and $N_t = 4000$ time steps. In this problem, the body force is calculated in term of volumetric buoyancy force $F_b = (\rho - \rho_h)g$ as in (Fakhari et al., 2016). This model is valid when the lighter fluid is surrounded by the heavier fluid.

Fig. 3-9 shows the evolution of the bubble shapes obtained from the simulations compared to the reference. The proposed method shows the trailing bubble's catch-up with the leading bubble, which leads to significant deformation of the trailing bubble and the tilting of the leading bubble. A mushroom-like shape is shown at $t = 1.5$ s and an oblique coalesce is shown at $t = 2.0$ s.

Fig. 3-10 shows the evolution of the rise velocities (average of the two bubbles). Compared to the 2D rising bubble problem, this setting shows no oscillation, partly due to the body force being calculated using volumetric buoyancy force. After reaching about 0.2 m/s, the rise velocity becomes steady. The corresponding Reynolds number is calculated to be:

$$Re = \frac{\rho_h U_t d}{\mu_h} = 43.2, \tag{3.65}$$

where U_t is the terminal velocity. The Reynolds number is in good agreement with the Reynolds number of 43 observed in the experimental setting (van Sint Annaland et al., 2005). After this steady state, the rise velocity increases as the two bubbles are about to coalesce. The difference between the unfiltered and filtered cumulant

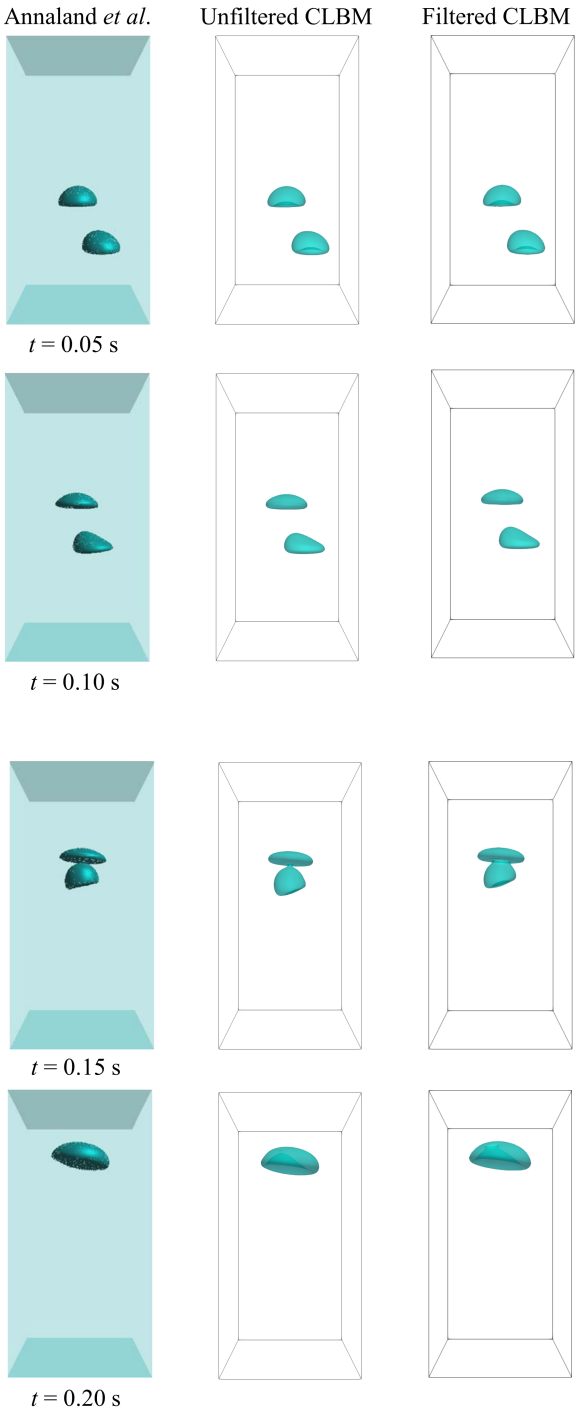

Figure 3-9: Evolution of bubble shapes in 3D oblique coalescence of two bubbles problem. van Sint Annaland et al. (2005) (left), unfiltered cumulant LBM (middle), and filtered cumulant LBM (right).

LBM is pronounced in this stage. Qualitative agreement with the experiment can be observed.

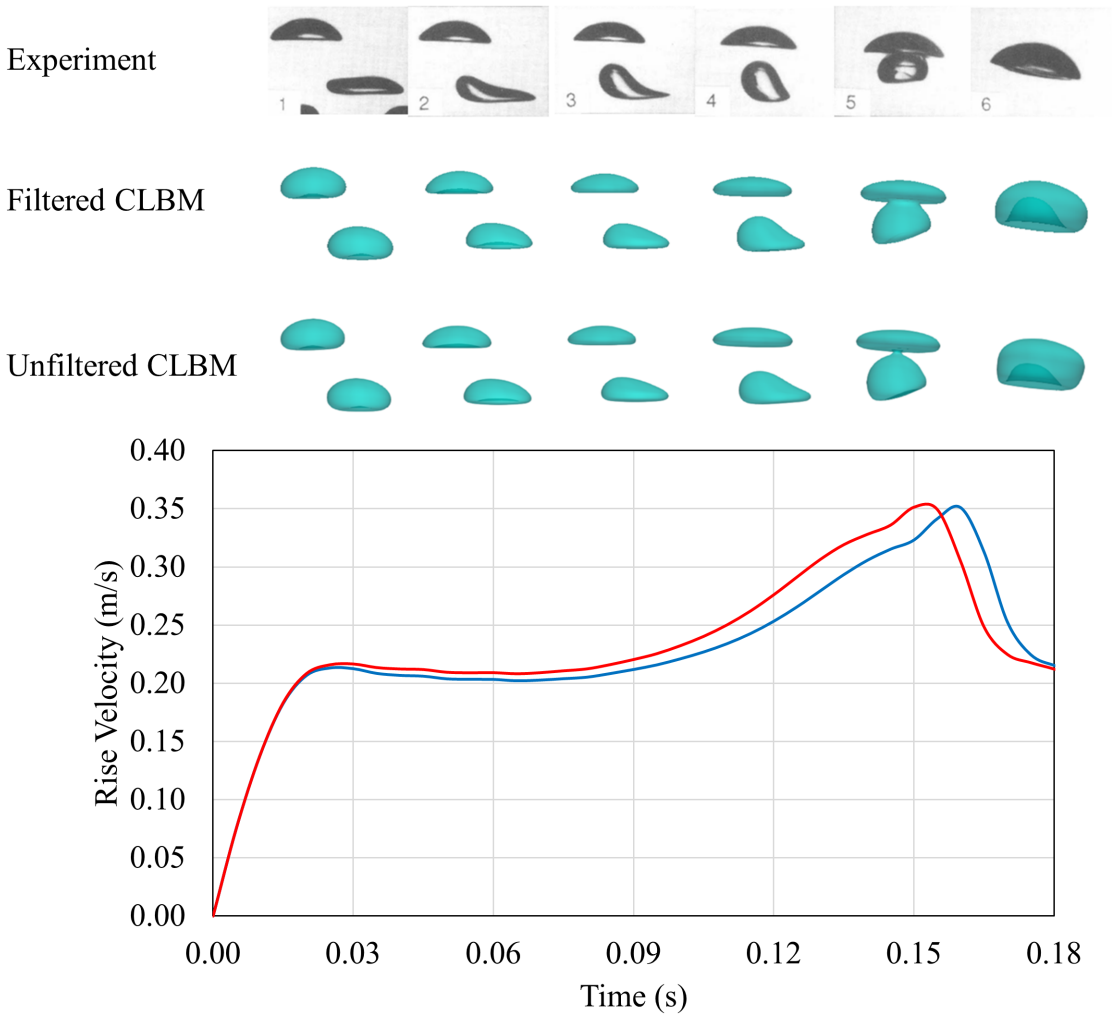

Figure 3-10: Evolution of rising velocities in 3D oblique coalescence of two bubbles problem. Unfiltered cumulant LBM (blue) and filtered cumulant LBM (red). Included are the experimental photos taken from Brereton and Korotney (Brereton and Korotney, 1991).

3.4.5 3D droplet splashing on a thin film

To test the proposed method in higher density ratio and Reynolds number settings, a 3D droplet splashing on a thin film problem is considered. The problem has been studied by many researchers both theoretically (Yarin, 2006) and numerically (Wang et al., 2015; Fakhari et al., 2016; Rieber and Frohn, 1999).

Fig. 3-11 shows the schematic of the problem. A spherical droplet with diameter $D = 5.537 \times 10^{-5}$ m and initial velocity $U_o = 32.25$ m/s is placed just above a thin

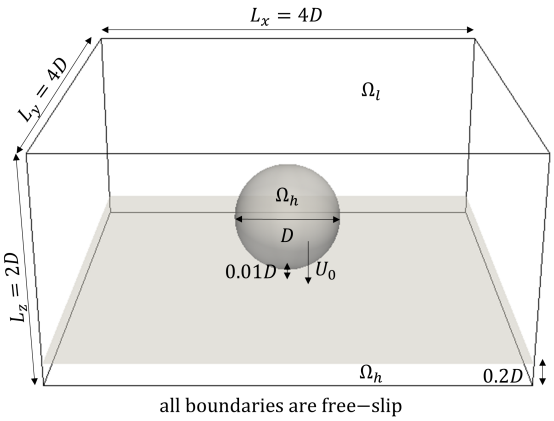

Figure 3-11: Schematic of initial condition of the 3D droplet splashing on a thin film.

film with height $h = 0.2D$ in a zero gravity environment. The density and viscosity of the heavier phase are $\rho_h = 1000$ kg/m^3 and $\mu_h = 8.928 \times 10^{-4}$ kg/(m $\cdot$ s), whereas the density and viscosity of the lighter phase are $\rho_l = 1$ kg/m^3 and $\mu_l = 8.928 \times 10^{-6}$ kg/(m $\cdot$ s). The surface tension is $\sigma = 0.072$ kg/s^2.

The Reynolds, Weber numbers (ratio between the inertial and surface tension force), and dimensionless time characterizing the problem are:

$$Re = \frac{\rho_h U_o D}{\mu_h} = 2000, \tag{3.66}$$

$$We = \frac{\rho_h U_o^2 D}{\sigma} = 800. \tag{3.67}$$

$$t^* = t\frac{U_o}{D} \tag{3.68}$$

To ease the computational burden, the problem was simulated on a quarter domain $L'_x \times L'_y \times L'_z = 2D \times 2D \times 2D$, with symmetry at $x = L_x/2$ and $y = L_y/2$, up to time $T^* = 2$. The problem was solved using both unfiltered and filtered cumulant LBM with $\omega_1 = 2$, the mesh resolution $\Delta x = D/200$, and the number of time steps $N_t = 40000$. The body force is calculated as $F_b = -\rho g$.

Complex dynamics occur in this problem. Soon after the initial impact, a thin sheet of liquid (lamella) is ejected and expands radially and vertically. While the lamella expands, a liquid ring (rim) develops on its top. The rim is subject to insta-

bility, which causes it to break into cusps, fingers, and secondary droplets, forming a crown shape. The evolution of the crown radius can be measured and used to determine the flow development's progress at any given time.

In this study, to trigger the rim's breakup, a uniform random disturbance with an amplitude of $0.05U_o$ is added to the droplet's initial velocities and the stationary film, similar to Rieber and Frohn (Rieber and Frohn, 1999). The surface tension effect quickly damps this disturbance.

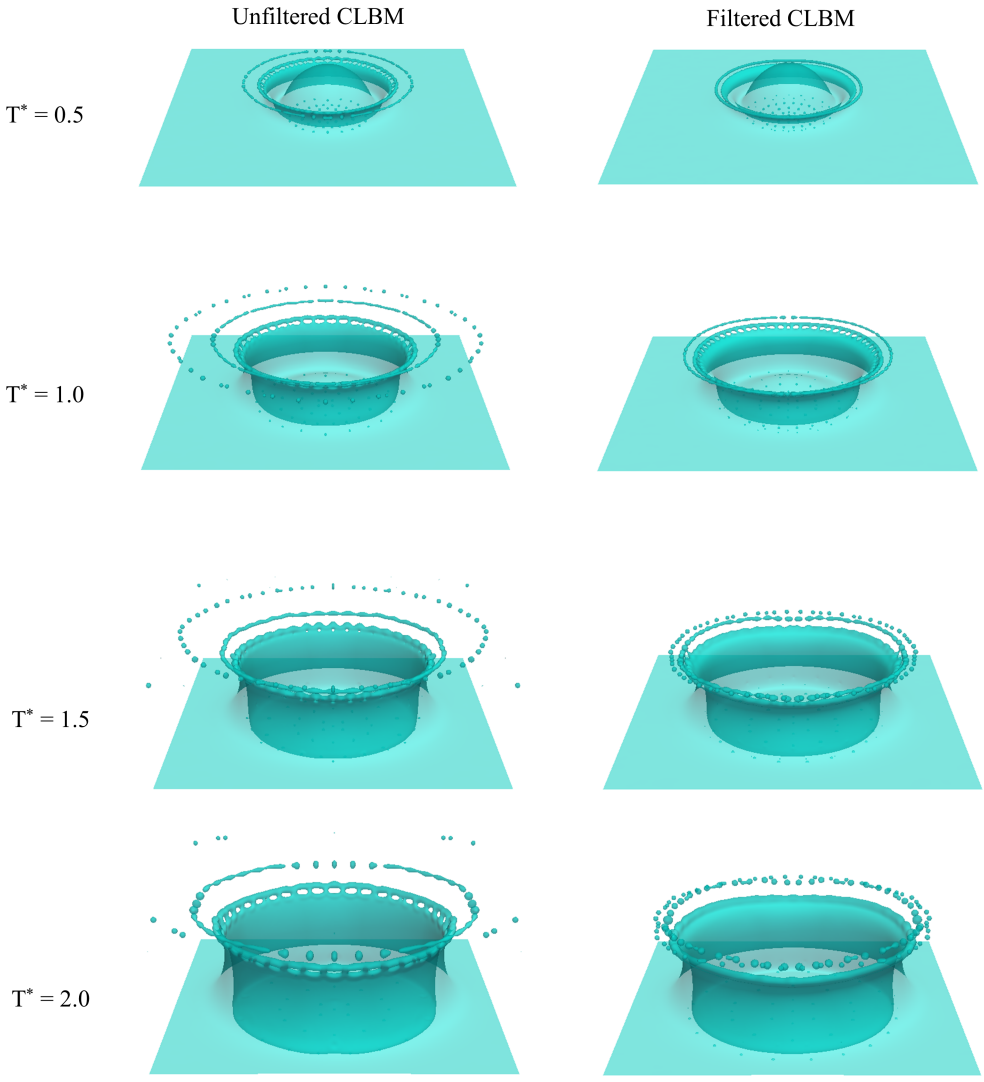

Figure 3-12: Interface evolution in 3D droplet splashing on a thin film at a resolution $\Delta x = D/200$. Unfiltered cumulant LBM (left) and filtered cumulant LBM (right).

Fig. 3-12 shows the interface evolution obtained from the simulation. Both the

unfiltered and filtered cumulant LBM can capture the radial growth of the lamella similarly. However, differences can be seen clearly for axial growth. Both the unfiltered and filtered cumulant LBM cannot quite capture the cusps and fingers but show the rim's breakup into secondary droplets. Each finger's tip is connected, as shown by the unfiltered cumulant LBM at $T^* = 2$, which may be due to the difficulty to represent a sharp interface using a diffuse interface model. Moreover, the filtered cumulant LBM shows more viscous results with less occurrence of secondary droplets.

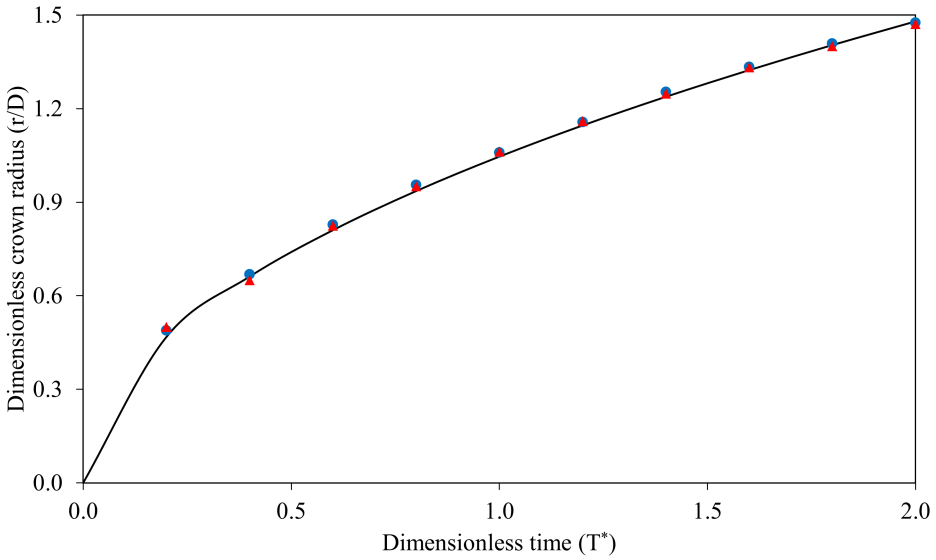

Figure 3-13: Evolution of the crown radius in 3D droplet splashing on a thin film problem. Reference (Rieber and Frohn, 1999) (black line), unfiltered cumulant LBM (blue circle), and filtered cumulant LBM (red triangle).

Fig. 3-13 compares the evolution of the crown radius obtained from the simulations and from the theoretical study by Yarin (Yarin, 2006) who shows that the radial growth of the splashing lamella can be described as:

$$r/D = \alpha_0 \sqrt{T^*}, \tag{3.69}$$

where

$$\alpha_0 = (6\frac{h}{D})^{\frac{1}{4}}, \tag{3.70}$$

according to Rieber and Forhn (Rieber and Frohn, 1999). The crown radius from the

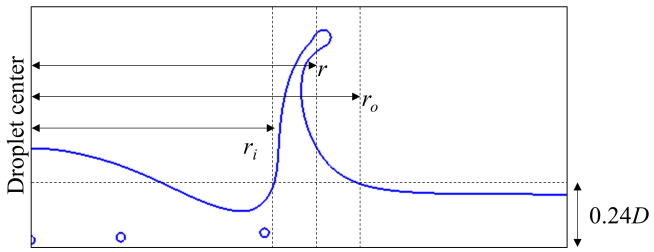

Figure 3-14: Determination of crown radius $r = (r_i + r_o)/2$ in 3D droplet splashing on a thin film problem.

simulation is obtained similarly with (Inamuro et al., 2016), where its value is equal to half of the outer and inner radius of the crown as shown in Fig. 3-14.

Both simulated results agree very well with the reference. As in (Wang et al., 2015), the crown radius evolution is insensitive to the Reynolds and Weber numbers. However, the rim's breakup depends strongly on them and can be observed at $Re = 2000$ and $We = 800$, which has been demonstrated by the proposed method.

3.4.6 3D dam-breaking on a dry floor

The quality of the proposed method in simulating a violent two-phase flow is examined by simulating the 3D dam-breaking on a dry floor problem. The problem is characterized by a high-density ratio, high Reynolds number, and rapid and complex topological changes. Simulation results are compared to the experimental results by Hu and Sueyoshi (Hu and Sueyoshi, 2010), Martin and Moyce (Martin et al., 1952), and numerical results by Janssen and Krafczyk (Janssen and Krafczyk, 2010) who simulated the problem by using free-surface LBM.

Fig. 3-15 shows the problem setup. An initial stationary water column with the width a and height n^2a is placed at the bottom-left corner of the domain, where n defines the initial water column's aspect ratio. Experimentally, this is achieved by using a partition plate. As the experiment initiates, the water column starts flowing inside the water tank due to the gravitational pull. The column height falls, and a surge develops along x-axis and crashes against the right-end domain.

The simulation is performed with the density of water and air set to $\rho_h = 1000$

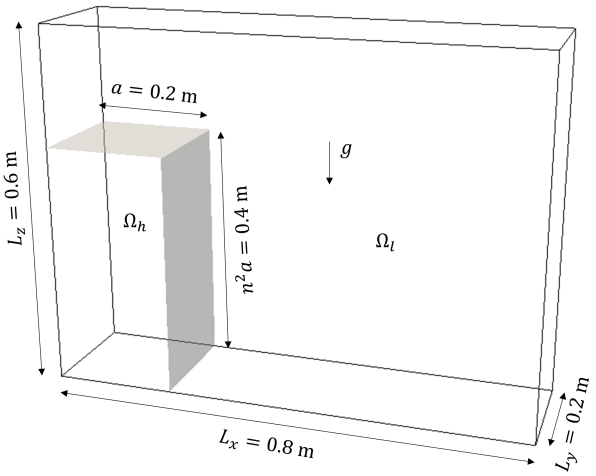

Figure 3-15: Schematic of initial condition of the 3D dam-breaking on a dry floor problem.

kg/m^3 and $\rho_l = 1$ kg/m^3, respectively. The dynamic viscosity of water and air are $\mu_h = 10^{-3}$ Pa $\cdot$ s and $\mu_l = 10^{-5}$ Pa $\cdot$ s, respectively. The gravity acceleration and surface tension are $g = 9.8$ m/s^2 and $\sigma = 0.072$ N/m, respectively. The reference velocity and Reynolds number are defined as:

$$u_0 = \sqrt{gn^2a} \approx 2.0 \text{ m/s}, \tag{3.71}$$

$$Re = \frac{\rho_h u_0 n^2 a}{\mu_h} \approx 7.9 \times 10^5. \tag{3.72}$$

The surge front position x along the x-axis (the furthest surge position from y-z plane) can be measured and used to determine the progress of the flow at any given time. The time and surge front are normalized as follows:

$$t^* = nt\sqrt{\frac{g}{a}}, \tag{3.73}$$

$$X = \frac{x}{a}. \tag{3.74}$$

The problem is simulated up to time $T = 1$ s with a time interval $\Delta t = 1/40000$ s. Two cases are simulated, one with free-slip boundaries and the other with no-slip boundaries. Both cases were simulated at a resolution of $400 \times 100 \times 300$. The body

force is calculated as $F_b = -\rho g$.

Fig. 3-16 shows the evolution of water profile at times $t = 0.18$ s, 0.39 s, 0.52 s, and 0.99 s. Fig. 3-16 (left) shows the experimental results by Hu and Sueyoshi (Hu and Sueyoshi, 2010), whereas Fig. 3-16 (middle) and (right) show the simulation results obtained by using filtered cumulant LBM with free-slip and no-slip boundaries, respectively.

For this problem, the computation with the unfiltered cumulant LBM was unstable. Therefore, only the results from the filtered cumulant LBM are shown here. Herein the results are obtained using $\omega_1 = 2$. We have tested using $\omega_1 = 1$, but it is also unstable without a velocity field filter.

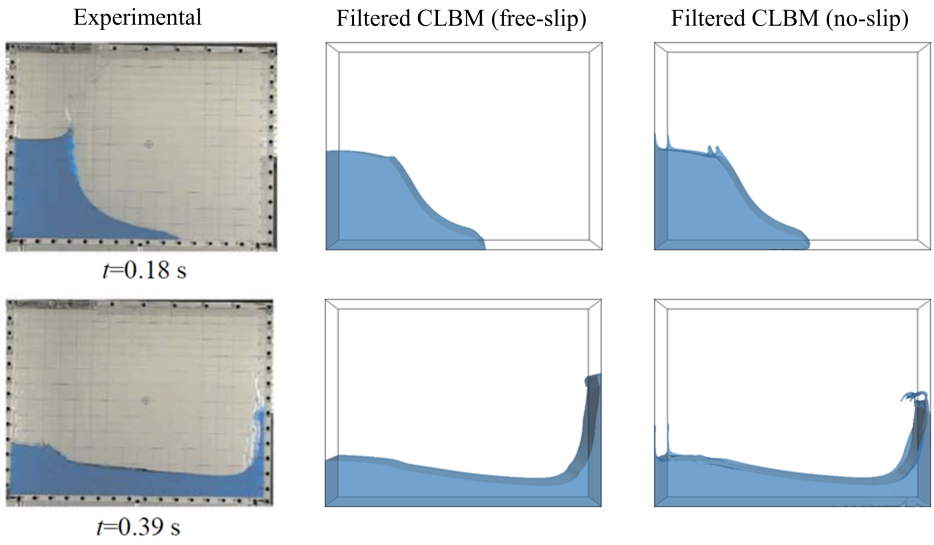

In the experiment, a partition plate was used to hold the water column and then removed at high speed. Its effect on the surge front speed has been studied by Hu and Sueyoshi and was concluded negligible if the partition plate is removed at sufficiently high speed (Hu and Sueyoshi, 2010). In the simulation, the water column is released at once and instantly. Comparing the evolution of the surge front, water height, splashing, and wave breaking (as seen in Fig. 3-16), it is shown that the results from the simulation are qualitatively in good agreement with the experiment, especially for no-slip boundaries. In this problem, a very thin boundary layer is expected to be developed due to the high Reynolds number, and therefore it is supposed to

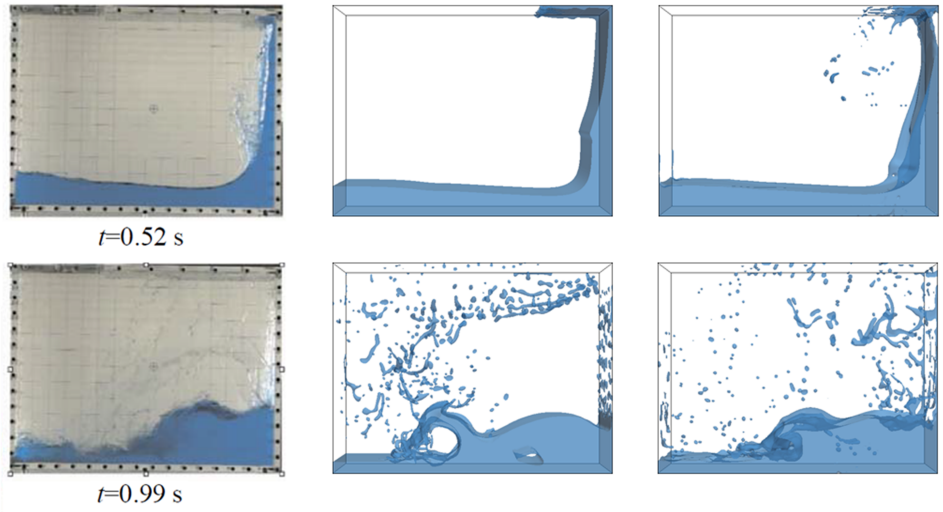

Figure 3-16: Evolution of water profile for 3D dam-breaking problem on a dry floor. Experimental by Hu and Sueyoshi (Hu and Sueyoshi, 2010) (left), filtered cumulant LBM – free-slip (middle), filtered cumulant LBM – no-slip (right).

be appropriate to use free-slip boundaries. However, a faster surge front than the experiments is obtained, which is also observed in (Janssen and Krafczyk, 2010; Hu and Sueyoshi, 2010). A numerical boundary layer is developed when using no-slip boundaries, which spans several grid points and slows down the surge front speed.

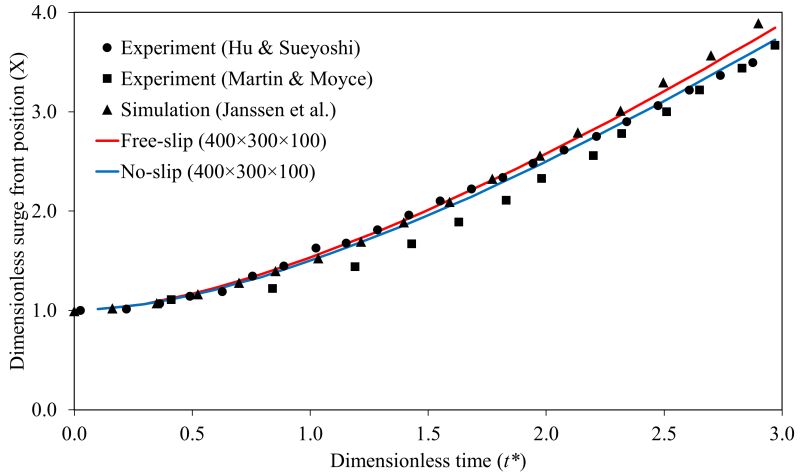

Figure 3-17: Evolution of dimensionless surge front position for 3D dam-breaking problem on a dry floor. Slip (red) and no-slip (blue) at resolution of $400 \times 300 \times 100$. References: experiment by Hu and Sueyoshi (Hu and Sueyoshi, 2010) (black circle), experiment by Martin and Moyce (Martin et al., 1952) (black square), and simulation by Janssen and Krafczyk (2010) (black triangle).

Fig. 3-17 shows the evolution of the surge front position along x-axis. As shown in the figure, there are some discrepancies between the references; however, the proposed method's results lie between the references. For free-slip boundaries, the proposed method results are in good agreements with Janssen and Krafczyk (2010). who also use free-slip boundaries. The results are in good agreement with the experimental results for no-slip boundaries, especially with Hu and Sueyoshi.

3.4.7 3D dam-breaking on a wet floor

In this section, a variant of the previous dam-breaking problem is considered where a thin liquid film is added on the simulation domain floor. The addition of a thin film causes additional complexity in terms of breaking and splashing. The proposed method is benchmarked against our in-house incompressible solver to examine its quality.

The incompressible solver solves the INSE using Simplified Marker and Cell (SMAC) method (Amsden and Harlow, 1970). The 5th order Hamilton-Jacobi Weighted Essentially Non-Oscillatory (HJ-WENO) scheme (Jiang and Peng, 2000) and the 3rd order Total Variation Diminishing (TVD) Runge-Kutta (Gottlieb and Shu, 1998) are used for the space discretization and the time integration, respectively. The pressure Poisson equation is solved using AMGCG method (Pereira et al., 2006). For the interface capturing method, the Tangent of Hyperbola for Interface Capturing (THINC)/WLIC scheme (Yokoi, 2007) is employed where the normal vector is calculated from a level set function (Osher and Sethian, 1988).

Fig. 3-18 shows the problem setup. An initial stationary water column with a width of 15 cm and a height of 36 cm is placed touching the ceiling at the left-end of the domain. The thin water layer's height is $h = 1.8$ cm, which corresponds to a depth ratio of 0.05. The physical parameters of this problem are the same as in the previous dam-breaking problem. The reference velocity and Reynolds number are defined as:

$$u_0 = \sqrt{g(L_z - h)} \approx 1.83 \text{ m/s}, \tag{3.75}$$

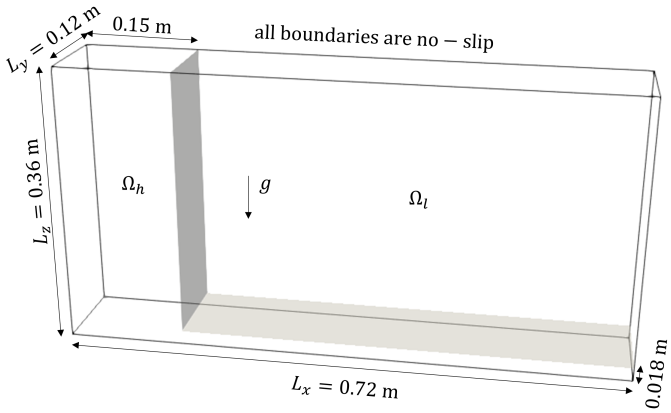

Figure 3-18: Schematic of initial condition of the 3D dam-breaking problem on a wet floor.

$$Re = \frac{\rho_h u_0 (L_z - h)}{\mu_h} \approx 6.3 \times 10^5. \tag{3.76}$$

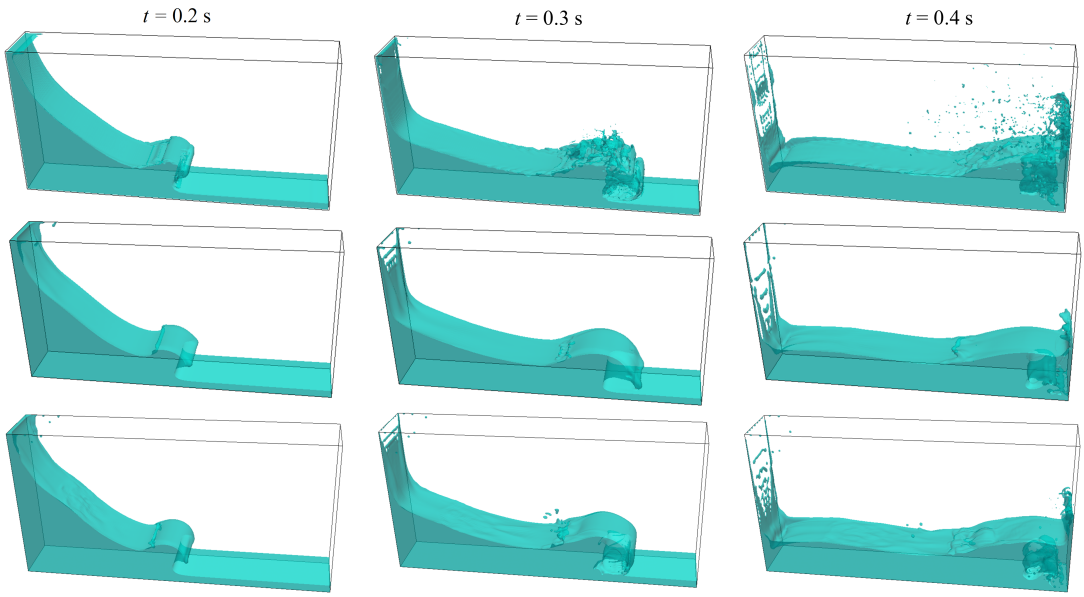

The problem was simulated using filtered cumulant LBM with $\omega_1 = 2$ up to time $T = 1$ s with a resolution of $N_x \times N_y \times N_z$ of $576 \times 96 \times 288$ and $1152 \times 192 \times 576$ with number of time step N_t of 80000 and 320000, respectively. The body force is calculated as $F_b = -\rho g$. The unfiltered cumulant LBM is unstable for this problem.

Fig. 3-19 shows the evolution of the water profile obtained by the reference ($576 \times 96 \times 288$) (top), filtered cumulant LBM ($576 \times 96 \times 288$) (middle), and filtered cumulant LBM ($1152 \times 192 \times 576$) (bottom). As soon as the flow is released, a wave is developed

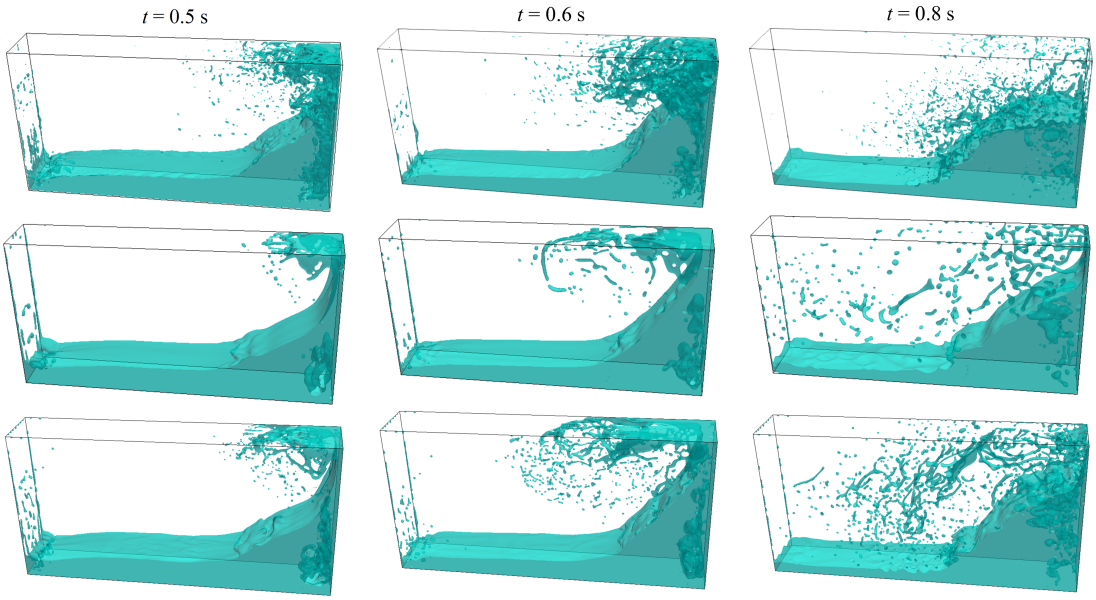

Figure 3-19: Evolution of water profiles in 3D dam-breaking on a wet floor. Reference ($576 \times 96 \times 288$) (top), filtered cumulant LBM ($576 \times 96 \times 288$) (middle), and filtered cumulant LBM ($1152 \times 192 \times 576$) (bottom).

at $t = 0.2$ s, interacts with the down-stream water (wave-breaking) at $t = 0.3$ s, entrains air at $t = 0.4$ s, and then crashes against the right-end of the domain at $t = 0.5$ s. At later stages ($t = 0.6$ s and $t = 0.8$ s), the entrained air develops into many bubbles that rise to the surface. The water splashing on the ceiling develops into many droplets that fall, break, and recombine. After it rises, the wave then returns with many small droplets raining on it, making the simulation using other two-phase LBMs unstable.

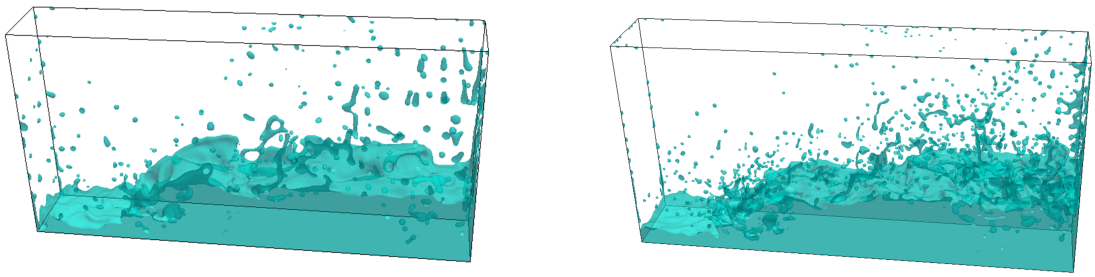

Figure 3-20: Evolution of water profiles in 3D dam-breaking on a wet floor at $t = 1.0$ s using filtered cumulant LBM. Resolution: $576 \times 96 \times 288$ (left) and $1152 \times 192 \times 576$ (right).

Fig. 3-20 shows the present result at $t = 1.0$ s, which shows that the proposed method remains stable for a long time. The proposed method results are qualitatively in good agreement with the reference, although they look more viscous due to the diffuse interface model and second-order filter. With the increase of resolution, however, less viscous results can be obtained.

3.4.8 3D liquid jet breakup

To further examine the quality of the proposed method, the liquid jet breakup problem is considered. This problem is still limitedly studied (at a low-density ratio or in 2D) (Saito et al., 2017; Amirshaghaghi et al., 2018). Even for incompressible Navier-Stokes solver, this problem is still challenging, especially for 3D simulation of a liquid jet breakup with high-density ratio, Reynolds number, and Weber number. This study is our first attempt to simulate the problem, and the potential of the proposed method is demonstrated herein. Shinjo and Umemura's work (Shinjo and Umemura, 2010) is used as a reference that solves the problem using an incompressible Navier-Stokes solver.

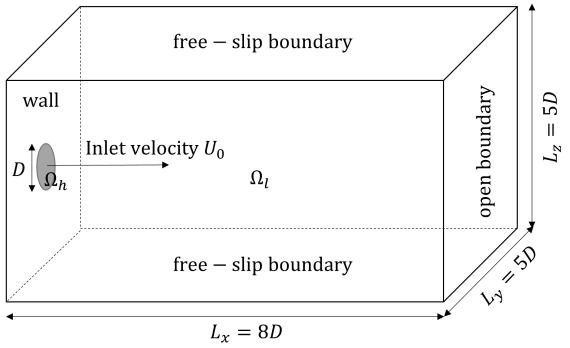

Figure 3-21: Schematic of initial condition of the liquid jet atomization problem.

Fig. 3-21 shows the schematic of the problem. A liquid jet with an initial diameter $D = 0.0001$ m flows into a chamber with a uniform velocity of U_0. The chamber's length is half of the original size in the reference (Shinjo and Umemura, 2010). The left boundary is a wall except for the circular inflow, the right boundary is an open boundary, and the other boundaries are free-slip boundaries.

Two cases were simulated with the physical parameters are shown in Table 3.2. The surface tension in both cases is equal to $\sigma = 0.03$ N/m. The physical values are based on fuel and air' properties. The air is compressed in Case 1, whereas normal air is used in Case 2. Case 1 appears in the reference, but Case 2 is our own setup.

Table 3.2: Physical parameters in 3D liquid jet breakup problem.

Case	ρ_h (kg/m^3)	ρ_l (kg/m^3)	μ_h $(Pa \cdot s)$	μ_l $(Pa \cdot s)$	U_0 (m/s)
1	848	34.5	2.87×10^{-3}	1.97×10^{-5}	100
2	848	1.205	2.87×10^{-3}	1.84×10^{-5}	200

The Reynolds number, Weber number, and the dimensionless time characterizing the problem are:

$$Re = \frac{\rho_h U_0 D}{\mu_h}, \tag{3.77}$$

$$We = \frac{\rho_h U_0^2 D}{\sigma}, \tag{3.78}$$

$$t^* = t\frac{U_0}{D}. \tag{3.79}$$

Based on the definition above, the Reynolds and Weber number of Case 1 are 2958 and 28200, respectively, whereas the Reynolds and Weber number of Case 2 are 5916 and 112800, respectively.

To ease the computational burden, the problem was simulated on a quarter domain $L'_x \times L'_y \times L'_z = 8D \times 2.5D \times 2.5D$, with symmetry at $y = L_y/2$ and $z = L_z/2$ up to time $T^* = 7.19$. The problem was solved using both unfiltered and filtered cumulant LBM with $\omega_1 = 1$. For Case 1, the problem is tested with mesh resolution $\Delta x = D/50$ and $\Delta x = D/100$ and the number of time steps $N_t = 7190$ and $N_t = 14380$, respectively. For Case 2, the problem is tested with mesh resolution $\Delta x = D/100$ and the number of time steps $N_t = 28760$.

Fig. 3-22 shows the overall flow structure of Case 1. Very detail structure was obtained in the reference (Fig. 3-22a) as the mesh resolution is high $\Delta x = D/286$. The result from the unfiltered cumulant LBM is shown (Fig. 3-22b). An important thing to notice is that the novel velocity-based formulation developed in this study (unfiltered cumulant LBM) can stably solve this case even without the turbulence

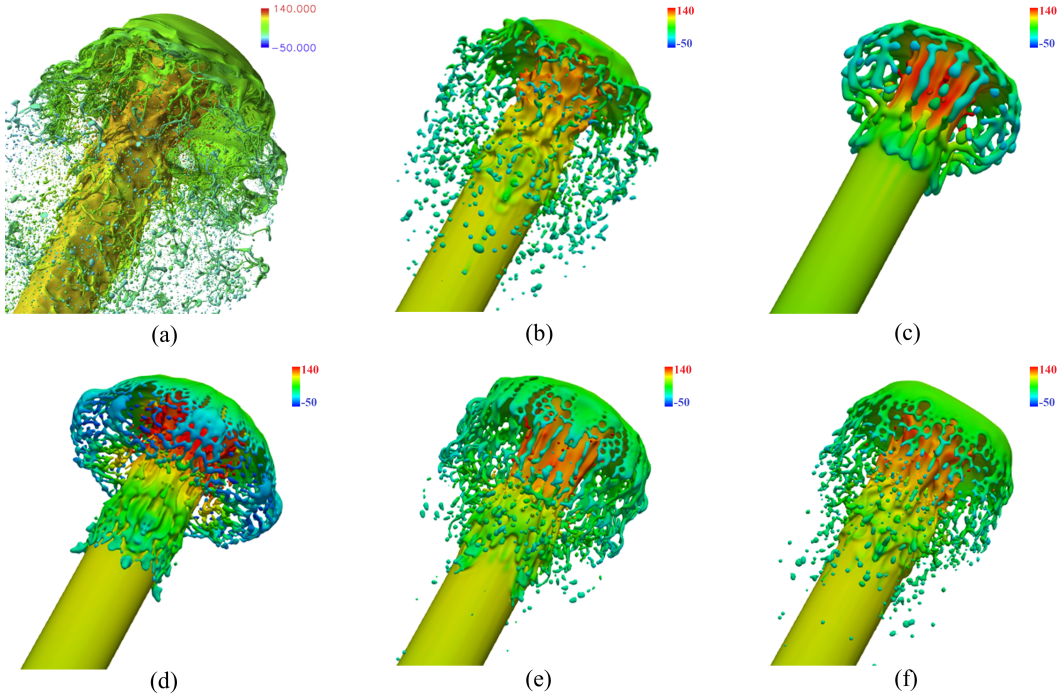

Figure 3-22: The overall flow structure at $T^* = 7.19$ in liquid jet breakup for Case 1. Reference ($\Delta x = D/286$) (a), unfiltered cumulant LBM ($\Delta x = D/100$) (b), filtered cumulant LBM ($\Delta x = D/50, Pe_{cutoff} = 2$) (c), filtered cumulant LBM ($\Delta x = D/100, Pe_{cutoff} = 2$) (d), filtered cumulant LBM ($\Delta x = D/100, Pe_{cutoff} = 20$) (e), and filtered cumulant LBM ($\Delta x = D/100, Pe_{cutoff} = 50$) (f).

model in comparison to (Amirshaghaghi et al., 2018).

Only in this problem, we modify the cutoff value of the Peclet number in the velocity field filter to see its effect in capturing small structures such as droplets. (Fig. 3-22 c and d) show the result of filtered cumulant LBM on mesh resolution of $\Delta x = D/50$ and $\Delta x = D/100$ for $Pe_{cutoff} = 2$, respectively. The velocity field filter damps the flow structures as less breakup occurs. However, with the increase of mesh resolution, more breakup occurs. (Fig. 3-22 e and f) show the result of filtered cumulant LBM on mesh resolution $\Delta x = D/100$ for $Pe_{cutoff} = 20$ and $Pe_{cutoff} = 50$, respectively. The flow structures become closer to that obtained by the unfiltered cumulant LBM by increasing the cutoff value.

Fig. 3-23 shows the interface shape and the axial velocities of Case 1. The proposed method can capture the mushroom-like jet and the disturbance behind the tip of the jet. However, there is a discrepancy with the reference on the penetration depth

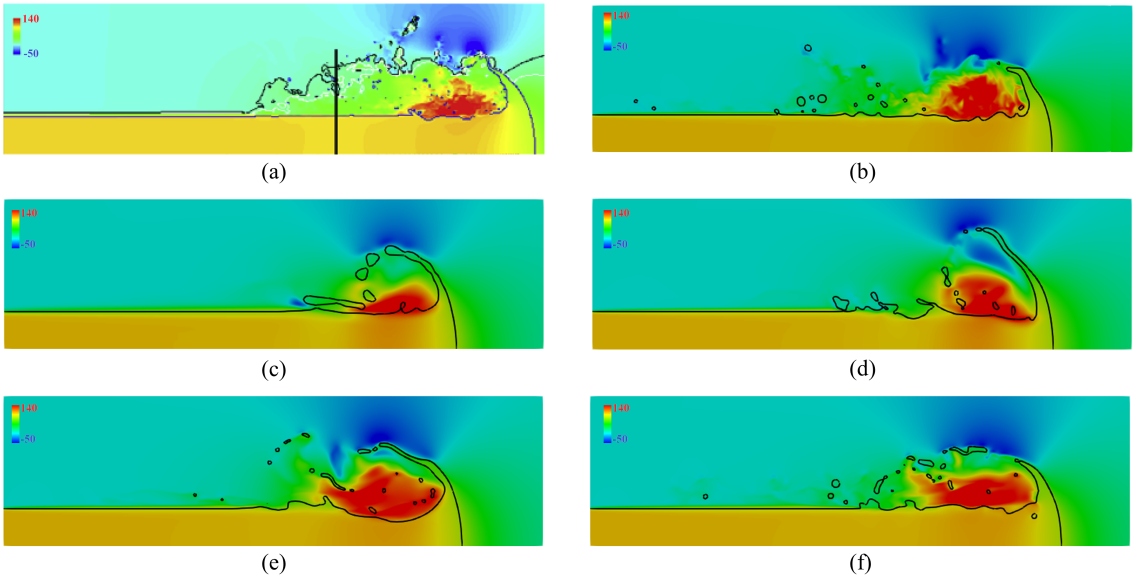

Figure 3-23: Interface shapes and axial velocities (upper half) at $y = 2.5D, T^* = 7.19$ in liquid jet breakup for Case 1. Reference ($\Delta x = D/286$) (a), unfiltered cumulant LBM ($\Delta x = D/100$) (b), filtered cumulant LBM ($\Delta x = D/50, Pe_{cutoff} = 2$) (c), filtered cumulant LBM ($\Delta x = D/100, Pe_{cutoff} = 2$) (d), filtered cumulant LBM ($\Delta x = D/100, Pe_{cutoff} = 20$) (e), and filtered cumulant LBM ($\Delta x = D/100, Pe_{cutoff} = 50$) (f).

about 12%, and therefore needs further studies.

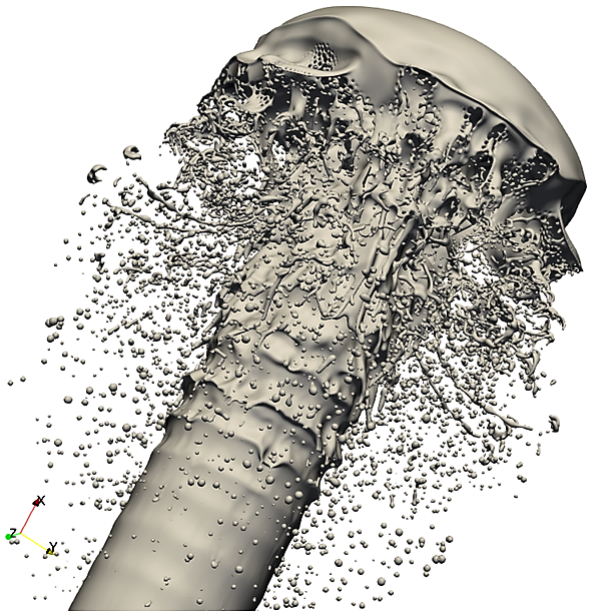

Figure 3-24: Interface shape of liquid jet breakup (Case 1, high resolution) at $T^* = 7.19$.

We have also simulated the Case 1 problem using a high resolution with $\Delta x = D/300$ using the unfiltered cumulant LBM. Fig. 3-24 shows the interface shape of the liquid jet breakup at $T^* = 7.19$. By using a higher resolution, jet instability, breakup, and splashing can be seen in more detail. The penetration depth by using this high resolution is slightly improved, which is $\approx 6.3H/D$ and about 10% difference with the reference (Shinjo and Umemura, 2010). It seems that the liquid jet simulated by the proposed cumulant LBM breaks up earlier than the reference, which affects the penetration depth.

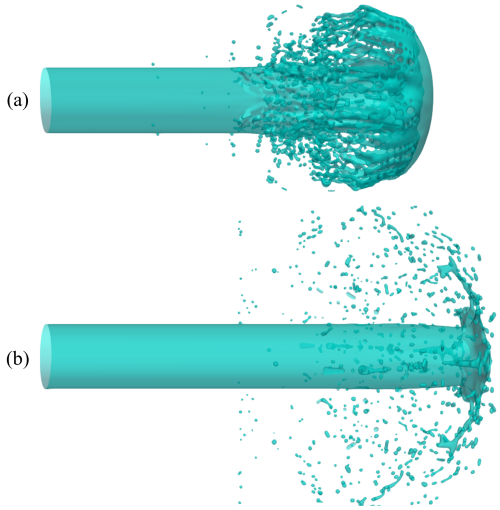

Figure 3-25: Interface shapes at $T^* = 7.19$ in liquid jet atomization obatined using filtered cumulant LBM with $\Delta x = D/100$ and $Pe_{cutoff} = 20$. Case 1 (a) and Case 2 (b).

Finally, we tested our proposed method for high-density ratio, Reynolds, and Weber number of Case 2. The result is obtained from filtered cumulant LBM with $Pe_{cutoff} = 20$ as shown in Fig. 3-25, whereas the unfiltered cumulant LBM is unstable for this case. As shown in Fig. 3-25, due to the high-density ratio, the jet in Case 2 is less affected by the air and penetrates deeper than the jet in Case 1. The tip of the jet becomes flat, and droplets come from it. This result shows the possibility of the proposed method in simulating this severe case; however, validation works remain for further studies.

3.5 Conclusions

This work presents a novel filtered cumulant LBM, which has been developed to solve violent two-phase flow problems, such as the dam-breaking setting. The proposed method employs the velocity-based formulation of the two-phase LBM, which has better stability than the momentum-based formulation, as the pressure update has less incompressibility error and the velocity update is done semi-implicitly. The cumulant collision model is also employed, which has good stability for problems with high Reynolds numbers. A second-order hybrid-like filter is also employed to further enhance the stability for the simulation of violent two-phase flows and can be turned off for non-violent flows. This filter adds artificial viscosity, which depends on the flow Peclet number similar to the advection equation's hybrid differencing scheme. The algorithm is completed by the conservative phase-field lattice Boltzmann method (CPFLBM), which is used for interface capturing and guarantees mass conservation.

The proposed method, along with its unfiltered version, has been validated on several non-violent two-phase flow problems such as the 2D rising bubble and the 3D droplet splashing on a thin film problem. The results show good agreements with both computational and experimental references. However, the proposed method is more diffusive due to the filter's application. Therefore, a high resolution is needed for sufficient accuracy, as seen in the 3D droplet splashing on a thin film problem. The proposed method has been applied to simulate the dam-breaking and liquid jet breakup, which shows its capacity to handle violent two-phase flows. The results show good agreements between the proposed method and the computational references. In dam-breaking problem, the maximum error of dimensionless surge front and water height between cumulant LBM with the experiment are about 6% and less than 1%, respectively. In the liquid jet breakup, the difference of penetration depth with the incompressible Navier-Stokes solver is about 10%. Most notably, in this study, we have stably simulated both the dam-breaking problem and liquid jet breakup at a high-density ratio and Reynolds number.

Chapter 4

Cumulant LBM for Turbulent Bubbly Pipe Flow Simulations

4.1 Introduction

Turbulent bubbly pipe flows are essential in many industrial applications, such as power plants and chemical plants. For better design and operation of such plants, understanding the dynamics of these flows is necessary. Despite its relatively simple configuration, turbulent bubbly pipe flow is useful for gaining insight into many critical phenomena, such as bubble distribution, velocity profile, and turbulence, that may affect the power or chemical plants (Kamp et al., 2001).

Many experiments on turbulent bubbly pipe flows have been conducted, and most of these experiments focused on vertical upward flow (Serizawa et al., 1975; Wang et al., 1987; Liu and Bankoff, 1993). Those experiments gave new insights such as the effect of bubble size, void fraction, and pressure gradient on bubble distribution, velocity profile, and turbulence. Fewer experiments on vertical downward flow have been conducted (Nakoryakov et al., 1996; Kashinsky and Randin, 1999), even though it is of great importance, especially concerning nuclear reactors' design safety analysis. Therefore, in the present study, we focus on applying our proposed method for simulating turbulent bubbly pipe flow to vertical downward flow.

Although experiments are essential for studying turbulent bubbly flows, they are

challenged by obstacles such as setting up experiments and obtaining accurate data. Direct Numerical Simulation (DNS) has therefore been employed in several studies to obtain the details of turbulent bubbly flows (Kawamura and Kodama, 2002; Lu and Tryggvason, 2006; Bois, 2017; Cifani et al., 2018). These simulations, however, were performed in a limited setting (namely, low-density ratio and Reynolds number) and simple channel geometry. The present study aims to simulate a more realistic setting of a water-air system, namely, high-density ratio and high Reynolds number, and in a pipe geometry commonly employed in experiments. This study will be useful in the future as flow conditions for industrial applications become even more severe.

DNS of turbulent bubbly flows requires a stable, accurate, and efficient method. In this study, the lattice Boltzmann method (LBM) is used because it promises massively parallel computation and dealing with complex boundaries. LBM is derived from a particular discretization of the Boltzmann equation and can solve the incompressible Navier-Stokes equations without solving the pressure Poisson equation (Sterling and Chen, 1996). LBM has been widely used for two-phase flow simulations, and it is continually being extended for more-complex problems (Shan and Chen, 1993; Fakhari et al., 2017b). Recently, we developed a cumulant LBM for two-phase flows with high-density ratio and high Reynolds number (Sitompul and Aoki, 2019). In this study, we extend the cumulant LBM for two-phase flows by incorporating a multi-phase field model so that it is possible to simulate separate bubble interfaces (Aihara et al., 2019).

In Section 4.2, the equations that govern the simulations of turbulent bubbly flow are given. In Section 4.3, the proposed method is described; that is, cumulant LBM for two-phase flow, and the multi-phase field model. In Section 4.4, the problem specifications, which include computational domain, flow characteristics, test cases, and post-processing, are given. In Section 4.5, the capability of the proposed method in simulating turbulent flows is demonstrated in terms of turbulent single-phase channel flows ($\mathrm{Re}_\tau = 180, 590$) and pipe flows ($\mathrm{Re}_\tau = 180, 550$), turbulent bubbly channel flows with ($\mathrm{Re}_\tau \approx 180$) and void fraction ($\alpha = 1.5\%, 19.4\%$), and turbulent bubbly pipe flow with ($\mathrm{Re}_\tau = 550, \alpha = 9.5\%$). In Section 4.6, the conclusions of this study

are presented.

4.2 Governing equations

Hereafter, a fully developed, turbulent, bubbly, downward pipe flow is considered. Experimentally, a long pipe with an inner diameter D and length $L \approx 80D$ was used (Colin et al., 2012). Water and small air bubbles were introduced into the pipe from an inlet at the top of the pipe and flowed downward. While traveling through the pipe, the air bubbles coalesced and thereby affected the turbulent flow. Parameters of interest were measured at a distance $L = 70D$ from the inlet, where the turbulence is fully developed with a specific bubble size.

To execute DNS of a problem in full size is not presently practical; therefore, DNS's common practice for turbulent bubbly flows is followed hereafter. Instead of a long pipe with inlet and outlet boundaries and coalescing bubbles, a short pipe with periodic boundaries and non-coalescing bubbles of fixed size is used. It is expected that the fully developed condition of a small-size problem is similar to that of a full-size one. The governing equations for fluid motion are given in detail as follows.

An immiscible, incompressible, viscous, two-phase flow of dispersed bubbles (a lighter fluid) surrounded by water (a heavier fluid) is considered. Its hydrodynamics is governed by the following Incompressible Navier-Stokes Equations (INSE), given as

$$\nabla \cdot \mathbf{u} = 0, \tag{4.1}$$

$$\frac{\partial \mathbf{u}}{\partial t} + \mathbf{u} \cdot \nabla \mathbf{u} = -\frac{1}{\rho}\nabla p + \frac{1}{\rho}\nabla \cdot \left[\mu \left(\nabla \mathbf{u} + \nabla^T \mathbf{u}\right)\right] + \frac{1}{\rho}\mathbf{F}_b + \frac{1}{\rho}\mathbf{F}_s, \tag{4.2}$$

where ρ is fluid density, $\mathbf{u}$ is fluid velocity, p is fluid pressure, μ is fluid dynamic viscosity, $\mathbf{F}_b$ is body force, $\mathbf{F}_s$ is surface tension force, and t is time.

A one-fluid approach, by which the two fluids (dispersed bubbles and water) are modeled as a single fluid having density and viscosity changes across the interface

between the two fluids, is taken as follows:

$$\rho = \phi\rho_l + (1-\phi)\rho_h, \tag{4.3}$$

$$\mu = \phi\mu_l + (1-\phi)\mu_h, \tag{4.4}$$

where subscripts l and h denote a lighter fluid and a heavier fluid, repectively, and ϕ is a common marker function distinguishing the two fluids ($\phi = 1$ and $\phi = 0$ indicate the lighter fluid and the heavier fluid, respectively).

A phase-field model is used to simulate the interface between the two fluids (Aihara et al., 2019). This model has gained popularity recently due to its ease of programming and excellent parallel scalability. However, when this model is used, two bubbles will automatically coalesce when their interfaces get close enough. The same situation, known as "numerical coalescence," also occurs in the cases of the volume-of-fluid or level-set methods. A multiple-marker approach is adopted to prevent this situation (Balcázar et al., 2015; Cifani et al., 2018). As for this approach, each bubble is modeled by using a distinct marker function. Multiple interfaces can therefore be modeled even when they lie within one grid-point. The phase-field model used in this study is described in detail in Subsection 4.3.1.

The common marker function in Eqs. (4.3) and (4.4) is composed of multiple marker functions that represent dispersed bubbles and is given as

$$\phi = \sum_i \phi_i, \tag{4.5}$$

where subscript i represents each component of the dispersed bubbles ($\phi_i = 1$ wherever bubble i is located and $\phi_i = 0$ elsewhere).

The body force is defined as

$$\mathbf{F}_b = \mathbf{G} + (\rho - \overline{\rho})\mathbf{g}, \tag{4.6}$$

where $\mathbf{G}$, $\overline{\rho}$, and $\mathbf{g}$ are applied pressure gradient force, average density, and gravita-

tional acceleration, respectively.

Surface tension is modeled by using an extended version of the continuous-surface-force model for dispersed bubbles (Balcázar et al., 2015):

$$\mathbf{F_s} = \sigma \sum_i \kappa_i \nabla \phi_i, \tag{4.7}$$

where σ is surface tension, and κ is curvature defined as

$$\kappa_i = -\nabla \cdot \mathbf{n}_i, \tag{4.8}$$

and normal vector $\mathbf{n}$ is calculated as

$$\mathbf{n}_i = \frac{\nabla \phi_i}{|\nabla \phi_i|}. \tag{4.9}$$

By using this multiple-marker approach and surface-tension model, it is possible to avoid coalescence of dispersed bubbles. This DNS model also has the advantage over experiments in that size distribution of the bubbles can be easily controlled.

4.3 Numerical methods

4.3.1 Cumulant LBM with Multi-phase Field Model

In this study, we employed the unfiltered version of cumulant LBM for hydrodynamics of the two phase flows described in Chapter 3. The additional viscosity term is modified and directly calculated from the Particle Distribution Function (PDF) as follows:

$$\mathbf{F}_{\nu,i} = \frac{\nu}{\nu + 1/6} \left[\sum_\alpha e_{\alpha i} e_{\alpha j} (f_\alpha - f_\alpha^{eq}) \right] \frac{\delta \rho}{\delta x_j}, \tag{4.10}$$

where subscripts i and j are spatial indexes, and f_α^{eq} is the equilibrium PDFs.

To capture the interfaces of the multiple phases, a multi-phase field model proposed by Aihara et al. (2019) is employed. The dynamics of the multiple phases are

governed by:

$$\begin{aligned}\frac{\partial \phi_i}{\partial t} + \nabla \cdot (\phi_i \mathbf{u}) =& M \left[\nabla \cdot \left\{ \nabla \phi_i - \frac{4}{W} \phi_i (1 - \phi_i) \mathbf{n}_i \right\} \right. \\ & \left. - \frac{\phi_i^2}{\sum_{j=1}^{N} \phi_j^2} \sum_{j=1}^{N} \left[\nabla \cdot \left\{ \nabla \phi_i - \frac{4}{W} \phi_i (1 - \phi_i) \mathbf{n}_i \right\} \right] \right],\end{aligned} \tag{4.11}$$

where ϕ is the phase-field variable, $\mathbf{u}$ is the velocity, M is the mobility, W is the interface half-width, $\mathbf{n}$ is the normal vector as defined in Eq. (4.9), t is the time, the subscript i and j are the indexes of different phases, and N is the total number of phases. This equation describes the motion of the multiple phases due to the advection (the second term at the left-hand side), the deviation from the equilibrium profile (the first term at the right-hand side), and the interaction between the multiple phases (the second term at the right-hand side). The multi-phase field model conserves mass, has relatively good accuracy, and does not require complex geometrical reconstruction. The interaction term (the second term at the right-hand side) ensures there is no overlapping between interfaces. The additional computational cost of the interaction term is small as it consists of values that have been precalculated from the diffusion - anti-diffusion term (the first term at the right-hand side).

At the equilibrium, each phase-field variable assumes a hyperbolic tangent profile:

$$\phi_i = \frac{1}{2} \left[1 + \tanh \left(\frac{2 s_i}{W} \right) \right], \tag{4.12}$$

where s is the signed distance function of the interface located at $s = 0$. This profile is also used as the initial profile. The multi-phase field equation (Eq. (4.11)) is then solved using finite volume method (FVM), where the advection flux is approximated using a third-order weighted essentially non-oscillatory (WENO) scheme (Liu et al., 1994), the diffusion flux is approximated using a linear function, and the time integration is approximated using a third-order total variation diminishing (TVD) Runge-Kutta (RK) scheme (Gottlieb and Shu, 1998). By using these schemes, the overshooting and undershooting of the phase-field values can be suppressed. However, small oscillations can still occur, especially for high-density ratio problems. There-

fore, to prevent the oscillations, we capture the interfaces of both dispersed lighter and continuous heavier fluids, cut-off the phase-field value smaller than zero and larger than one, and normalized the phase-field values each time step as:

$$\phi_i^{*,n+1} = \frac{\phi_i^{n+1}}{\sum_{j=1}^{N} \phi_j^{n+1}}. \tag{4.13}$$

Using the normalization, the summation of the phase-field variables is equal to one in one cell. The mass redistribution scheme is employed to conserve the mass for each phase-field variable exactly, where the mass difference with the initial value is distributed over the interface (Chiu and Lin, 2011).

The fluid density and viscosity are then computed from the dispersed phase only as in Eq. (4.5).

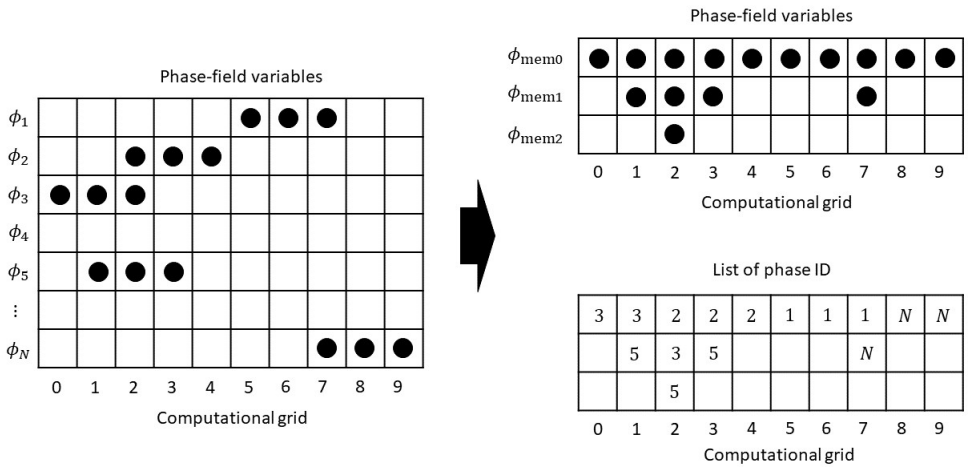

Figure 4-1: The schematic of the original active parameter tracking (APT) method.

The naive implementation of the multi-phase field model, in which values of N phase-field variables are saved, and N multi-phase field equations are solved for the whole domain, requires a huge amount of memory and calculations, especially when the number of phases is large. Therefore, the active parameter tracking (APT) method can be used to reduce the computational cost (Yamanaka et al., 2012). The schematic of the original APT method is shown in Fig. 4-1. In this method, only the active phase-filed variables, which values greater than a small cut-off value ($\phi_i > \epsilon$), are saved. A lookup table, which is a function of grid position, is then used to track

the active parameters. When the updated value of the phase-field variable is greater than the cut-off value, its value and phase identification (ID) number are saved as long as ϕ_{mem} is not full, as shown on the right-hand side of Fig. 4-1. If ϕ_{mem} is full, the updated value must be compared first with the minimum value saved in ϕ_{mem}. If it is greater than the minimum value, the updated value replaces the minimum value or discarded. Each time step, the lookup table is used to withdraw the phase-field value, and the calculations are performed only on the active grid-points containing the active phase-field variables and their neighboring inactive grid-points. By using this APT method, the required size of memory and calculations are significantly reduced.

We improved the computational efficiency of the previous APT method. The schematic of the improved active parameter tracking (APT) method is shown in Fig. 4-2. In the original APT, a new phase-field value is stored without considering its immediate neighbors. One needs to withdraw the phase-field value first before updating it because its immediate neighbor might have a different identity number. In the improved APT, a new phase-field value is stored with considering its immediate

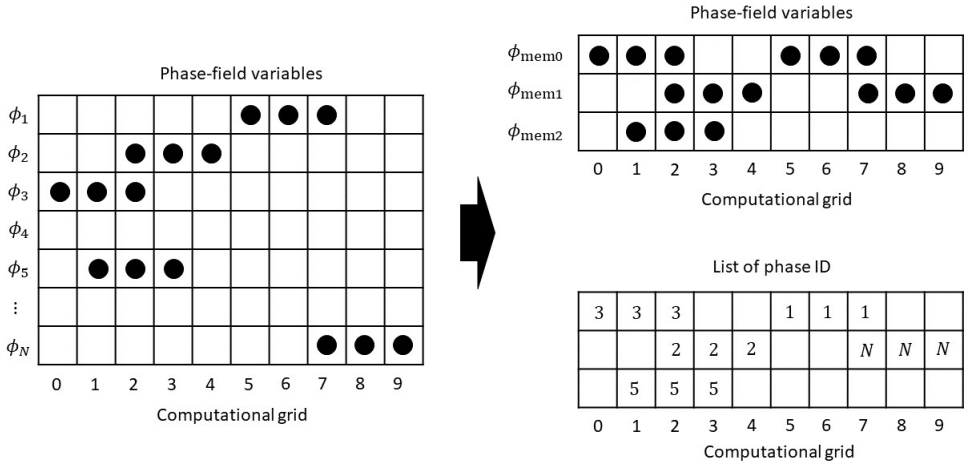

Figure 4-2: The schematic of the improved active parameter tracking (APT) method.

neighbors. The phase-field variables with the same identification number are grouped and saved in different spatial memory constraints that the immediate neighbors must be empty or of the same identification number. By using the improved APT method, one can update the phase-field variables in memory simultaneously and without first withdrawing the phase-field values, thus increasing the computational efficiency. In

this study, we set $\epsilon = 10^{-6}$ and prepare thirteen arrays of ϕ_{mem} to save the active phase-filed variables. However, during the simulation, only about six to seven arrays are used.

4.3.2 Boundary conditions

Two boundary conditions are employed in this study: namely, the wall and periodic boundary conditions. For the cumulant LBM, the interpolated bounce back scheme is employed as the wall boundary condition of abritary shape (Bouzidi et al., 2001). The unknown PDFs coming from the wall direction is approximated as:

$$f_{\bar{i}\bar{j}\bar{k}xyz(t+\delta t)} \begin{cases} 2q f^*_{ijkxyzt} + (1-2q) f^*_{ijk(x-ic\delta x)(y-ic\delta y)(z-ic\delta z)t}, & \text{if } q < \frac{1}{2}, \\ \dfrac{1}{2q} f^*_{ijkxyzt} + \dfrac{2q-1}{2q} f^*_{\bar{i}\bar{j}\bar{k}xyzt}, & \text{if } q \geq \frac{1}{2}, \end{cases} \tag{4.14}$$

where the same indexes as in Eq. (3.7) is used, and q is the distance to the wall normalized to the distance to the neighboring gridpoint. In addition, the normal gradients of pressure at the boundary is set to zero. For the multi-phase field model, a simple staircase shape is employed to model the abritary shape of the wall boundary. The phase-field variables and velocities at the wall are then set to zero. The periodic boundary condition is realized by simply copying the the DFs, pressure, velocities, and phase-field variables at one end to the corresponding halo region of the other end, and vise versa. In the present study, a halo region of two gridpoints is prepared as the a third-order WENO scheme is used in the multi-phase field model.

4.3.3 Algorithm of computation

The algorithm used for present DNS is summarized as follows:

Step 1: Initialize the macroscopic variables: phase-field variable $\phi(\mathbf{x}, 0)$ (Eq. (4.12)), fluid density $\rho(\mathbf{x}, 0)$ (Eq. (4.3)), fluid viscosity $\mu(\mathbf{x}, 0)$ (Eq. (4.4)), pressure $p(\mathbf{x}, 0)$, and macroscopic fluid velocity $\mathbf{u}(\mathbf{x}, 0)$.

Step 2: Update the multiple phase-field variables of Eq. (4.11) (using the third-order TVD-RK) and normalize them using Eq. (4.13). The normalized variables are saved by using APT.

Step 3: Update density $\rho(\mathbf{x}, t+\delta t)$ (Eq. (4.3)) and viscosity $\mu(\mathbf{x}, t+\delta t)$ (Eq. (4.4)).

Step 4: Compute the forces at current time step $\mathbf{F}(\mathbf{x}, t)$, which include surface tension given by Eq. (4.7).

Step 5: Compute post-collision distribution function $f^*(\mathbf{x}, t)$ (Eqs. (A.1) – (A.46)).

Step 6: Update distribution function (boundary conditions and streaming steps) $f(\mathbf{x}, t+\delta t)$ (Eq. (3.14)).

Step 7: Update pressure $p(\mathbf{x}, t+\delta t)$ (Eq. (3.30)).

Step 8: Filter the pressure field (Eq. (3.34)).

Step 9: Update the pressure force given by Eq. (3.36).

Step 10: Update velocity $\mathbf{u}(\mathbf{x}, t+\delta t)$ (Eq. (3.37)).

Step 11: Advance one-time step and return to **Step** 2.

4.4 Flow Characteristics

4.4.1 Computational domain

The present study is our first attempt to simulate a turbulent bubbly pipe flow with a high-density ratio, viscosity ratio, void fraction, and Reynolds number. The problem has not been simulated before and may possess some numerical challenges as far as we know. Therefore, during the proposed method development, we focus more on having stable computations with reasonable good accuracy rather than obtaining very accurate results. With this focus in mind, the concept of "minimum turbulent channel," proposed by Jiménez and Moin (1991), is adopted. In this concept, a

reduced domain size where its turbulence characteristics resemble that of the full one is employed. For a channel with half-width H, the full domain size of $L_x \times L_y \times Lz = 4\pi H \times 2H \times 4\pi H/3$ is reduced to $\pi H \times 2H \times \pi H/2$ in the streamwise, wall-normal, and spanwise directions, respectively (Vreman and Kuerten, 2014a). For a pipe with radius $R = H$, the streamwise length is reduced from $25R$ to $4\pi R$ (El Khoury et al., 2013). The computational time in the development of the proposed method is significantly reduced using the reduced domain size.

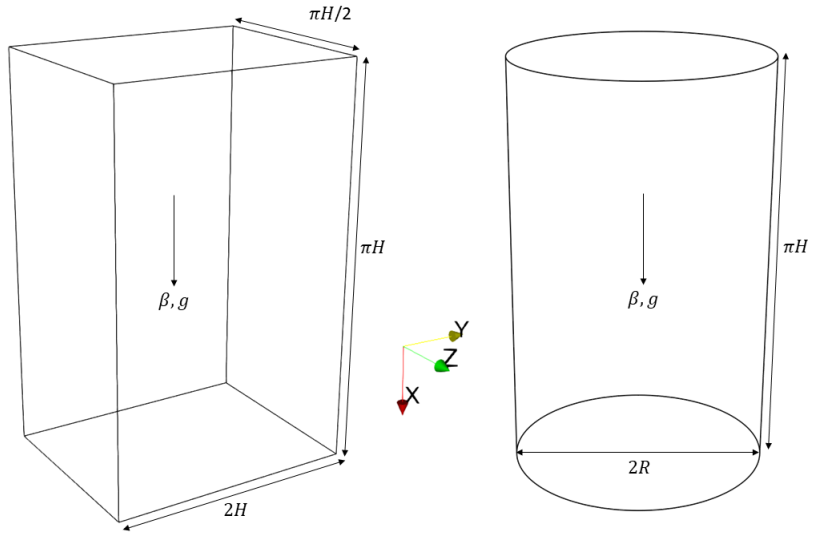

Figure 4-3: Schematic of the computational domain used in the present turbulent channel and pipe flow simulations.

The schematic of the computational domain used in this study is shown in Fig. 4-3. For the channel, periodic boundaries are applied in the streamwise (X) and spanwise (Z) directions and no-slip boundaries are imposed in the wall-normal (Y) directions. For pipe, periodic boundaries are applied in the streamwise (X) directions, and no-slip boundaries are imposed at the circumference. As LBM is employed, the computational domain is divided into uniform cubic lattices (uniform Cartesian grid), and therefore, in the case of a pipe, several grid-points outside the computational domain are inactive. A more sophisticated grid such as an adaptive grid is possible in LBM, however, beyond the present study's scope.

4.4.2 Flow characteristics

The turbulent bubbly flow is driven downward by a constant pressure gradient β in positive X-direction, which is the summation of the applied pressure gradient G and the weight of the mixture:

$$\beta = G + \bar{\rho} g, \tag{4.15}$$

where $\bar{\rho}$ and g are the average mixture density and the gravity acceleration (pointing downward), respectively. The mixture weight is not considered for the turbulent single-phase flow, and the flow is driven by the applied pressure gradient only.

The force balance at steady-state for a bubbly flow is given by:

$$\frac{\partial}{\partial y}\tau(y) + G + \rho(y) g = 0, \tag{4.16}$$

where τ, ρ, and y denote the shear stress, the local density, and the spanwise position, respectively. Given the local density:

$$\rho = \alpha \rho_l + (1 - \alpha)\rho_h, \tag{4.17}$$

Eq. (4.16) can be rewritten as:

$$\frac{\partial}{\partial y}\tau(y) + \beta + (\bar{\alpha} - \alpha(y))\,\Delta\rho g = 0, \tag{4.18}$$

where α and $\bar{\alpha}$ are the local and average void fraction, and the subscripts l and h denote the lighter and heavier fluids, respectively. The bubble distribution can then be determined as:

$$\alpha(y) = \bar{\alpha} + \frac{\beta + \frac{\partial}{\partial y}\tau(y)}{\Delta\rho g}. \tag{4.19}$$

The turbulent flow can be characterized by the friction Reynolds number:

$$\mathrm{Re}_\tau = \frac{u_\tau H}{\nu_h}, \tag{4.20}$$

where ν_h is the kinematic viscosity of the heavier fluid and u_τ is the friction velocity

which is related to the wall shear stress τ_w by:

$$u_\tau = \sqrt{\frac{\tau_w}{\rho_h}}. \tag{4.21}$$

The wall shear stress is related to the constant pressure gradient as:

$$\tau_w = (G + \bar{\rho}g)H = \beta H. \tag{4.22}$$

In the present study, we set β, H, and ρ_h to unity.

For the turbulent bubbly flow, the flow is also characterized by several dimensionless parameter: the density ratio, viscosity ratio, Eotvos number (the ratio of gravitational to surface tension forces), and the Morton number, which are respectively defined as:

$$\gamma = \frac{\rho_h}{\rho_l}, \tag{4.23}$$

$$\eta = \frac{\mu_h}{\mu_l}, \tag{4.24}$$

$$\mathrm{Eo} = \frac{\rho_h g D_b^2}{\sigma}, \tag{4.25}$$

$$\mathrm{Mo} = \frac{g\mu_h^4}{\rho_h \sigma^3}, \tag{4.26}$$

where μ, D_0, and σ are the dynamic viscosity, the initial diameter of the spherical bubble, and the surface tension, respectively.

4.4.3 Test cases

The capability of the proposed method in simulating turbulent flows is tested using several problems with increasing difficulty. First, the turbulent single-phase flows are simulated for both channel and pipe geometries at low Reynolds number ($\mathrm{Re}_\tau = 180$), and high Reynolds number ($\mathrm{Re}_\tau = 590$ for channel and $\mathrm{Re}_\tau = 550$ for pipe). The problems have been extensively studied numerically and experimentally, and as a result, reliable databases exist for validation (Kim et al., 1987; Eggels et al., 1994; El Khoury et al., 2013; Vreman and Kuerten, 2014a,b).

Table 4.1: Comparison of the details of the turbulent bubbly flow simulations between the present study and the references.

Author	Lu *et al.* (2006)	Bois G. (2017)	Cifani *et al.* (2018)	Present (high Re)	Colin *et al.* (2012)
Methods	FVM - FT	FDM - FT	FVM - VOF	LBM - PF	Experiment
Inclination	downward	upward	downward	downward	downward
Geometry	channel	channel	channel	pipe	pipe
Re_τ	127.3	180.0	154.5	550.0	880.0
γ	10.0	5.8	10.0	831.7	831.7
η	1.0	3.0	1.0	55.6	55.6
Eo	0.31	1.03	3.13	1.21	2.15
Mo	1.54×10^{-10}	3.53×10^{-12}	1.54×10^{-7}	2.55×10^{-11}	2.55×10^{-11}
α	1.5-6%	10.0%	19.4%	9.5%	9.5%
n_b	18-72	942	10000	225	N/A
$L_x(H)$	π	2π	8π	π	160
$L_y(H)$	2	2	2	2	2
$L_z(H)$	$\pi/2$	π	$4/3\pi$	2	2
$D_b(H)$	0.25	0.20	0.25	0.20	0.10
$\Delta_x(H/\mathrm{Re}_\tau)$	2.08	2.94	2.52	2.15	N/A
$\Delta_y(H/\mathrm{Re}_\tau)$	0.79/2.19	0.31	1.93	2.15	N/A
$\Delta_z(H/\mathrm{Re}_\tau)$	2.08	2.94	1.26	2.15	N/A
$D_b(H/\mathrm{Re}_\tau)$	32	36	39	110	88
N_x	192	384	1536	808	N/A
N_y	160	1152	160	512	N/A
N_z	96	192	512	512	N/A
D_b/Δ	14–40	12-115	20	51	N/A
N_{total}	2.9×10^6	8.5×10^7	1.3×10^8	2.1×10^8	N/A

Next, the turbulent bubbly channel flows with low-density ratio and Reynolds number ($\gamma = 10$ and $\mathrm{Re}_\tau \approx 180$, respectively) are simulated, and the results are compared with the existing numerical references (Lu and Tryggvason, 2008; Cifani et al., 2018). In this case, only a few studies and benchmarking have been done; therefore, the present study's results and comparisons can be used to improve the existing database. Finally and our primary goal, a turbulent bubbly pipe flow with high-density ratio and Reynolds number ($\gamma \approx 832$ and $\mathrm{Re}_\tau \approx 550$, respectively) is simulated, and the results are compared with the existing experimental data (Colin et al., 2012).

The comparison of the details of the turbulent bubbly flow simulations between the present study and some well-known references are given in Table 4.1. The table is adapted from the work of Bois (2017). As far as we know, most of the references employ a finite volume method (FVM) or finite difference method (FDM) with a

front-tracking (FT) or volume of fluid (VOF) method to simulate turbulent bubbly flows. A channel geometry is employed in those simulations, and the density ratio and Reynolds number are relatively low. However, significant progress has been made in terms of the number of simulated bubbles n_b as in the work of Cifani et al. (2018). As shown in Table 4.1, the present simulation is significantly different from the known references in terms of the employed methods, geometry, density ratio, and Reynolds number and comparable to the experimental setup. Although a reduced size domain is employed in terms of the problem size, the present resolution ($N_{tot} = N_x \times N_y \times Nz$) is relatively high in comparison to the other references.

4.4.4 Post-processing

The turbulent flow is characterized by vortices of different scales. To qualitatively indentify the turbulent structures, the streamwise vorticity and the Q-criterion values are calculated, which are respectively defined as:

$$\omega_x = \left(\frac{\partial u_z}{\partial y} - \frac{\partial u_y}{\partial z} \right), \tag{4.27}$$

$$Q = -\frac{1}{2} \left[\left(\frac{\partial u_x}{\partial x} \right)^2 + \left(\frac{\partial u_y}{\partial y} \right)^2 + \left(\frac{\partial u_z}{\partial z} \right)^2 + 2\frac{\partial u_y}{\partial x}\frac{\partial u_x}{\partial y} + 2\frac{\partial u_z}{\partial x}\frac{\partial u_x}{\partial z} + 2\frac{\partial u_z}{\partial y}\frac{\partial u_y}{\partial z} \right], \tag{4.28}$$

where u is the velocity and x, y, z are the spatial positions.

The first and second-order statistics are calculated to quantify the turbulence, which includes the void fraction distribution, the average streamwise velocity, the root mean square (RMS) of the velocity fluctuations, and the average Reynolds stress. The statistics are obtained along the wall-normal direction (radial direction for pipe) by averaging the values of interest (q) overall active grid points and at several time steps. The average and the root mean square or the fluctuation of the values of interest are respectively calculated as:

$$\langle q \rangle = \frac{\sum_{n=1}^{N} (\phi_n q_n)}{\sum_{n=1}^{N} \phi_n}, \tag{4.29}$$

$$\mathrm{RMS}(q') = \sqrt{\frac{\sum_{n=1}^{N} [\phi_n (q_n - \langle q_n \rangle)^2]}{\sum_{n=1}^{N} \phi_n}}, \tag{4.30}$$

where ϕ is the common phase-field variable and N is the total number of samples. To improve the statistics, the averaging is also performed between the reflective symmetry in the wall-normal direction (radial direction for pipe).

The agreement of a parameter (θ) obtained from the present simulation and the reference is assessed using the normalized root-mean-square error (NRMSE) defined as:

$$\mathrm{NRMSE} = \frac{1}{(\theta_{max}^{ref} - \theta_{min}^{ref})} \sqrt{\frac{1}{J} \sum_{j=1}^{J} (\theta_j - \theta_j^{ref})^2}, \tag{4.31}$$

where J is the number of grid points in Y-direction, the superscript ref indicates the reference value, and subscripts max and min denote the maximum and minimum value overall grid points in Y-direction, respectively.

4.5 Results and Discussions

4.5.1 3D bubble rising

The capability of the proposed method in simulating fundamental two-phase flow problems is demonstrated briefly hereafter. Four cases of 3D bubble-rising problems were simulated, and the results were compared with experimental results by Grace et al. (1976) and numerical results by van Sint Annaland et al. (2005) for brief validation of the proposed method.

3D bubble-rising problems can be characterized by different Morton and Eötvös numbers, as shown in Table 4.2. In these problems, density ratio $\gamma = 100$, viscosity ratio $\eta = 100$, gravitational acceleration $g = 9.8$, and initial bubble diameter $D_b = 0.01$ were set. The problems were simulated in a $0.04 \times 0.04 \times 0.1$ domain for a period of $T = 0.5$ using grid size $\Delta_x = 0.0005$ and time step $\Delta_t = \Delta_x/10$. No-slip boundary conditions were applied at walls.

Figure 4-4 compares instantaneous bubble shapes obtained by van Sint Annaland et al. (2005), shown at the top, and by the proposed method, shown at the bottom.

Table 4.2: Comparison of the terminal Reynolds numbers in 3D bubble-rising problem.

Case	Bubble regime	Mo	Eo	Grace et al. (1976)	van Sint Annaland et al. (2005)	Present
A	Spherical	1.26×10^{-3}	0.971	1.7	1.6	1.9
B	Ellipsoidal	0.1	9.71	4.6	4.3	4.7
C	Skirted	0.971	97.1	20	18	16.3
D	Dimpled	10^3	97.1	1.5	1.7	1.6

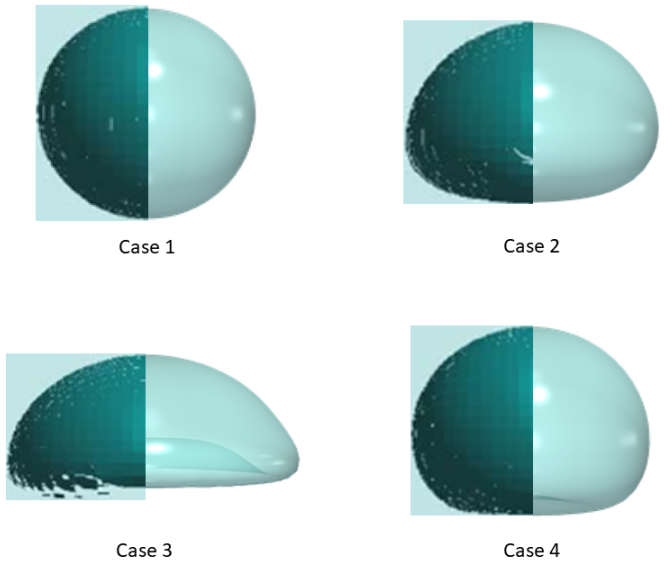

Figure 4-4: Comparison of bubble shapes in 3D bubble-rising problem. For each case, the bubble shape is split in half: one half obtained by van Sint Annaland et al. (2005) (left) and the other half obtained by the proposed method (right).

It can be seen from the figure that various bubble shapes can be simulated by the proposed method, and the present simulation results agree well qualitatively with those of the reference simulation. To quantify the agreement, the terminal Reynolds number, which is defined in the following equation, was calculated:

$$\mathrm{Re}_t = \frac{V_t D_b}{\nu_h}, \tag{4.32}$$

where V_t is the terminal velocity of the rising bubble. The terminal Reynolds numbers

obtained by the proposed method and the reference simulations are compared in Table 4.2. It can be seen from the table that the obtained Reynolds numbers agree well with those obtained by the reference simulations. It can therefore be expected that the proposed method can simulate various bubble shapes in the following simulations of turbulent bubbly flow.

4.5.2 Turbulent single-phase flows at low Reynolds number

In this section, the capability of the proposed method in simulating turbulent single-phase flows at low Reynolds number ($\mathrm{Re}_\tau = 180$) in both channel and pipe geometries are demonstrated. The problems have been simulated on three different grid sizes ($\Delta x = H/32, H/64, H/128$), correspond to ($\Delta y^+ = 5.6, 2.8, 1.4$), respectively, where $y^+ = yu_\tau/\nu$. The time step $\Delta t = \Delta x/1000$ was set. The present results are validated using those of Vreman and Kuerten (2014a) for chanel flow and El Khoury et al. (2013) for pipe flow, who employ spectral methods to solve the problems on a full-size domain.

The turbulent flows were initialized as follows. First, the streamwise velocity was initialized using a parabolic function, scalled by RNUM, a uniform random number between zero and one. The initial streamwise velocity distribution for the channel flow:

$$u_x(x, y, z) = \frac{G}{2\mu} y(H - y)\mathrm{RNUM}(x, y, z), \tag{4.33}$$

and for the pipe flow:

$$u_x(x, y, z) = \frac{G}{4\mu}(R^2 - r^2)\mathrm{RNUM}(x, y, z), \tag{4.34}$$

whereas, the spanwise velocity, the wall-normal velocity, and the pressure were set to zero. The turbulent flow was let to develop for a period of $T = 50H/u_\tau$ and then the statistics were collected every $\Delta T = 0.005H/u$ for a period of $T = 300H/u_\tau$.

Fig. 4-5 shows qualitatively the details of the turbulent structures obtained from the present simulations at an approximately statistically steady state. The areas with

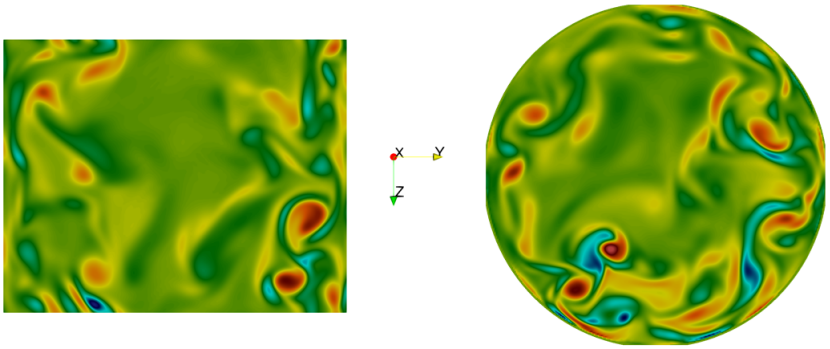

(a) Instantaneous streamwise vorticity contours at a $y-z$ plane.

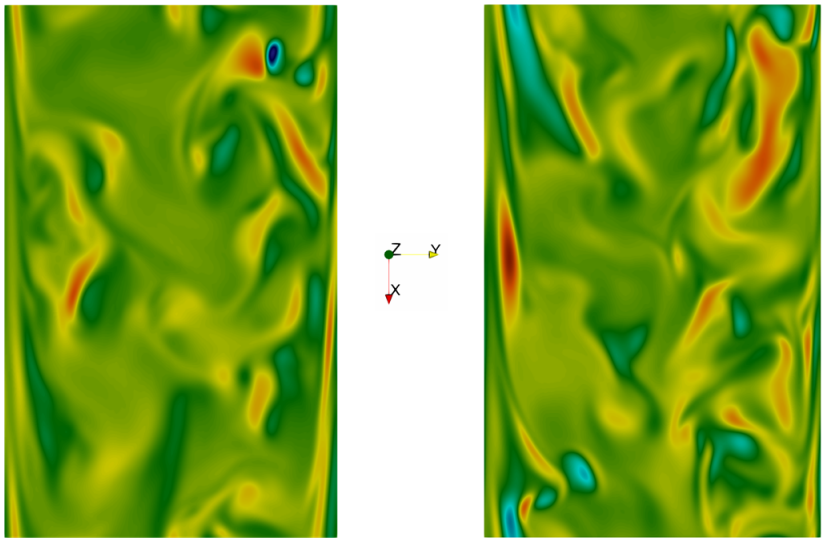

(b) Instantaneous spanwise vorticity contours at an $x-y$ plane.

Figure 4-5: Turbulent single-phase flow structures at low Reynolds number. Red and blue colours represent positive and negative values, respectively.

strong turbulence are colored in red and blue using the streamwise vorticity. The turbulent structures are more dominant near the walls than wall-bounded turbulent flows and generally are quite similar between channel and pipe flows. Relatively large turbulent structures can be seen as the Reynolds number is relatively low.

Fig. 4-6 shows the comparison of the turbulent statistics obtained from the present simulations and the references. As the resolution increases, the agreements between the proposed method and the references improve. Relatively good agreements are obtained using the smallest grid size ($\Delta y^+ = 1.4$). The NRMSE of the average streamwise velocity $<u>^+$, the root mean square of the streamwise velocity fluctu-

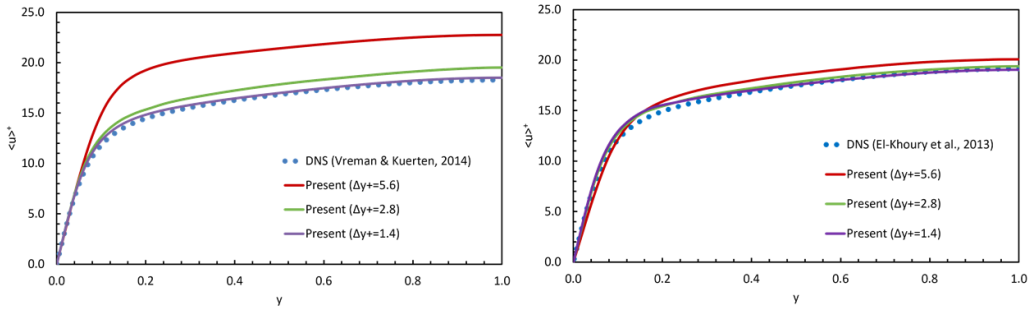

(a) Average streamwise velocity: channel (left) and pipe (right).

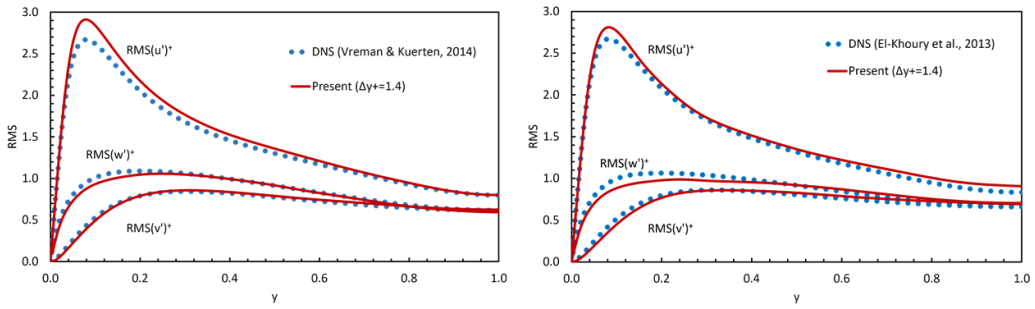

(b) Root mean square of the velocity fluctuations: channel (left) and pipe (right).

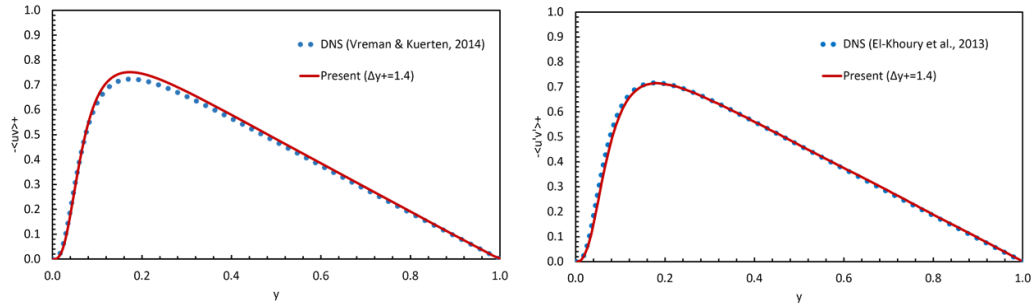

(c) Average Reynold stress: channel (left) and pipe (right).

Figure 4-6: Comparison of the turbulent statistics distribution of the turbulent single-phase flow at low Reynolds number obtained from the present simulation and the references, normalized by the friction velocity.

ations RMS$(u')^+$, and the Reynolds shear stress $-<u'v'>^+$ are about 1%, 3%, and 2% for the channel flow, and 2%, 2%, and 1% for the pipe flow, respectively, where turbulent statistics have been normalized by u_τ. The agreements are reasonable considering that $\Delta y^+ \leq 1$ is required to obtain accurate results by using DNS. It can be seen that the differences mainly occur in the buffer layer, which can be attributed to the use of the reduced-size domain, as also mentioned in Bois (2017). The convergence and the agreement to the reference results are generally better for the pipe flow

than the channel flow. Since the channel's streamwise length is equal to that of the pipe, perhaps the channel's spanwise length is rather significant and should be made longer for better accuracy. As demonstrated by the results, the proposed method can simulate the turbulent flows with relatively good accuracy using the given domain and grid sizes.

4.5.3 Turbulent single-phase flows at high Reynolds number

In this section, the capability of the proposed method in simulating turbulent single-phase flows at high Reynolds number ($\mathrm{Re}_\tau = 590$) for channel flow and ($\mathrm{Re}_\tau = 550$) for pipe flow are demonstrated. The problems have been simulated on grid size of ($\Delta x = H/256$) corresponds to ($\Delta y^+ = 2.3$) for channel and ($\Delta y^+ = 2.1$) for pipe. The present results are validated using the results by Vreman and Kuerten (2014b) for chanel flow and El Khoury et al. (2013) for pipe flow. To initialize the flow, the pressure and velocity distribution were interpolated from the final result of previous low Reynolds number simulation with grid size of $\Delta x = H/128$ and time step $\Delta t = \Delta x/1000$. The turbulent flow was let to develop for a period $T = 50H/u_\tau$ and the turbulent statistics were collected for a period of $T = 100H/u_\tau$, every $\Delta T = 0.005H/u_\tau$.

Fig. 4-7 shows the details of the turbulent structures qualitatively at a high Reynolds number obtained from the present simulations for both channel and pipe flows. The flow is characterized by a smaller turbulent boundary layer and many smaller turbulent structures than the previous low Reynolds number problem. The turbulent structures between the channel and pipe flows are quite similar.

Figs. 4-8 shows the comparisons of $<u>^+$, RMS$(u')^+$, and $-<u'v'>^+$ obtained from the present simulations and the references. Similar to the results obtained at low Reynolds number, the agreements with the reference results are better for the pipe flow than that of the channel flow, where the NRMSE of $<u>^+$ is about 3% for the pipe flow and 9% for the channel flow. Other than slightly larger Reynolds number ($\mathrm{Re}_\tau = 590$) and grid size ($\Delta y^+ = 2.3$), we think that the larger differences in the channel flow are due to the relatively short spanwise length. However, it is

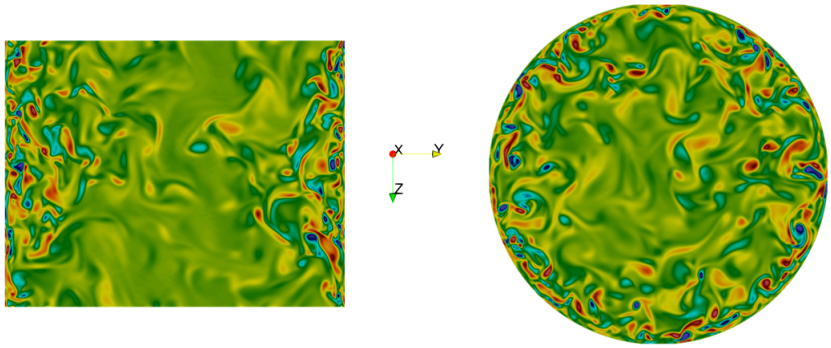

(a) Instantaneous streamwise vorticity contours at a $y-z$ plane.

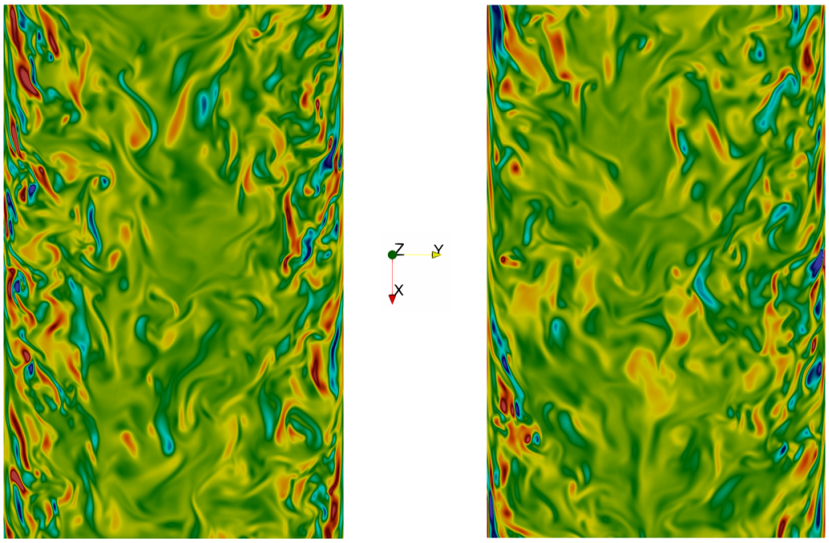

(b) Instantaneous spanwise vorticity contours at an $x-y$ plane.

Figure 4-7: Turbulent single-phase flow structures at high Reynolds number. Red and blue colours represent positive and negative values, respectively.

important to highlight that the proposed method can stably simulate the turbulent flows at high Reynolds numbers with relatively good accuracy using a rather coarse grid.

4.5.4 Turbulent Bubbly Channel Flow

In this section, the proposed method's capability in simulating turbulent bubbly channel flows with a low-density ratio and the Reynolds number are demonstrated. Two cases are simulated: the low void fraction problem $\alpha = 1.5\%$, first studied by Lu and Tryggvason (2006), and the high void fraction problem $\alpha = 19.4\%$, first studied

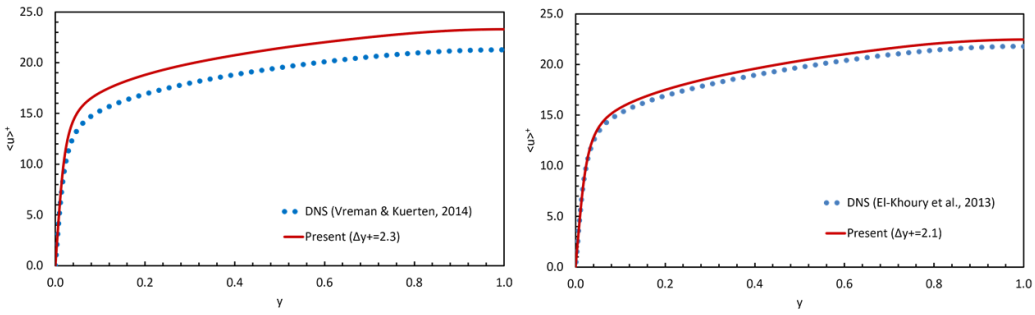

(a) Average streamwise velocity: channel (left) and pipe (right).

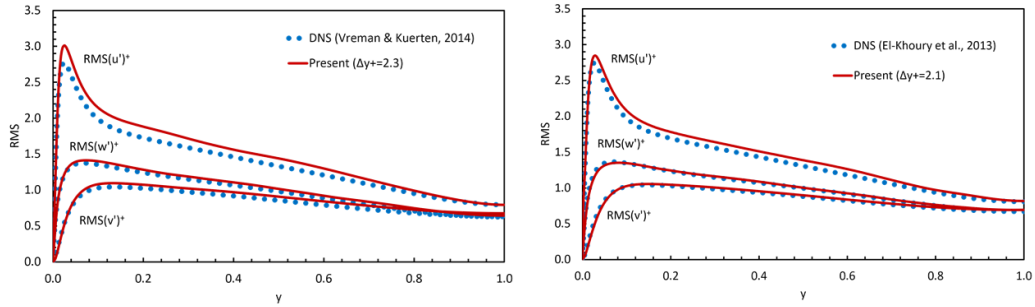

(b) Root mean square of the velocity fluctuations: channel (left) and pipe (right).

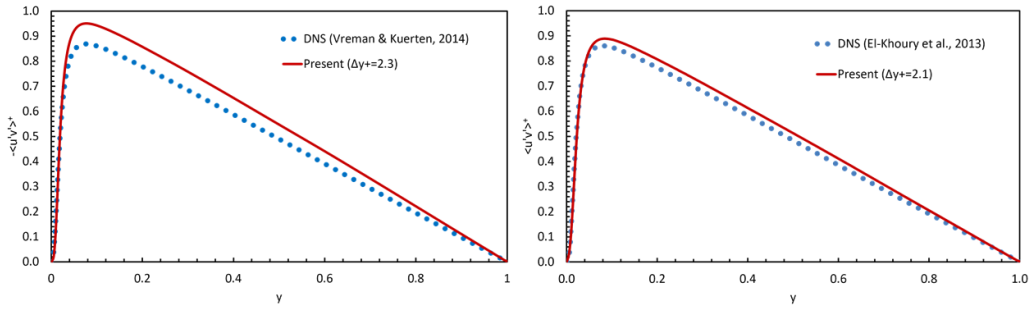

(c) Average Reynold stress: channel (left) and pipe (right).

Figure 4-8: Comparison of the turbulent statistics of the turbulent single-phase flow at high Reynolds number obtained from the present simulation and the references, normalized by the friction velocity.

by Cifani et al. (2018). The details of the parameters used for the problem are shown in Table 4.1. Additionally, the results obtained by Cifani et al. (2018) for $\alpha = 1.5\%$ are included as we learned that many variables affect the agreement between two results in turbulent bubbly flows, such as grid size, interface tracking, and how the turbulent statistics were obtained, to name a few (Cifani, 2017).

For both cases, the turbulent bubbly flow simulations started from the initial conditions obtained from the turbulent single-phase flow with $\mathrm{Re}_\tau = 127.3$. For

$\alpha = 19.4\%$, in Cifani et al. (2018), the applied pressure gradient was dynamically adjusted to keep the volumetric flow rate equal to that of the single-phase flow. It then appeared that the wall shear stress increases about 1.47 times, giving $\mathrm{Re}_\tau \approx 154.5$. In the present study, however, we have not tried to adjust the applied pressure gradient dynamically; instead, we simulated the case with $\mathrm{Re}_\tau = 180.0$.

The turbulent bubbly channel flow problems have been simulated using the grid size of $\Delta_x = H/100$ and time step $\Delta t = \Delta x/1000$. The turbulent single-phase flow with $\mathrm{Re}_\tau = 127.3$ was first calculated using the same grid size, and its final pressure and velocity distribution were used as the initial conditions. The computational domain was initially loaded with 18 and 234 spherical bubbles for $\alpha = 1.5\%$ and $\alpha = 19.4\%$, respectively. The turbulent flows were let to develop for a period of $T = 150H/U$ and the turbulent statistics were collected every $\Delta T = 0.075H/U$ for a period of $T = 180H/U$, where U is the average bulk velocity ($\mathrm{Re}_\tau = 127.3$). During the turbulent statistics collection, the computed wall shear stress has been in about 3% difference with its exact value.

Fig. 4-9 shows the instantaneous bubble distributions and Q-criterion values obtained from the present simulations at an approximately statistically steady state. The flow dynamics are very complex, where the bubble distributions affect the turbulent flows and vise versa. In Case 1 (Fig. 4-9a), the surface tension is strong enough that a spherical bubble shape is maintained. The bubble acts like a spherical obstacle that experiences a drag and a lift as the surrounding fluid flows past it. In the frame of reference of the moving bubble, the lift force will push the bubble towards a faster surrounding fluid region where the pressure is low. The bubble will be pushed toward the channel's center for a downward flow, forming a bubble-free region near the walls. Vortices are created from each bubble, adding velocity fluctuations in the flow as shown by Q-criterion values. The bubbles tend to form a cluster as low-pressure regions are created at the wakes. The near-wall vorticities are not affected much as there are few bubbles, and they gather relatively far from the wall.

In Case 2 (Fig. 4-9b), the bubbles deform into ellipsoidal shapes due to the smaller surface tension effect. The drag and the lift of the bubbles are affected as the bubbles

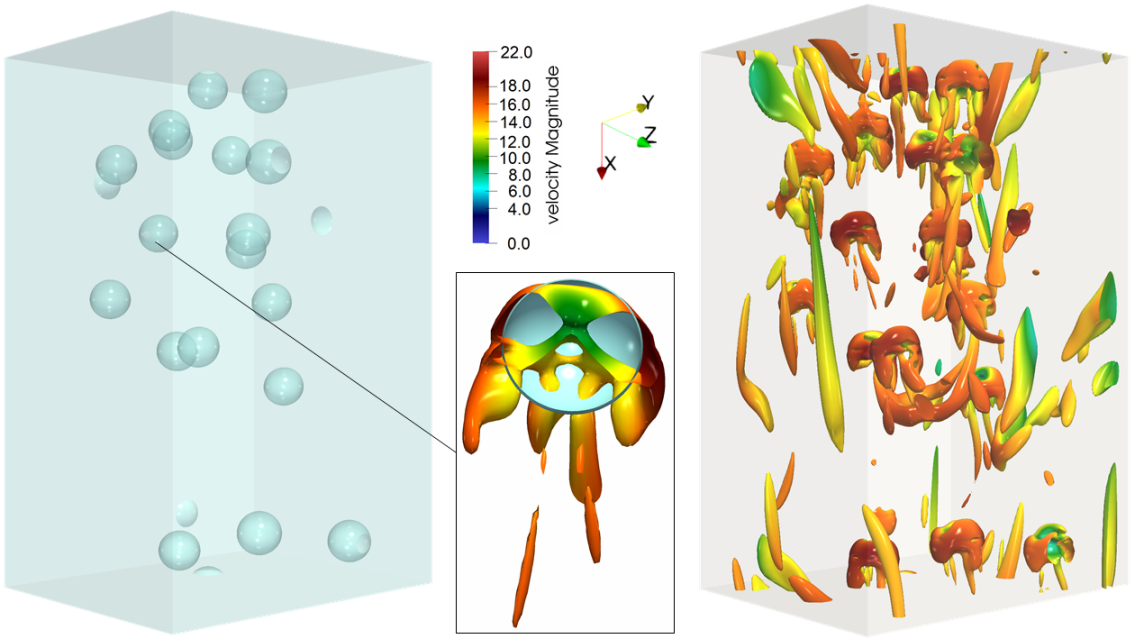

(a) Case 1 ($\alpha = 1.5\%$), bubble distributions (left), Q-criterion values (right).

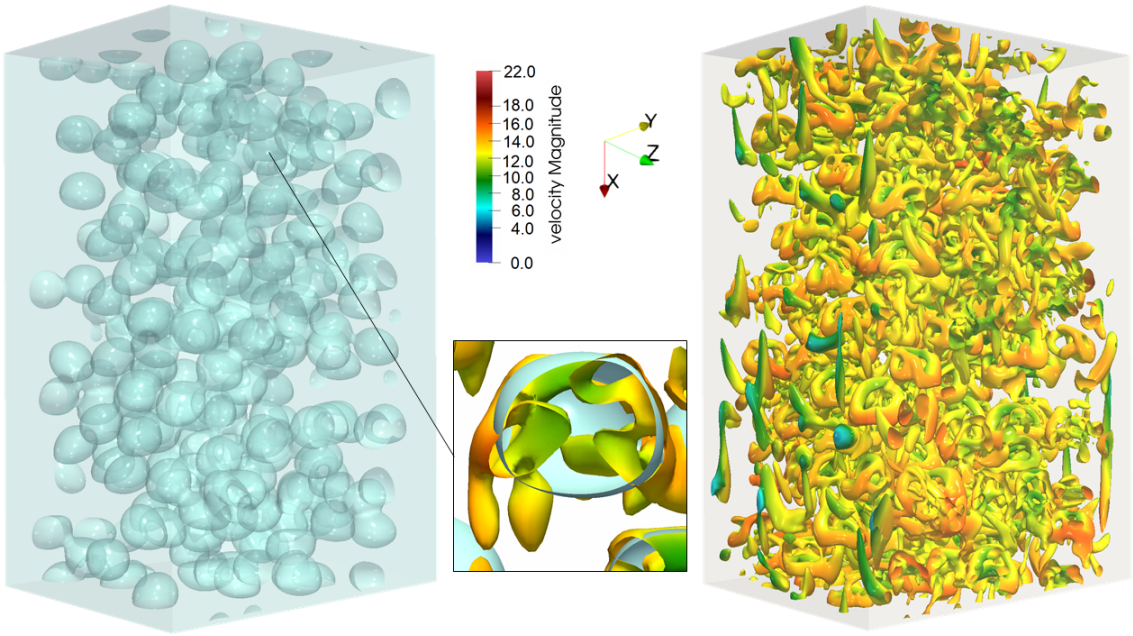

(b) Case 2 ($\alpha = 19.4\%$), bubble distributions (left), Q-criterion values (right).

Figure 4-9: Instantenous bubble distributions and Q-criterion values in the turbulent bubbly channel flows.

deform. The bubbles in Case 2 move more freely than in Case 1. The vortex shedding effect is suppressed as the distance between each bubble is very close, as shown by the Q-criterion values, resulting in weaker and more spread out vortices. The near-wall

vorticities are quite affected as some bubbles come close to the wall.

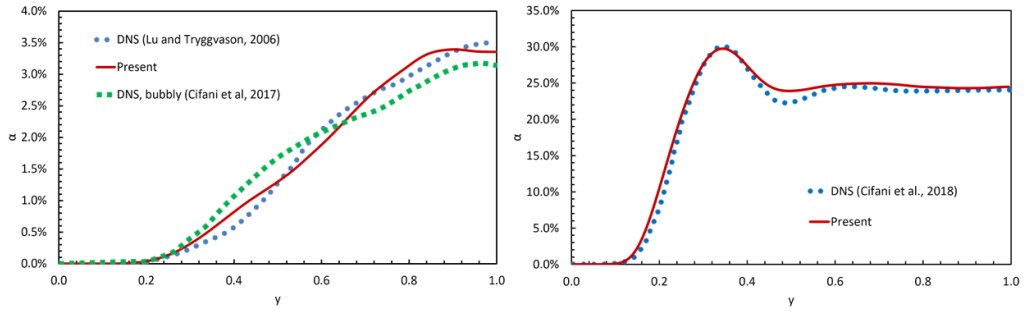

(a) Void fraction distribution.

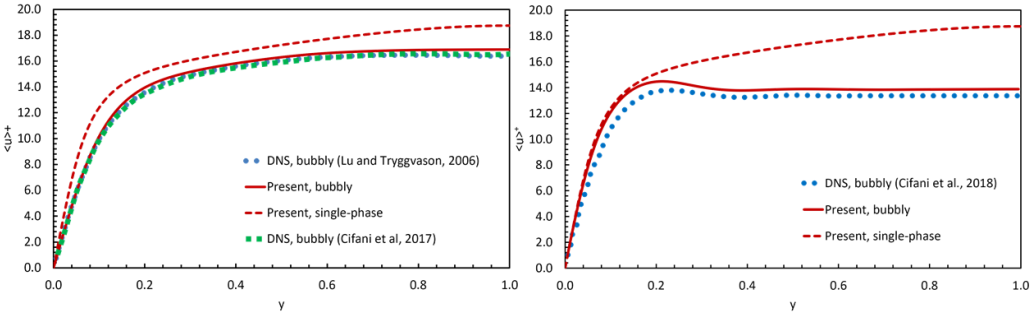

(b) Average streamwise velocity distribution.

Figure 4-10: Comparison of the first-order turbulent statistics in the turbulent bubbly channel flow obtained from the present simulation and the references: $\alpha = 1.5\%$ (left) and $\alpha = 19.4\%$ (right).

Fig. 4-9 shows the comparison of the average void fraction and streamwise velocity obtained from the present simulations and the references. The obtained results are in relatively good agreement with the references. The NRMSE of the average void fraction α and u^+ are about 4% and 2% in Case 1, and 2% and 4% in Case 2, respectively. As shown in Fig. 4-9, the bubbles tend to gather at the center of the channel, suppressing the streamwise velocity and make the distribution at the center become relatively uniform. For downward flows, the weight of the mixture is greater than the applied pressure gradient so that β gives a positive value. In the central region, the shear stress approaches zero so that the local void fraction is approximately $\beta/\Delta\rho g$ higher than the average. The summation of β and the shear stress then gradually falls to zero at the transition region and $-\bar{\alpha}\Delta\rho g$ near the walls, corresponding to the gradual fall of the local void fraction to the average and zero values, respectively. In

Case 1, the local void fraction change in the transition region is very smooth due to the meandering of the bubbles as the void fraction is meager. In Case 2, a peak of the void fraction at the transition region observed in the experiment is also well captured by the present simulation. This transition region's thickness and shape depend on many variables such as bubble size, void fraction, and Reynolds number.

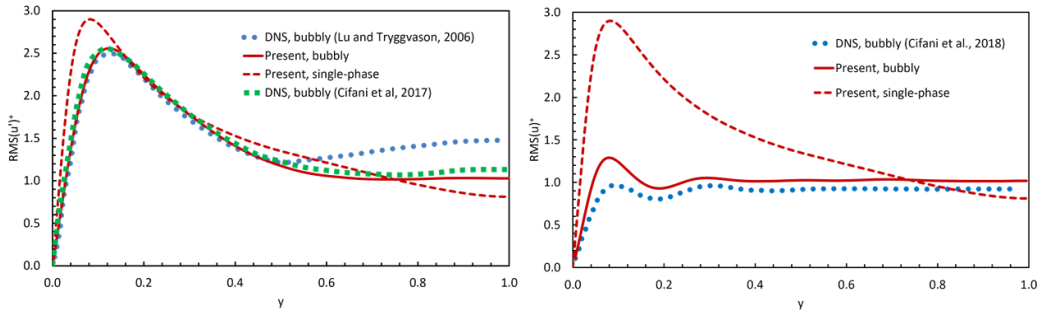

(a) Root mean square of the streamwise fluctuation distribution.

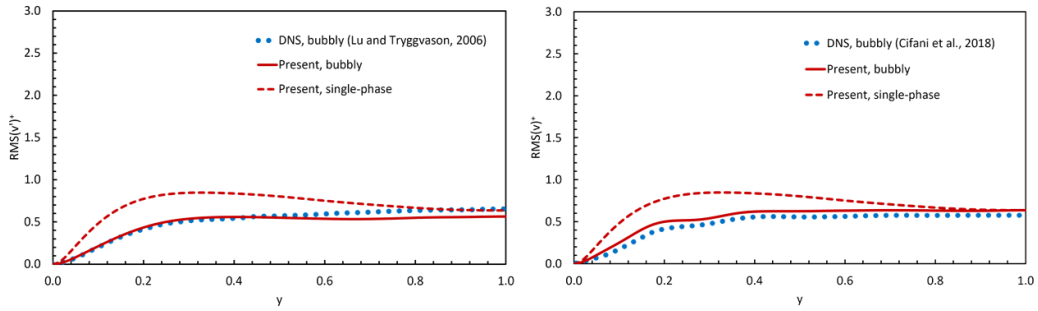

(b) Root mean square of the wall-normal velocity fluctuation distribution.

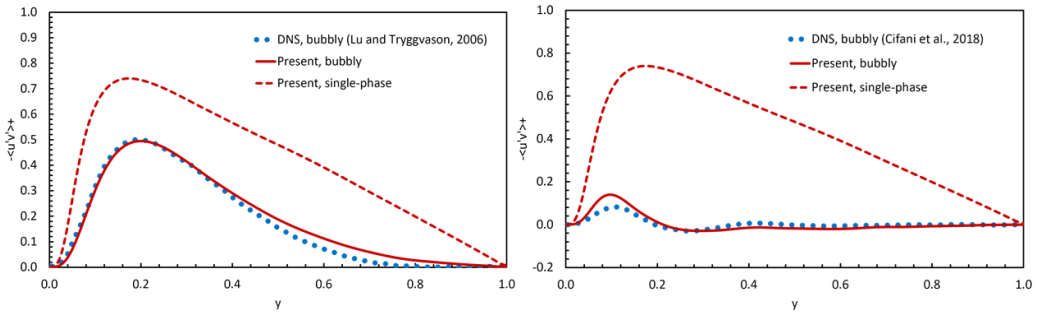

(c) Reynold stress distribution.

Figure 4-11: Comparison of the second-order turbulent statistics in the turbulent bubbly channel flow obtained from the present simulation and the references: $\alpha = 1.5\%$ (left) and $\alpha = 19.4\%$ (right).

Fig. 4-11 shows the comparison of the RMS of streamwise and wall-normal velocity fluctuations and the Reynold stresses obtained from the present simulations and the

references. In Case 1, at the central region, the streamwise velocity fluctuation of the bubbly flow increases compared to that of the single-phase flow, which can be attributed to the vortex shedding from each bubble, as previously mentioned. At the transition region, the velocity fluctuation decreases as the average streamwise velocity is flatter than that of the single-phase flow and fewer bubbles exist than in the central region. Both the normal and Reynolds stress are also suppressed by the bubbles so that the flow becomes less turbulent.

However, the increase of the streamwise velocity fluctuation in the present simulation is not as significant as that obtained by Lu and Tryggvason (2006) but comparable with that obtained by Cifani et al. (2018). A good agreement is obtained where the NRMSE of streamwise velocity fluctuations is about 3% compared with the result by Cifani et al. (2018). The difference with Cifani et al. (2018) probably comes from how the turbulent statistics were calculated, as also mentioned by Cifani (2017). The statistics are supposed to be calculated for the heavy fluid only; however, the interface definition among methods can differ. The other difference can also come from the difference in grid size used. A uniform grid with a size of $\Delta y^+ = 1.3$ is used in the present simulation. A non-uniform grid ranged from $\Delta y^+ = 0.79$ near the wall to $\Delta y^+ = 2.19$ in the central region is used in the reference.

In Case 2, the turbulence is significantly suppressed by the presence of many bubbles, shown by the large decrease in the streamwise and wall-normal velocity fluctuations and the Reynold stresses. The flow becomes more uniform and less fluctuating compare to Case 1. As more bubbles and the bubbles are deformable, it is harder to get a good agreement in Case 2 than in Case 1. Reasonably good agreements obtained where NRMSE of streamwise velocity fluctuations is about 14% with the maximum difference occurs at the overlap region. The results discussed in this section show that the proposed method can stably simulate the simplified turbulent bubbly flows problem with a relatively good agreement with the references.

4.5.5 Turbulent Bubbly Pipe Flow

In this section, the capability of the proposed method in simulating a turbulent bubbly pipe flow with high-density ratio ($\gamma = 831.7$) and Reynolds number ($\mathrm{Re}_\tau = 550$) is demonstrated. The details of the parameters used in the present simulation are shown in Table 4.1, which are comparable with the experimental values by Colin et al. (2012). The problem was simulated using the grid size of $\Delta x = H/256$ and time step $\Delta t = \Delta x/1000$. The pressure and velocity distributions obtained from the turbulent single-phase pipe flow ($\mathrm{Re}_\tau = 550$) at the final time were used as the initial conditions for the present simulation. The computational domain was initially loaded with 225 spherical bubbles. Due to the heavy computations, however, the flow was let to develop for a period of $T = 20H/U$, and then the turbulent statistics were collected every $\Delta T = 0.1H/U$, for a period of $T = 40H/U$, where U is the average bulk velocity ($\mathrm{Re}_\tau = 550$). Up to this time, the statistically steady state has not been achieved yet, and the average wall shear stress was about 1.38 times the exact value. Because of this reason, the turbulent statistics obtained from this section have been normalized by setting the computed wall shear stress to unity. All turbulent statistics obtained in the previous sections have not been normalized to the exact shear stress.

Fig. 4-12 shows the instantaneous bubble distribution (left) and the Q-criterion value (right) obtained by the present simulation at $T = 20H/U$. The bubble shapes are in good agreement with Clift et al. (1978) where the ellipsoidal or wobbling shapes are obtained. The bubble shape is also similar to that obtained by Bois (2017), as the Morton and Eotvos number are similar. As they are easily deformed, the bubbles move more freely than in the previous bubbly channel flow problems. At $T = 20H/U$, the bubbles have been distributed and gathered in the pipe center. The flow becomes much more complex than the previous channel flow problems shown by the Q-criterion value, where vorticities with small sizes and various shapes occur in the whole domain. The vortex shedding can still be seen behind each bubble as the distance between each bubble is not too close. Fig. 4-13 shows the comparison velocity field inside

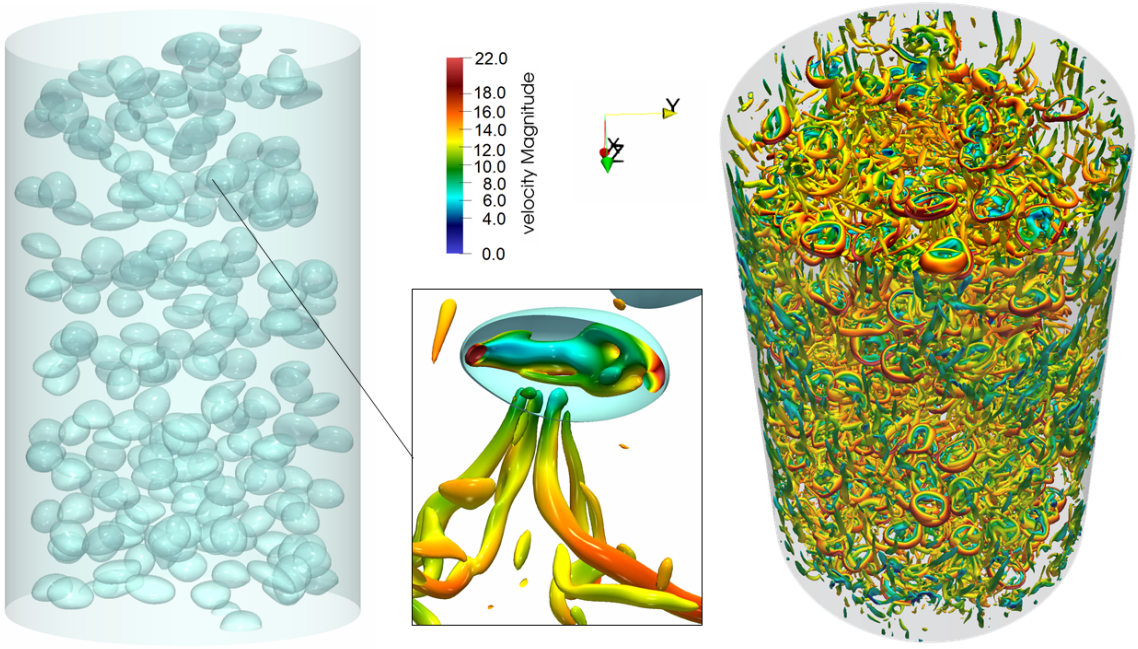

Figure 4-12: Instantenuos bubble distribution (left) and Q-criterion value (right) in the turbulent bubbly pipe flow obtained from the present simulation.

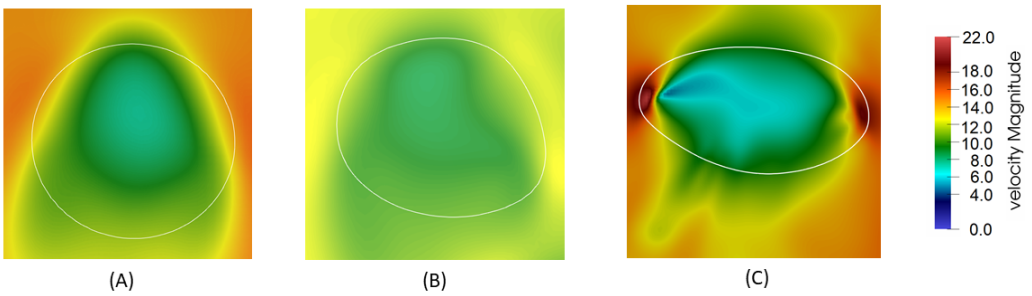

Figure 4-13: The comparison of the velocity field inside and around a single bubble obtained from the present simulation. Turbulent bubbly channel flow with $\alpha = 1.5\%$ (A), $\alpha = 19.4\%$ (B) and turbulent bubbly pipe flow with $\alpha = 9.5\%$ (C).

and around a single bubble obtained from the present simulation. In the previous turbulent bubbly channel flows, the bubble deformation and the Reynolds number are relatively small so that the velocity field inside and around the bubble is relatively smooth. However, due to greater deformation and Reynolds number in the turbulent bubbly pipe flow, large variations in the velocity field occur. The highest velocity magnitude occurs at the side of the bubble, and the velocity field is very fluctuating behind the bubble. The velocity contour from the inside to the outside of the bubble is

smooth for all cases. The velocity-based formulation helps to stabilize the simulations, especially for high-density ratio and Reynolds number problems.

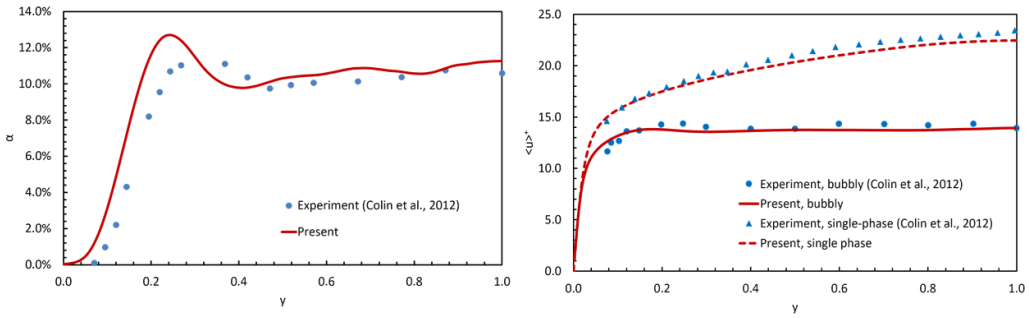

Figure 4-14: Comparison of the first-order turbulent statistics in the turbulent bubbly pipe flow. The average void fraction distribution (left) and the average streamwise velocity, normalized by the friction velocity (right).

Fig. 4-14 shows the comparison of the first order turbulent statistics obtained by the present simulation and the reference. The obtain void fraction profile is similar to that of Case 2 of the bubbly channel flow problem, where the void fraction distribution is relatively flat at the center and gradually decreases in the transition region. The peak at the transition region is also captured in the present method, which also exists in the experiment. Reasonably good agreement is obtained with the experimental results, where the average relative difference of void fraction distribution is about 12%. Similar to the previous bubbly channel flow problems, the bubbles' presence suppressed the streamwise velocity, so the flow becomes homogeneous. However, the streamwise velocity fluctuation behavior is quite different from that of the previous bubbly channel flow problems. As a note, the average void fraction in this problem is $\alpha = 9.5\%$, which is between those of the previous bubbles channel flow problems ($\alpha = 1.5\%$ and $\alpha = 19.4\%$). Although the number of bubbles is relatively high, the distance between each bubble is relatively moderate, so that vortex sheddings occur and increase the streamwise velocity fluctuation in the central region. This behavior is also observed in Lu and Tryggvason (2006) in which the average void fraction ($\alpha = 6\%$).

Fig. 4-15 shows the second-order turbulent statistics obtained by the present simulation. The streamwise velocity fluctuation near the walls is slowly affected as only

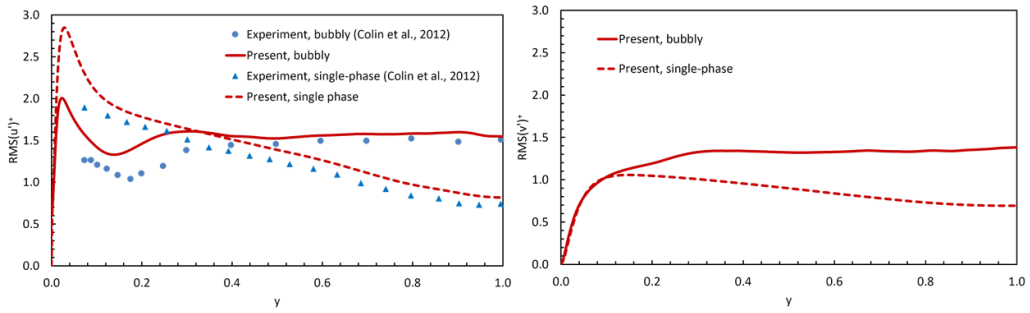

(a) RMS of the streamwise (left) and radial (right) velocity fluctuations.

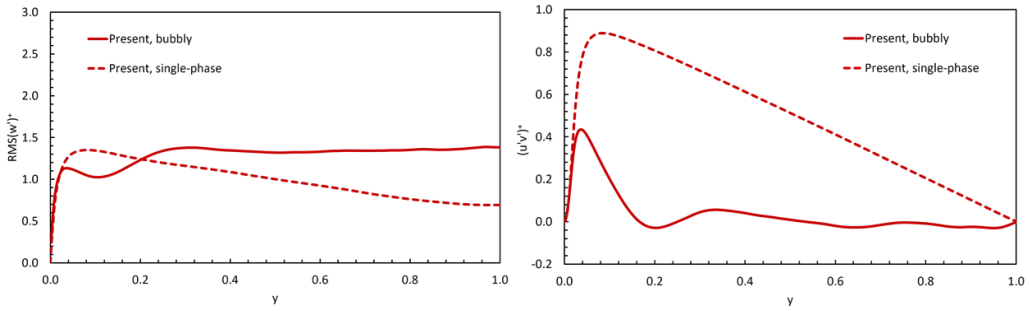

(b) RMS of the circumferential velocity fluctuations (left) and Reynolds stress (right).

Figure 4-15: Comparison of the second-order turbulent statistics in the turbulent bubbly pipe flow, normalized by the friction velocity.

a few bubbles come close to the wall, and long time integration is required to obtained steady-state conditions. Generally, the behavior of the turbulent bubbly pipe flow is similar to that of previous bubbly channel flows, although the bubble shapes, the turbulent structures, and the computed value of the turbulent statistics are different. Good agreement is obtained, where the NRMSE of the average streamwise velocity and RMS of the streamwise velocity fluctuations are about 4% and 13%, respectively. The turbulence becomes homogenous as shown by approximately zero Reynolds stress in the central pipe region, similar to the previous turbulent bubbly channel flow problems. However, the RMS of the radial and circumferent velocity fluctuation distribution is quite different, where the magnitude of the velocity fluctuations at the pipe center becomes similar in all directions. This behavior is not yet understood; however, this shows that the simplified settings' behavior differs from the real one. Therefore, the proposed method is expected to be useful for studying turbulent bubbly flows in more realistic settings in the future.

4.6 Conclusions

A cumulant lattice Boltzmann method with a multi-phase model has been developed for simulating turbulent bubbly channel flow with high density and viscosity ratio. The proposed method has been tested using several cases, which include single and multiple bubble risings, simplified turbulent bubbly flows, and turbulent bubbly flows of a water-air system with high void fraction and Reynolds number. The results show that our proposed method can stably simulate the problems and is in good agreement with the computational and experimental references.

The turbulent bubbly downflows with low-density ratio ($\gamma = 10, \mathrm{Re}_\tau \approx 180, \alpha =$ 1.5% and 19.4%) in a channel were simulated and compared with the reference. The results show that the obtained flow's general behavior is the same as the reference where the bubbles tend to fill the center of the channel and suppressed the center's mean velocity. Vortices appear behind the bubbles as bubbles act as obstacles. A turbulent bubbly downflow for a water-air system ($\gamma \approx 831.7, \mathrm{Re}_\tau = 550, \alpha = 9.5\%$) in a pipe has been simulated. The results show that the bubbles are more deformed and dispersed. More vortices appear in this case than in the low-density ratio case and the mean velocity is suppressed more homogeneously. This result shows that using the low-density ratio for simulating the water-air system may not be correct. The turbulence are sensitive to change in bubble properties, void fraction, and Reynolds number and therefore, an accurate method that can simulate the real flow conditions is necessary. In the present simulation, the NRMSE of bubble distribution, mean streamwise velocity, and streamwise velocity fluctuation are about 12%, 4%, and 13%, respectively.

Chapter 5

Cumulant LBM for Foam Simulations

5.1 Introduction

Wet foam is created when dispersed bubbles stack on the liquid surface without bursting. When the water between those stacked bubbles drains, a micrometer-thin film of liquid between bubbles are created, creating a dry foam. The thin film can be stable when stabilization mechanisms exist such as the Marangoni effect. Several examples of a foam formation include beer, bread, whipped cream, styrofoam, detergents, and firefighting foam.

The modeling and simulation of foam formation are challenging. The liquid film is very thin compared to the bubble diameter, which requires multi-scale modeling. Even with an Adptive Mesh Refinement, it is currently impractical to fully resolve the thin film, especially when there are many bubbles. The physics is very complex if the material transport and heat transfer via liquid film are considered.

Front-tracking and interface-capturing methods are two conventional numerical methods used to simulate interfaces. Front tracking methods simulate the interface by using particles. They can simulate multiple interfaces in one cell and represent a thin liquid film; however they face difficulty in handling topological change. They require a reconnection scheme to describe breakup and coalescence, which limit its efficiency.

Interface capturing methods such as the Volume of Fluid (VOF) and Level-Set (LS) methods simulate the interface on a fixed grid. The methods can handle topological change; however, one cell can only contain one interface. Therefore, bubbles and drops always coalesce at distances shorter than one cell, a condition called the numerical coalesce.

Interface capturing methods have become standards in liquid-gas two-phase flow simulations. The mehods have also been developed to simulate cases of non-coalescing bubbles, where separate marker functions are used to represent dispersed non-coalescing bubbles. Several researchers have used a multi-marker LS method to prevent the coalesce of bubbles. Similar to the original LS method, the multi-marker LS method faces difficulty in conserving mass. Several approaches have been developed to overcome the difficulty; however, with reduced computational efficiency. A multi-marker VOF method has been employed with good efficiency; however, they face difficulty calculating surface tension and flow with arbitrary boundaries. We propose an algorithm that implements the cumulant lattice Boltzmann method for gas-liquid two-phase flow and introduce a multi-phase field model to simulate non-coalesce bubble in foam formation. The method is efficient to be applied for parallel computations.

5.2 Numerical Methods

In this study, we also employ the Incompressible Navier-Stokes Equations (INSE), one fluid model, and multi-marker approach based on multi-phase field model, as described in Chapter 4. The topology of the bubble cluster modeled using the multi-phase field model is shown in Fig 5-1. In the single-phase field model, the gas bodies are modeled using a single-phase field variable, and the gas bodies are represented by zero phase-field value. The gas bodies will automatically coalesce when they come close, and their interfaces are within one cell. In the case of the multi-phase model, each gas body is given a separate phase-field variable, and multiple interfaces can be simulated even if they are within one cell. The coalescing of the gas bodies can then be prevented. The thin liquid films are reconstructed from separate phase-field

variables using the following function:

$$\phi_g(\mathbf{x},t) = max\left(\phi_1(\mathbf{x},t), ..., \phi_{ngb-1}(\mathbf{x},t), \phi_{ngb}(\mathbf{x},t)\right), \tag{5.1}$$

where ϕ_g is the global phase-field variable and the index ngb is the number of gas bodies. The application of the multi-phase field model, however, leads to additional difficulties. The first one is that the phase-field value in gas bodies is not zero as in the single-phase field model, leading to the oscillation of phase-field value when the flow divergence is non-zero. These issues can be suppressed by simulating the liquid phase and normalizing the phase-field value with all phases' summation. This study adds an iterative pressure projection method to reduce the compressibility error and thus reduce the phase-field variable's oscillation. Since our proposed cumulant LBM decouples the pressure from the lattice kinetics, the iterative pressure projection method can be applied straightforwardly.

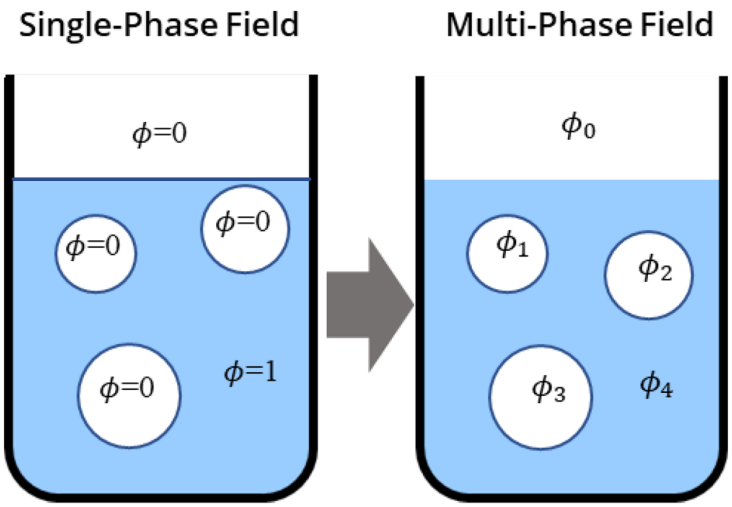

Figure 5-1: The topology of the bubble cluster by MPF method.

The following iterative pressure projection method developed by Yang (2019) is used to advance the numerical solutions of velocity and pressure to the next time step. Then the following iteration process is conducted for N steps:

1. compute the increment of pressure δp and update the temporary pressure $p^{*,i}$

to $p^{*,i+1}$,

$$\delta p = -\rho c_s^2 \cdot \mathbf{u}^{*,i} \Delta t, \tag{5.2}$$

$$p^{*,i+1} = p^{*,i} + \delta p. \tag{5.3}$$

2. update velocity field $\mathbf{u}^{*,i}$ to $\mathbf{u}^{*,i+1}$ by projecting the increment of pressure,

$$\mathbf{u}^{*,i+1} = \mathbf{u}^{*,i} - \frac{\Delta t}{\rho} \nabla \delta p. \tag{5.4}$$

where p^* and u^* is the intermediate pressure and velocity, and the superscript i indicates the current step of iterations and starts from 0. The final solutions of velocity and pressure at step $n+1$ are given by

$$p^{n+1} = p^{*,N}, \tag{5.5}$$

$$\mathbf{u}^{n+1} = \mathbf{u}^{*,N}. \tag{5.6}$$

The assumption of incompressible fluid means an infinite speed of sound, and thus a pressure change anywhere will be transmitted throughout the fluid immediately. As for the weakly compressible fluid under consideration, the above iterative pressure projection method has a physical meaning to propagate the perturbation multiple times by a finite sound speed (Yang, 2019).

5.3 Results and Discussions

We revisited the 2D bubble rising problem in Chapter 3. The cumulant LBM, combined with the iterative pressure projection method, is employed to simulate the problem. Fig. 5-3 show the final bubble shapes and the rising velocities. It can be seen that the cumulant LBM with iterative pressure projection can suppress the oscillation of the rise velocity caused by unsatisfied incompressibility condition. The bubble shapes from the present calculations are also in good agreement with the reference results.

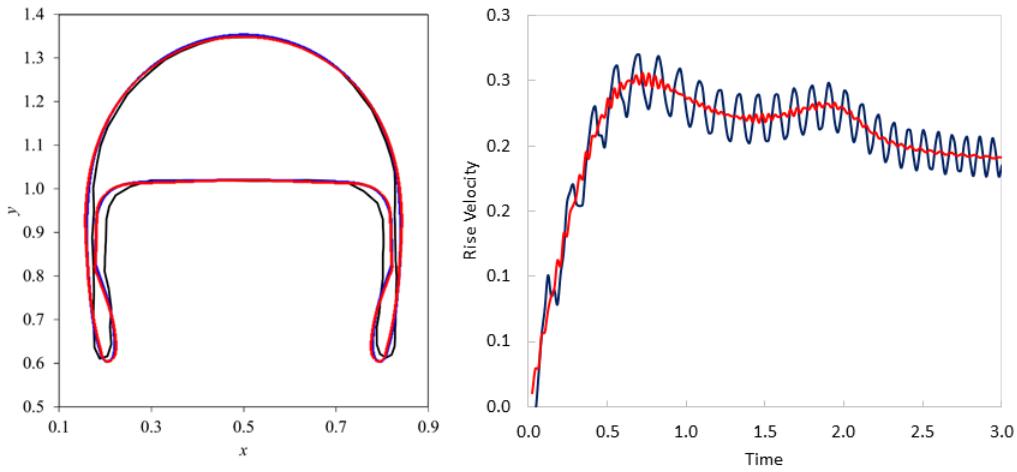

Figure 5-2: Bubble shapes at final time (left) and rise velocity (right) for Case 2 of the 2D rising bubble problem. Cumulant LBM with 10 pressure iterations (red), cumulant LBM without pressure iteration (blue). References: TP2D (Hysing et al., 2009) (solid black) and Abels (Aland and Voigt, 2012) (dashed black).

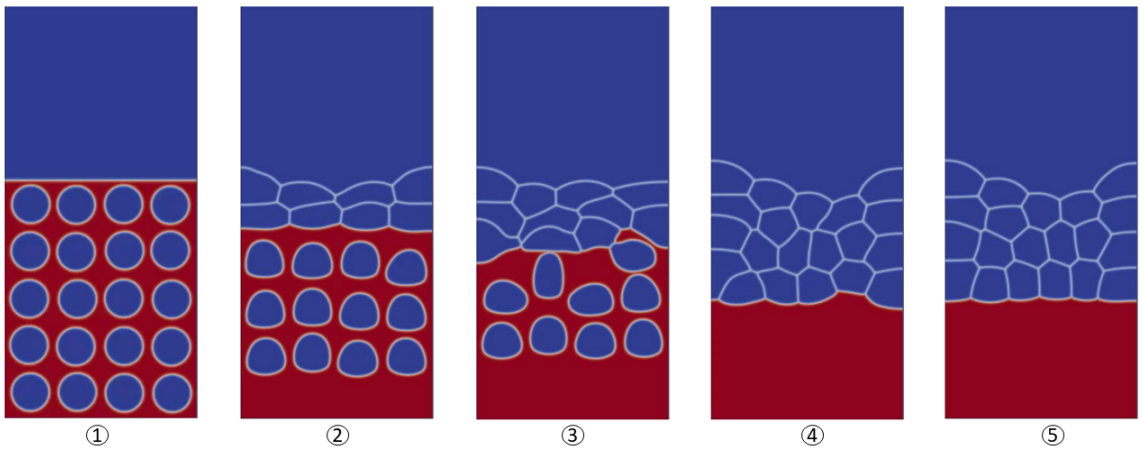

Figure 5-3: Snapshots of a 2D foam development.

Using the proposed method, we can simulate the foam formation without volume loss. In Fig. 5-3, we raise 20 bubbles to form a foam in 2D, where the density ratio $\gamma = 1000$, the viscosity ratio $\eta = 100$, the Eotvos number Eo $= 9$, and the Morton number Mo $= 0.0026$. The lattice size is 200×500. In Fig. 5-4, we simulated the foam formation in 3D. We raised 200 bubbles of various sizes. The soapy water parameter setting is used where $\gamma = 831$, $\eta = 100$, gravity $g = 9.8$, and surface tension $\sigma = 0.025$. The computational domain size is $0.2 \times 0.2 \times 0.48$ and discretized using grid size of $200 \times 200 \times 480$. The foam formation with thin liquid films has been stably simulated

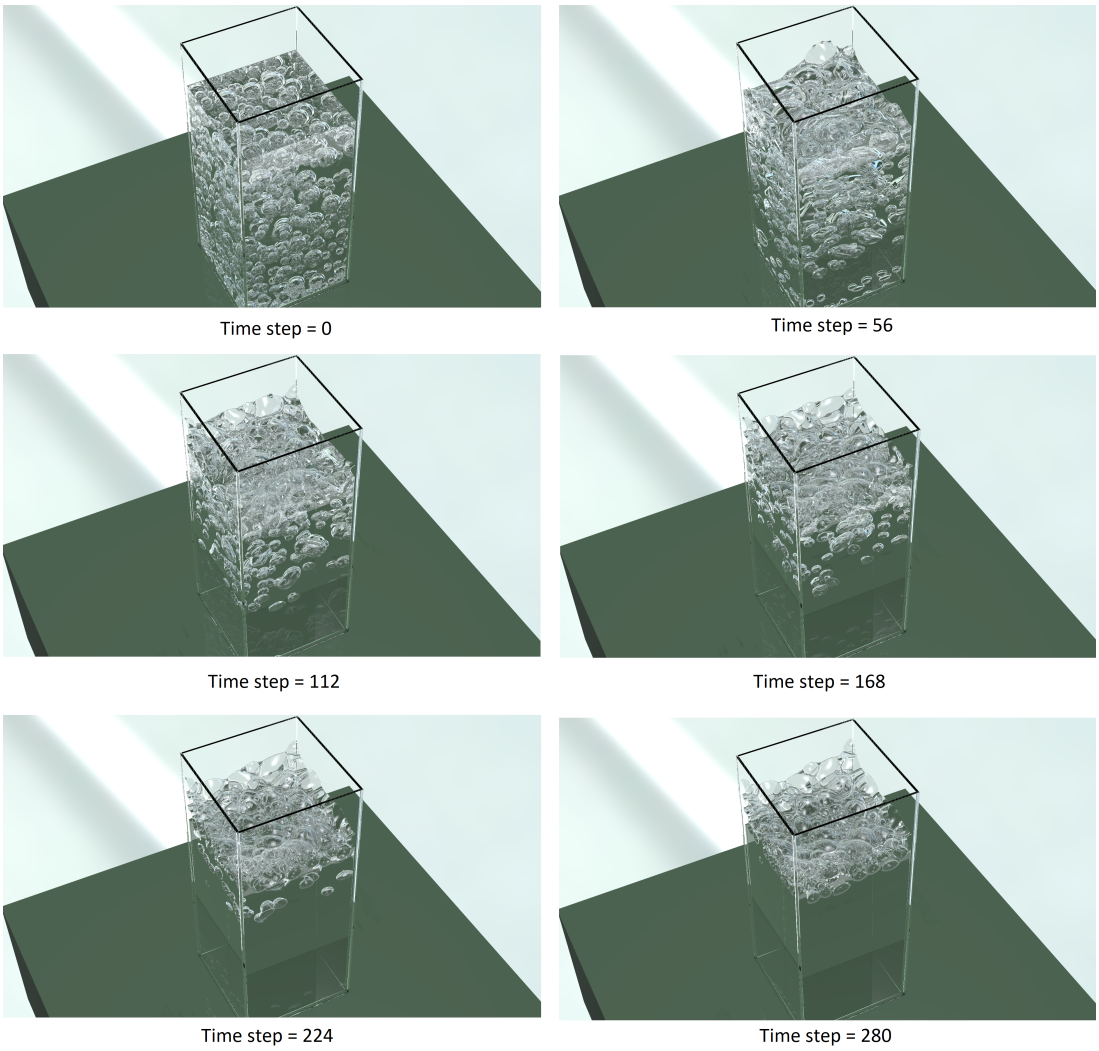

Figure 5-4: Snapshots of a 3D foam development.

by using the proposed method. The bubbles stack on the liquid surface and form a dry foam. Currently, the foam in the present simulations will never break. An algorithm for handling bubble coalesce should be developed and studied in the future.

5.4 Conclusions

A cumulant LBM with multi-phase field model for simulating multiphase flows with non-coalescing bubbles has been developed. We have reduced the compressibility error using an iterative pressure projection method. 2D and 3D foam formations have been stably simulated, and thin liquid films are well presented. Our model allows us to

describe the formation of clusters of bubbles on the surface seperated by thin liquid films, which show foam's characteristic features.

Chapter 6

Conclusions

6.1 Summary

Lattice Boltzmann Method (LBM) has become a popular alternative for simulating fluid flows due to its simple kinetic equation. It has several advantages: it does not solve the pressure Poisson equation, it can simulate flows with complex geometries and high-Reynolds numbers, and it is efficient for parallel computing. Because of its promising features, LBM is continually being extended for a broader range of applications.

Three topics have been studied in this dissertation:

1. **Violent two-phase flow** simulations with high-density ratio and Reynolds number: One example of this flow is the dam-breaking, which is important in civil and marine engineering. The problem has been simulated using the free-surface model, where the gas phase dynamics are neglected. Although it can simulate the free-surfaces, the free-surface model is not realistic in simulating the dynamics of droplets and bubbles generated from the free-surfaces. In case of two-phase flow model, the gas phase is considered; however, there was no successful simulation using LBM, especially for high-density ratio ($\gamma \approx 1000$) and high Reynolds number ($\mathrm{Re} \approx 10^5$). Therefore in this thesis, we developed a novel cumulant LBM to simulate the problem successfully for the first time.

We also studied a liquid jet breakup with a high-density ratio and Reynolds number using the proposed method. This problem was studied in a low-density ratio in the past.

2. **Turbulent bubbly pipe flow** with high-density ratio and Reynolds number: The problem is essential in the design and operation of power and chemical plants. In the past, the turbulent bubbly flow problem has been studied in simple channel geometry, low-density ratio ($\gamma \approx 10$), and low Reynolds number ($\mathrm{Re}_\tau \approx 180$). Although they can capture the general behavior such as the bubble and velocity distribution across the channel, the simple model is not accurate in capturing the flow behavior in experimental and industrial settings. By using our proposed cumulant LBM, we can simulate the turbulent bubbly flow problem pipe geometry, high-density ratio ($\gamma \approx 832$), and high Reynolds number ($\mathrm{Re}_\tau \approx 550$) successfully for the first time.

3. **Foam formation** simulations with thin liquid films and many bubbles: The problem is essential in material and heat transfer research and is difficult due to its multi-physics and multi-scale nature.

Our proposed cumulant LBM is based on a velocity-based formulation of two-phase LBM for hydrodynamics. The formulation is numerically stable due to its small incompressibility error and semi-implicit velocity update. A cumulant collision model has been incoorperated for the first time for two-phase flow to stably simulate high Reynolds flows. For interface capturing, we apply a phase-field model that conserves mass and has good accuracy. The method is also extended to a multi-phase field model to simulate non-coalescing dispersed bubbles. The combined algorithm is efficient to be used in parallel computation.

By simulating the three topics mentioned above, the proposed method is validated for various problems and is expected to be useful for simulating more complicated problems in the future. The summary and conclusions of each topic are given in the following.

6.1.1 Violent flow simulations

This work presents a novel filtered cumulant LBM, which has been developed to solve violent two-phase flow problems, such as the dam-breaking and liquid jet breakup settings. The proposed method employs the velocity-based formulation of the two-phase LBM, where the density is an arbitrary constant in the particle distribution function. This formulation is known to have better stability than the momentum-based formulation, as the pressure update has less incompressibility error, and the velocity update is done semi-implicitly. The cumulant collision model is also employed, which has good stability for problems with high Reynolds numbers. A second-order filter is also employed to further enhance the stability for the simulation of violent two-phase flows and can be turned off for non-violent flows. This filter adds artificial viscosity, which depends on the flow Peclet number similar to the advection equation's hybrid differencing scheme. The algorithm is completed by the conservative phase-field lattice Boltzmann method, which is used for interface capturing and guarantees mass conservation. A density-scaled continuous surface force model is employed for the surface tension force model.

The proposed method, along with its unfiltered version, has been validated on five non-violent two-phase flow problems: the 2D Rayleigh-Taylor instability, the 2D falling droplet, the 2D rising bubble, the 3D oblique coalescence of two bubbles, and the 3D droplet splashing on a thin film. These settings cover a wide range of density ratios, Reynolds numbers, and topological changes. The results show good agreements with both experimental and computational references. However, the proposed method is more diffusive than the unfiltered model due to the second-order filter, and therefore the high resolution is needed for sufficient accuracy, as seen in the Rayleigh-Taylor instability and splashing droplet problems. The proposed method has been applied to simulate two versions of the 3D dam-breaking and a 3D liquid jet breakup ($\gamma \approx 1000$ and $\mathrm{Re} \approx 10^5$), showing its capacity to handle violent two-phase flows. The results are in good agreement with the experimental and numerical results, where the maximum error in dimensionless surge front and water height are about 5% and less than 1%,

respectively. The dynamics of the free-surfaces, droplets, and bubbles are qualitatively in good agreement with the experiment. For liquid jet breakup, the difference of the penetration depth with that of the INSE solver is about 10%. It seems that the liquid jet in the present simulation breaks-up earlier than that of the INSE solver. Further study is needed to understand this phenomenon fully. However, we demonstrated that the proposed cumulant LBM could stably simulate the liquid jet breakup with a high-density ratio and Reynolds number.

6.1.2 Turbulent bubbly pipe flow simulations

A turbulent bubbly pipe flow with a high-density ratio and Reynolds number has been simulated using cumulant LBM. In this study, the unfiltered cumulant LBM and a multi-phase field model were employed to simulate the hydrodynamics and the interfaces of non-coalesce dispersed bubbles, respectively.

The proposed method was first evaluated by solving the turbulent single-phase-flow problem for both channel and pipe geometries and at both low and high Reynolds numbers ($\mathrm{Re}_\tau \approx 180$ and 550). The results obtained by the proposed method agree well with reference DNS calculations based on spectral methods; namely, normalized root mean square of errors (NRMSEs) are about 2% for $\mathrm{Re}_\tau \approx 180$ and about 9% for channel flow and 3% for pipe flow at $\mathrm{Re}_\tau \approx 550$.

The proposed method was then used to simulate two cases of turbulent bubbly channel flows with low-density ratio and low Reynolds number (i.e., void fractions of $\alpha = 1.5\%$ and 19.4%), and the results were compared with those given in computational references. The general behavior of the obtained flow is the same as that reported in the references; that is, the bubbles tend to fill the center of the channel, and average streamwise velocity is suppressed at the center of the channel. The bubbles generate vortices, and the flow becomes homogeneous at the center of the channel. The first and second-order statistics were calculated, and the calculation values agree reasonably well with the reference calculations; namely, Normalized Root Mean Square of Error (NRMSE) of the bubble distribution, mean streamwise velocity, and velocity fluctuations are about 10%.

Finally, a turbulent bubbly pipe flow of a water-air system with high -density ratio and high Reynolds number were simulated. The bubbles generated more vortices and are more deformed than in the previous turbulent bubbly channel flows. Average streamwise velocity is suppressed more homogeneously, and the magnitude of velocity fluctuations at the center of the pipe is almost uniform in all directions. The turbulent statistics obtained from the proposed method agree reasonably well with those obtained in the experiment, where the NRMSE of bubble distribution, mean streamwise velocity, and streamwise velocity fluctuation are about 12%, 4%, and 13%, respectively. As suggested by these results, the turbulent statistics are sensitive to change in bubble properties, void fraction, and Reynolds number; therefore, an accurate method that can stably simulate the real flow condition is necessary. The proposed method can stably simulate the flow conditions closer to the experimental setting with good accuracy using the given domain size and resolution. Therefore, it is promising for more realistic turbulent bubbly simulations in the future.

6.1.3 Foam formation simulations

The foam formation is a commonly occurred phenomenon in our daily lives, such as soap, beer, river, and sea foams. The phenomenon also occurs in various industries, such as textile, food, oil recovery, and recycling industries. Although it has been widely studied experimentally, the foam formation is rarely studied numerically due to the difficulties in simulating polydisperse bubbles separated by thin liquid films. In this study, we simulate the foam formation using a cumulant lattice Boltzmann method to calculate the two-phases' hydrodynamics, combined with a multi-phase field model to capture the polydisperse bubble interfaces. Each bubble is assigned as a separate phase using the multi-phase field model, and the bubble coalescence can be avoided. Additionally, we study and apply an iterative pressure projection method in our simulation and improve the active parameter tracking (APT).

2-D bubble rising problem is revisited and simulated again, and the results show the capability of the pressure projection method in diminishing the compressibility error. Smaller compressibility error helps to stabilize our foam simulation because it

can suppress phase-field variable value oscillation. 2D and 3D foam formation with high density and viscosity ratio were stably simulated. We have tested our proposed method for 200 air bubbles in water ($\gamma \approx 831.7, \eta = 55.6, \alpha = 12.5\%$) with various sizes and show the behavior of the foam formation. The improved APT method also helps to improve the efficiency of the computation. This study is expected to be useful in the future to understand the effect of the foam formation with additional physics involved, such as the heat transfer in a medium.

6.2 Recommendations

Several studies can be performed in the future, such as:

1. Violent two-phase flows: Further studies are needed to improve and extend the present method's use. These may include a filter enhancement, a high-resolution computation using parallel computers, and simulation of other violent two-phase flow problems, such as those including the solid objects.

2. Turbulent bubbly pipe flow simulations: Improvement of the simulation efficiency such as the use of adaptive mesh refinement (AMR), calculation of more realistic turbulent bubbly flows such as those with higher Reynolds number and arbitrary boundaries and alignments. The calculation of more detailed turbulent statistics can also be performed to better understand the turbulent characteristics due to bubble interactions.

3. Foam formation: multi-scale and multi-physics phenomena can be simulated in the future, such as the material and heat transport on thin liquid film. Also, the algorithm for bubble breakup must be developed. Improvement of the computational efficiency is necessary, including the AMR study and other alternative interface capturing schemes.

Appendices

Appendix A

Cumulant-collision Model

The PDFs are first transformed into central moments by using the following forward central moment transformation:

$$K_{ij|\gamma} = \sum_k f_{ijk}(k - u_z/c)^\gamma, \tag{A.1}$$

$$K_{i|\beta\gamma} = \sum_j K_{ij|\gamma}(j - u_y/c)^\beta, \tag{A.2}$$

$$K_{\alpha\beta\gamma} = \sum_i K_{i|\beta\gamma}(i - u_x/c)^\alpha, \tag{A.3}$$

The forward cumulant transformation is then applied to transform the central moments into the cumulant as follows (equations that can be obtained by permuting indices are set analogously):

$$C_{100} = K_{100}, \tag{A.4}$$

$$C_{110} = K_{110}, \tag{A.5}$$

$$C_{200} = K_{200}, \tag{A.6}$$

$$C_{120} = K_{120}, \tag{A.7}$$

$$C_{111} = K_{111}, \tag{A.8}$$

$$C_{211} = K_{211} - (K_{200}K_{011} + 2K_{110}K_{101}), \tag{A.9}$$

$$C_{220} = K_{220} - (K_{200}K_{020} + 2K_{110}^2), \tag{A.10}$$

$$\begin{aligned} C_{122} =& K_{122} - (K_{002}K_{120} + K_{020}K_{102} + 4K_{011}K_{111} \\ &+ 2(K_{101}K_{021} + K_{110}K_{012})), \end{aligned} \tag{A.11}$$

$$\begin{aligned} C_{222} =& K_{222} - (4K_{111}^2 + K_{200}K_{022} + K_{020}K_{202} + K_{002}K_{220} \\ &+ 4(K_{011}K_{211} + K_{101}K_{121} + K_{110}K_{112} \\ &+ 2(K_{120}K_{102} + K_{210}K_{012} + K_{201}K_{021})) \\ &+ (16K_{110}K_{101}K_{011} + 4(K_{101}^2K_{020} + K_{011}^2K_{200} + K_{110}^2K_{002}) \\ &+ 2K_{200}K_{020}K_{002}). \end{aligned} \tag{A.12}$$

The collision step is executed in cumulant space as follows:

$$C_{100}^* = (1-\omega_1)C_{100} + (1-\frac{\omega_1}{2})C_{100}^F, \tag{A.13}$$

$$C_{110}^* = (1-\omega_2)C_{110}, \tag{A.14}$$

$$C_{200}^* - C_{020}^* = (1-\omega_2)(C_{200} - C_{020}), \tag{A.15}$$

$$C_{200}^* - C_{002}^* = (1-\omega_2)(C_{200} - C_{002}), \tag{A.16}$$

$$C_{200}^* + C_{020}^* + C_{002}^* = \omega_3 + (1-\omega_3)(C_{200} + C_{020} + C_{002}), \tag{A.17}$$

$$(C_{120}^* + C_{102}^*) = (1-\omega_4)(C_{120} + C_{102}), \tag{A.18}$$

$$(C_{120}^* - C_{102}^*) = (1-\omega_5)(C_{120} - C_{102}), \tag{A.19}$$

$$C_{111}^* = (1-\omega_6)C_{111}, \tag{A.20}$$

$$(C_{220}^* - 2C_{202}^* + C_{022}^*) = (1-\omega_7)(C_{220} - 2C_{202} + C_{022}), \tag{A.21}$$

$$(C_{220}^* + C_{202}^* - 2C_{022}^*) = (1-\omega_7)(C_{220} + C_{202} - 2C_{022}), \tag{A.22}$$

$$(C_{220}^* + C_{202}^* + C_{022}^*) = (1-\omega_8)(C_{220} + C_{202} + C_{022}), \tag{A.23}$$

$$C_{211}^* = (1-\omega_9)C_{211}, \tag{A.24}$$

$$C_{221}^* = (1-\omega_{10})C_{221}, \tag{A.25}$$

$$C^*_{222} = (1 - \omega_{11})C_{222}. \tag{A.26}$$

Equations for C^*_{010}, C^*_{001}, C^*_{101}, C^*_{011}, $(C^*_{210} + C^*_{012})$, $(C^*_{201} + C^*_{021})$, $(C^*_{210} - C^*_{012})$, $(C^*_{201} - C^*_{021})$, C^*_{121}, C^*_{112}, C^*_{212}, and C^*_{122} can be obtained by permuting indices. Note that the equilibrium of most cumulants or their combinations is zero. Note also that the equilibrium first-order cumulants is zero, and the first-order cumulants of the forcing PDFs are equal to the external forces ($C^F_{100} = F^n_x$, $C^F_{010} = F^n_y$, $C^F_{001} = F^n_z$), where n denotes the current time step. Kinematic viscosity ν is related to the relaxation rate as follows:

$$\omega_2 = \left(\frac{\nu}{c_s^2} \frac{\delta t}{\delta x^2} + \frac{1}{2} \right)^{-1}. \tag{A.27}$$

In the present study, relaxation rate ω_1 is set to zero, whereas the others are set to one.

After the collision, the cumulants are transformed back into central moments by using the following backward cumulant transformation:

$$K^*_{000} = 1, \tag{A.28}$$

$$K^*_{100} = C^*_{100}, \tag{A.29}$$

$$K^*_{110} = C^*_{110}, \tag{A.30}$$

$$K^*_{200} = C^*_{200}, \tag{A.31}$$

$$K^*_{120} = C^*_{120}, \tag{A.32}$$

$$K^*_{111} = C^*_{111}, \tag{A.33}$$

$$K^*_{211} = C^*_{211} + (K^*_{200}K^*_{011} + 2K^*_{110}K^*_{101}), \tag{A.34}$$

$$K^*_{220} = C^*_{220} + (K^*_{200}K^*_{020} + 2K^{*2}_{110}), \tag{A.35}$$

$$\begin{aligned} K^*_{122} =& C^*_{122} + (K^*_{002}K^*_{120} + K^*_{020}K^*_{102} + 4K_0 11^* K^*_{111} \\ &+ 2(K^*_{101}K^*_{021} + K^*_{110}K^*_{012})), \end{aligned} \tag{A.36}$$

$$
\begin{aligned}
K^*_{222} =& C^*_{222} + (4K^{*2}_{111} + K^*_{200}K^*_{022} + K^*_{020}K^*_{202} + K^*_{002}K^*_{220} \\
&+ 4(K^*_{011}K^*_{211} + K^*_{101}K^*_{121} + K^*_{110}K^*_{112}) \\
&+ 2(K^*_{120}K^*_{102} + K^*_{210}K^*_{012} + K^*_{201}K^*_{021})) \\
&- (16K^*_{110}K^*_{101}K^*_{011} + 4(K^{*2}_{101}K^*_{020} + K^{*2}_{011}K^*_{200} + K^{*2}_{110}K^*_{002}) \\
&+ 2K^*_{200}K^*_{020}K^*_{002}).
\end{aligned} \tag{A.37}
$$

Note that Eq. (A.28) means that the zeroth-order moment is at equilibrium, which is an essential condition for the recovery of the velocity divergence from the PDFs.

Finally, the backward central moment transformation is applied to transform the central moments back to obtain the post-collision distribution functions as follows:

$$
K^*_{0|\beta\gamma} = K^*_{0\beta\gamma}(1 - (u_x/c)^2) - 2(u_x/c)K^*_{1\beta\gamma} - K^*_{2\beta\gamma}, \tag{A.38}
$$

$$
K^*_{\bar{1}\beta\gamma} = \left(K^*_{0\beta\gamma}((u_x/c)^2 - u_x/c) + K^*_{1\beta\gamma}(2u_x/c - 1) + K^*_{2\beta\gamma}\right)/2, \tag{A.39}
$$

$$
K^*_{1|\beta\gamma} = \left(K^*_{0\beta\gamma}((u_x/c)^2 + u_x/c) + K^*_{1\beta\gamma}(2u_x/c + 1) + K^*_{2\beta\gamma}\right)/2, \tag{A.40}
$$

$$
K^*_{i0|\gamma} = K^*_{i|0\gamma}(1 - (u_y/c)^2) - 2(u_y/c)K^*_{i|1\gamma} - K^*_{i|2\gamma}, \tag{A.41}
$$

$$
K^*_{i\bar{1}\gamma} = \left(K^*_{i|0\gamma}((u_y/c)^2 - u_y/c) + K^*_{i|1\gamma}(2u_y/c - 1) + K^*_{i|2\gamma}\right)/2, \tag{A.42}
$$

$$
K^*_{i1|\gamma} = \left(Ki|0\gamma^*((u_y/c)^2 + u_y/c) + K^*_{i|1\gamma}(2u_y/c + 1) + K^*_{i|2\gamma}\right)/2, \tag{A.43}
$$

$$
f^*_{ij0} = K^*_{ij|0}(1 - (u_z/c)^2) - 2(u_z/c)K^*_{ij|1} - K^*_{ij|2}, \tag{A.44}
$$

$$
f^*_{ij\bar{1}} = \left(K^*_{ij|0}((u_z/c)^2 - u_z/c) + K^*_{ij|1}(2u_z/c - 1) + K^*_{ij|2}\right)/2, \tag{A.45}
$$

$$
f^*_{ij1} = \left(K^*_{ij|0}((u_z/c)^2 + u_z/c) + K^*_{ij|1}(2u_z/c + 1) + K^*_{ij|2}\right)/2. \tag{A.46}
$$

Bibliography

Aihara, S., Takaki, T., and Takada, N. (2019). Multi-phase-field modeling using a conservative allen–cahn equation for multiphase flow. *Computers & Fluids*, 178:141–151.

Aland, S. and Voigt, A. (2012). Benchmark computations of diffuse interface models for two-dimensional bubble dynamics. *International Journal for Numerical Methods in Fluids*, 69(3):747–761.

Amirshaghaghi, H., Rahimian, M. H., Safari, H., and Krafczyk, M. (2018). Large eddy simulation of liquid sheet breakup using a two-phase lattice boltzmann method. *Computers & Fluids*, 160:93–107.

Amsden, A. A. and Harlow, F. H. (1970). A simplified mac technique for incompressible fluid flow calculations. *Journal of Computational Physics*, 6:322–325.

Ba, Y., Liu, H., Li, Q., Kang, Q., and Sun, J. (2016). Multiple-relaxation-time color-gradient lattice boltzmann model for simulating two-phase flows with high density ratio. *Physical Review E*, 94(2):023310.

Balcázar, N., Lehmkuhl, O., Rigola, J., and Oliva, A. (2015). A multiple marker level-set method for simulation of deformable fluid particles. *International Journal of Multiphase Flow*, 74:125–142.

Banari, A., Janßen, C., Grilli, S. T., and Krafczyk, M. (2014a). Efficient gpgpu implementation of a lattice boltzmann model for multiphase flows with high density ratios. *Computers & Fluids*, 93:1–17.

Banari, A., Janßen, C. F., and Grilli, S. T. (2014b). An efficient lattice boltzmann multiphase model for 3d flows with large density ratios at high reynolds numbers. *Computers & Mathematics with Applications*, 68(12):1819–1843.

Bhatnagar, P. L., Gross, E. P., and Krook, M. (1954). A model for collision processes in gases. i. small amplitude processes in charged and neutral one-component systems. *Physical review*, 94(3):511.

Bois, G. (2017). Direct numerical simulation of a turbulent bubbly flow in a vertical channel: Towards an improved second-order reynolds stress model. *Nuclear Engineering and Design*, 321:92–103.

Bouzidi, M., Firdaouss, M., and Lallemand, P. (2001). Momentum transfer of a boltzmann-lattice fluid with boundaries. *Physics of fluids*, 13(11):3452–3459.

Brackbill, J., Kothe, D. B., and Zemach, C. (1992). A continuum method for modeling surface tension. *Journal of Computational Physics*, 100(2):335–354.

Brereton, G. and Korotney, D. (1991). Coaxial and oblique coalescence of two rising bubbles. *Dynamics of bubbles and vortices near a free surface*, 119:50–73.

Chen, L., Tian, Y., and Karayiannis, T. (2006). The effect of tube diameter on vertical two-phase flow regimes in small tubes. *International Journal of Heat and Mass Transfer*, 49(21-22):4220–4230.

Chen, Y., Teng, S., Shukuwa, T., and Ohashi, H. (1998). Lattice-boltzmann simulation of two-phase fluid flows. *International Journal of Modern Physics C*, 9(08):1383–1391.

Chiu, P.-H. and Lin, Y.-T. (2011). A conservative phase field method for solving incompressible two-phase flows. *Journal of Computational Physics*, 230(1):185–204.

Chorin, A. J. (1967a). A numerical method for solving incompressible viscous flow problems. *Journal of computational physics*, 135(2):118–125.

Chorin, A. J. (1967b). The numerical solution of the navier-stokes equations for an incompressible fluid. *Bulletin of the American Mathematical Society*, 73(6):928–931.

Cifani, P. (2017). Dns of turbulent bubble-laden channel flows.

Cifani, P., Kuerten, J., and Geurts, B. (2018). Highly scalable dns solver for turbulent bubble-laden channel flow. *Computers & Fluids*, 172:67–83.

Clift, R., Grace, J., and Weber, M. (1978). Bubbles, drops, and particles–academic press. *New York*, 510.

Colin, C., Fabre, J., and Kamp, A. (2012). Turbulent bubbly flow in pipe under gravity and microgravity conditions. *Journal of Fluid Mechanics*, 711:469–515.

d'Humieres, D. (2002). Multiple–relaxation–time lattice boltzmann models in three dimensions. *Philosophical Transactions of the Royal Society of London. Series A: Mathematical, Physical and Engineering Sciences*, 360(1792):437–451.

Eggels, J., Unger, F., Weiss, M., Westerweel, J., Adrian, R. J., Friedrich, R., and Nieuwstadt, F. (1994). Fully developed turbulent pipe flow: a comparison between direct numerical simulation and experiment. *Journal of Fluid Mechanics*, 268:175–210.

El Khoury, G. K., Schlatter, P., Noorani, A., Fischer, P. F., Brethouwer, G., and Johansson, A. V. (2013). Direct numerical simulation of turbulent pipe flow at moderately high reynolds numbers. *Flow, turbulence and combustion*, 91(3):475–495.

Fakhari, A., Bolster, D., and Luo, L.-S. (2017a). A weighted multiple-relaxation-time lattice boltzmann method for multiphase flows and its application to partial coalescence cascades. *Journal of Computational Physics*, 341:22–43.

Fakhari, A., Geier, M., and Lee, T. (2016). A mass-conserving lattice boltzmann method with dynamic grid refinement for immiscible two-phase flows. *Journal of Computational Physics*, 315:434–457.

Fakhari, A., Mitchell, T., Leonardi, C., and Bolster, D. (2017b). Improved locality of the phase-field lattice-boltzmann model for immiscible fluids at high density ratios. *Physical Review E*, 96(5):053301.

Frisch, U., Hasslacher, B., and Pomeau, Y. (1986). Lattice-gas automata for the navier-stokes equation. *Physical review letters*, 56(14):1505.

Geier, M., Fakhari, A., and Lee, T. (2015a). Conservative phase-field lattice boltzmann model for interface tracking equation. *Physical Review E*, 91(6):063309.

Geier, M., Greiner, A., and Korvink, J. G. (2006). Cascaded digital lattice boltzmann automata for high reynolds number flow. *Physical Review E*, 73(6):066705.

Geier, M., Schönherr, M., Pasquali, A., and Krafczyk, M. (2015b). The cumulant lattice boltzmann equation in three dimensions: Theory and validation. *Computers & Mathematics with Applications*, 70(4):507–547.

Gingold, R. A. and Monaghan, J. J. (1977). Smoothed particle hydrodynamics: theory and application to non-spherical stars. *Monthly notices of the royal astronomical society*, 181(3):375–389.

Gottlieb, S. and Shu, C.-W. (1998). Total variation diminishing runge-kutta schemes. *Mathematics of Computation of the American Mathematical Society*, 67(221):73–85.

Grace, J., TH, N., et al. (1976). Shapes and velocities of single drops and bubbles moving freely through immiscible liquids.

Gunstensen, A. K. and Rothman, D. H. (1993). Lattice-boltzmann studies of immiscible two-phase flow through porous media. *Journal of Geophysical Research: Solid Earth*, 98(B4):6431–6441.

Guo, Z. and Zhao, T. (2002). Lattice boltzmann model for incompressible flows through porous media. *Physical review E*, 66(3):036304.

Guo, Z., Zheng, C., and Shi, B. (2002). Discrete lattice effects on the forcing term in the lattice boltzmann method. *Physical review E*, 65(4):046308.

Harlow, F. H., Evans, M., and Richtmyer, R. D. (1955). *A machine calculation method for hydrodynamic problems*. Los Alamos Scientific Laboratory of the University of California.

Harlow, F. H. and Welch, J. E. (1965). Numerical calculation of time-dependent viscous incompressible flow of fluid with free surface. *The physics of fluids*, 8(12):2182–2189.

He, X. and Luo, L.-S. (1997). Lattice boltzmann model for the incompressible navier–stokes equation. *Journal of Statistical Physics*, 88(3-4):927–944.

He, X., Shan, X., and Doolen, G. D. (1998). Discrete boltzmann equation model for nonideal gases. *Physical Review E*, 57(1):R13.

Hejranfar, K. and Ezzatneshan, E. (2015). Simulation of two-phase liquid-vapor flows using a high-order compact finite-difference lattice boltzmann method. *Physical Review E*, 92(5):053305.

Herrmann, M. (2008). A balanced force refined level set grid method for two-phase flows on unstructured flow solver grids. *Journal of Computational Physics*, 227(4):2674–2706.

Hirt, C. W. and Nichols, B. D. (1981). Volume of fluid (vof) method for the dynamics of free boundaries. *Journal of computational physics*, 39(1):201–225.

Hu, C. and Sueyoshi, M. (2010). Numerical simulation and experiment on dam break problem. *Journal of Marine Science and Application*, 9(2):109–114.

Huang, J. and Wang, X.-P. (2018). A lattice boltzmann model for multiphase flows with moving contact line and variable density. *Journal of Computational Physics*, 353:26–45.

Hysing, S.-R., Turek, S., Kuzmin, D., Parolini, N., Burman, E., Ganesan, S., and Tobiska, L. (2009). Quantitative benchmark computations of two-dimensional bubble dynamics. *International Journal for Numerical Methods in Fluids*, 60(11):1259–1288.

Inamuro, T., Ogata, T., Tajima, S., and Konishi, N. (2004). A lattice boltzmann method for incompressible two-phase flows with large density differences. *Journal of Computational physics*, 198(2):628–644.

Inamuro, T., Yokoyama, T., Tanaka, K., and Taniguchi, M. (2016). An improved lattice boltzmann method for incompressible two-phase flows with large density differences. *Computers & Fluids*, 137:55–69.

Janssen, C. and Krafczyk, M. (2010). A lattice boltzmann approach for free-surface-flow simulations on non-uniform block-structured grids. *Computers & Mathematics with Applications*, 59(7):2215–2235.

Jiang, G.-S. and Peng, D. (2000). Weighted eno schemes for hamilton–jacobi equations. *SIAM Journal on Scientific Computing*, 21(6):2126–2143.

Jiménez, J. and Moin, P. (1991). The minimal flow unit in near-wall turbulence. *Journal of Fluid Mechanics*, 225:213–240.

Kamp, A., Chesters, A., Colin, C., and Fabre, J. (2001). Bubble coalescence in turbulent flows: a mechanistic model for turbulence-induced coalescence applied to microgravity bubbly pipe flow. *International Journal of Multiphase Flow*, 27(8):1363–1396.

Kashinsky, O. and Randin, V. (1999). Downward bubbly gas–liquid flow in a vertical pipe. *International journal of multiphase flow*, 25(1):109–138.

Kawaguti, M. (1953). Numerical solution of the navier-stokes equations for the flow around a circular cylinder at reynolds number 40. *Journal of the Physical Society of Japan*, 8(6):747–757.

Kawamura, T. and Kodama, Y. (2002). Numerical simulation method to resolve interactions between bubbles and turbulence. *International Journal of Heat and Fluid Flow*, 23(5):627–638.

Kim, J., Moin, P., and Moser, R. (1987). Turbulence statistics in fully developed channel flow at low reynolds number. *Journal of fluid mechanics*, 177:133–166.

Kim, S. H. and Pitsch, H. (2015). On the lattice boltzmann method for multiphase flows with large density ratios. *Journal of Computational Physics*, 303:19–27.

Koelman, J. (1991). A simple lattice boltzmann scheme for navier-stokes fluid flow. *EPL (Europhysics Letters)*, 15(6):603.

Latva-Kokko, M. and Rothman, D. H. (2005). Diffusion properties of gradient-based lattice boltzmann models of immiscible fluids. *Physical Review E*, 71(5):056702.

Lax, P. and Wendroff, B. (1960). Systems of conservation laws. comm. pure appl. math., 13.

Lee, T. and Lin, C.-L. (2003). Pressure evolution lattice-boltzmann-equation method for two-phase flow with phase change. *Physical Review E*, 67(5):056703.

Lee, T. and Lin, C.-L. (2005). A stable discretization of the lattice boltzmann equation for simulation of incompressible two-phase flows at high density ratio. *Journal of Computational Physics*, 206(1):16–47.

Liu, T. and Bankoff, S. (1993). Structure of air-water bubbly flow in a vertical pipe—i. liquid mean velocity and turbulence measurements. *International Journal of Heat and Mass Transfer*, 36(4):1049–1060.

Liu, X.-D., Osher, S., Chan, T., et al. (1994). Weighted essentially non-oscillatory schemes. *Journal of computational physics*, 115(1):200–212.

Lu, J. and Tryggvason, G. (2006). Numerical study of turbulent bubbly downflows in a vertical channel. *Physics of Fluids*, 18(10):103302.

Lu, J. and Tryggvason, G. (2008). Effect of bubble deformability in turbulent bubbly upflow in a vertical channel. *Physics of Fluids*, 20(4):040701.

Martin, J. C., Moyce, W. J., Penney, W. G., Price, A., and Thornhill, C. (1952). Part iv. an experimental study of the collapse of liquid columns on a rigid horizontal plane. *Phil. Trans. R. Soc. Lond. A*, 244(882):312–324.

Nakoryakov, V., Kashinsky, O., Randin, V., and Timkin, L. (1996). Gas-liquid bubbly flow in vertical pipes.

ONODERA, N. and AOKI, T. (2014). Large-scale simulation of gas-liquid-solid multiphase flow on gpu cluster. *Japanese Journal of Multiphase Flow*, 27(5):607–613.

Osher, S. and Sethian, J. A. (1988). Fronts propagating with curvature-dependent speed: algorithms based on hamilton-jacobi formulations. *Journal of Computational Physics*, 79(1):12–49.

Patankar, S. V. (1980). Numerical heat transfer and fluid flow(book). *Washington, DC, Hemisphere Publishing Corp., 1980. 210 p.*

Pereira, F. H., Verardi, S. L. L., and Nabeta, S. I. (2006). A fast algebraic multigrid preconditioned conjugate gradient solver. *Applied Mathematics and Computation*, 179(1):344–351.

Qian, Y.-H., d'Humières, D., and Lallemand, P. (1992). Lattice bgk models for navier-stokes equation. *EPL (Europhysics Letters)*, 17(6):479.

Richardson, L. F. (2007). *Weather prediction by numerical process*. Cambridge university press.

Ricot, D., Marié, S., Sagaut, P., and Bailly, C. (2009). Lattice boltzmann method with selective viscosity filter. *Journal of Computational Physics*, 228(12):4478–4490.

Rieber, M. and Frohn, A. (1999). A numerical study on the mechanism of splashing. *International Journal of Heat and Fluid Flow*, 20(5):455–461.

Rothman, D. H. and Keller, J. M. (1988). Immiscible cellular-automaton fluids. *Journal of Statistical Physics*, 52(3-4):1119–1127.

Saito, S., Abe, Y., and Koyama, K. (2017). Lattice boltzmann modeling and simulation of liquid jet breakup. *Physical Review E*, 96(1):013317.

Serizawa, A., Kataoka, I., and Michiyoshi, I. (1975). Turbulence structure of air-water bubbly flow—ii. local properties. *International Journal of Multiphase Flow*, 2(3):235–246.

Shan, X. and Chen, H. (1993). Lattice boltzmann model for simulating flows with multiple phases and components. *Physical Review E*, 47(3):1815.

Shinjo, J. and Umemura, A. (2010). Simulation of liquid jet primary breakup: Dynamics of ligament and droplet formation. *International Journal of Multiphase Flow*, 36(7):513–532.

Sitompul, Y. P. and Aoki, T. (2019). A filtered cumulant lattice boltzmann method for violent two-phase flows. *Journal of Computational Physics*, 390:93–120.

Sitompul, Y. P., Aoki, T., and Takaki, T. (2021). Simulation of turbulent bubbly pipe flow with high density ratio and high reynolds number by using the lattice boltzmann method and a multi-phase field model. *International Journal of Multiphase Flow*, 134:103505.

Spalding, D. B. (1972). A novel finite difference formulation for differential expressions involving both first and second derivatives. *International Journal for Numerical Methods in Engineering*, 4(4):551–559.

Sterling, J. D. and Chen, S. (1996). Stability analysis of lattice boltzmann methods. *Journal of Computational Physics*, 123(1):196–206.

Succi, S. (2002). Mesoscopic modeling of slip motion at fluid-solid interfaces with heterogeneous catalysis. *Physical Review Letters*, 89(6):064502.

Suga, K., Kuwata, Y., Takashima, K., and Chikasue, R. (2015). A d3q27 multiple-relaxation-time lattice boltzmann method for turbulent flows. *Computers & Mathematics with Applications*, 69(6):518–529.

Sun, Y. and Beckermann, C. (2007). Sharp interface tracking using the phase-field equation. *Journal of Computational Physics*, 220(2):626–653.

Sussman, M., Fatemi, E., Smereka, P., and Osher, S. (1998). An improved level set method for incompressible two-phase flows. *Computers & Fluids*, 27(5-6):663–680.

Swift, M. R., Orlandini, E., Osborn, W., and Yeomans, J. (1996). Lattice boltzmann simulations of liquid-gas and binary fluid systems. *Physical Review E*, 54(5):5041.

Tryggvason, G., Bunner, B., Esmaeeli, A., Juric, D., Al-Rawahi, N., Tauber, W., Han, J., Nas, S., and Jan, Y.-J. (2001). A front-tracking method for the computations of multiphase flow. *Journal of computational physics*, 169(2):708–759.

van Sint Annaland, M., Deen, N., and Kuipers, J. (2005). Numerical simulation of gas bubbles behaviour using a three-dimensional volume of fluid method. *Chemical Engineering Science*, 60(11):2999–3011.

Vreman, A. and Kuerten, J. G. (2014a). Comparison of direct numerical simulation databases of turbulent channel flow at re τ= 180. *Physics of Fluids*, 26(1):015102.

Vreman, A. and Kuerten, J. G. (2014b). Statistics of spatial derivatives of velocity and pressure in turbulent channel flow. *Physics of fluids*, 26(8):085103.

Wang, S., Lee, S., Jones Jr, O., and Lahey Jr, R. (1987). 3-d turbulence structure and phase distribution measurements in bubbly two-phase flows. *International Journal of multiphase flow*, 13(3):327–343.

Wang, Y., Shu, C., and Yang, L. (2015). An improved multiphase lattice boltzmann flux solver for three-dimensional flows with large density ratio and high reynolds number. *Journal of computational physics*, 302:41–58.

Wu, Y., Gui, N., Yang, X., Tu, J., and Jiang, S. (2018). Improved stability strategies for pseudo-potential models of lattice boltzmann simulation of multiphase flow. *International Journal of Heat and Mass Transfer*, 125:66–81.

Xiao, F., Honma, Y., and Kono, T. (2005). A simple algebraic interface capturing scheme using hyperbolic tangent function. *International Journal for Numerical Methods in Fluids*, 48(9):1023–1040.

Yamanaka, A., Takaki, T., Aoki, T., and Shimokawabe, T. (2012). Multiphase field simulation of austenite-to-ferrite transformation accelerated by gpu computing. *Journal of Computational Science and Technology*, 6(3):182–197.

Yang, K. (2019). Simulation of weakly compressible fluid flow with immersed object using lattice boltzmann and finite difference method. M.S. thesis, Tokyo Institute of Technology.

Yarin, A. L. (2006). Drop impact dynamics: splashing, spreading, receding, bouncing.... *Annu. Rev. Fluid Mech.*, 38:159–192.

Yokoi, K. (2007). Efficient implementation of thinc scheme: a simple and practical smoothed vof algorithm. *Journal of Computational Physics*, 226(2):1985–2002.

Youngs, D. L. (1982). Time-dependent multi-material flow with large fluid distortion. *Numerical methods for fluid dynamics*.

Zhao-Li, G., Chu-Guang, Z., and Bao-Chang, S. (2002). Non-equilibrium extrapolation method for velocity and pressure boundary conditions in the lattice boltzmann method. *Chinese Physics*, 11(4):366.

Zu, Y. and He, S. (2013). Phase-field-based lattice boltzmann model for incompressible binary fluid systems with density and viscosity contrasts. *Physical Review E*, 87(4):043301.